NASA/TM–2016-104606/Vol. 44

Technical Report Series on Global Modeling and Data Assimilation, Volume 44

Randal D. Koster, Editor

Estimation of the Ocean Skin Temperature using the NASA GEOS Atmospheric Data Assimilation System

Santha Akella, Ricardo Todling, and Max Suarez

February 2016

NASA STI Program ... in Profile

Since its founding, NASA has been dedicated to the advancement of aeronautics and space science. The NASA scientific and technical information (STI) program plays a key part in helping NASA maintain this important role.

The NASA STI program operates under the auspices of the Agency Chief Information Officer. It collects, organizes, provides for archiving, and disseminates NASA's STI. The NASA STI program provides access to the NASA Aeronautics and Space Database and its public interface, the NASA Technical Report Server, thus providing one of the largest collections of aeronautical and space science STI in the world. Results are published in both non-NASA channels and by NASA in the NASA STI Report Series, which includes the following report types:

- TECHNICAL PUBLICATION. Reports of completed research or a major significant phase of research that present the results of NASA Programs and include extensive data or theoretical analysis. Includes compilations of significant scientific and technical data and information deemed to be of continuing reference value. NASA counterpart of peer-reviewed formal professional papers but has less stringent limitations on manuscript length and extent of graphic presentations.

- TECHNICAL MEMORANDUM. Scientific and technical findings that are preliminary or of specialized interest, e.g., quick release reports, working papers, and bibliographies that contain minimal annotation. Does not contain extensive analysis.

- CONTRACTOR REPORT. Scientific and technical findings by NASA-sponsored contractors and grantees.

- CONFERENCE PUBLICATION. Collected papers from scientific and technical conferences, symposia, seminars, or other meetings sponsored or co-sponsored by NASA.

- SPECIAL PUBLICATION. Scientific, technical, or historical information from NASA programs, projects, and missions, often concerned with subjects having substantial public interest.

- TECHNICAL TRANSLATION. English-language translations of foreign scientific and technical material pertinent to NASA's mission.

Specialized services also include organizing and publishing research results, distributing specialized research announcements and feeds, providing help desk and personal search support, and enabling data exchange services. For more information about the NASA STI program, see the following:

- Access the NASA STI program home page at http://www.sti.nasa.gov

- E-mail your question via the Internet to help@sti.nasa.gov

- Fax your question to the NASA STI Help Desk at 443-757-5803

- Phone the NASA STI Help Desk at 443-757-5802

- Write to:

   NASA STI Help Desk
   NASA Center for AeroSpace Information
   7115 Standard Drive
   Hanover, MD 21076-1320

Technical Report Series on Global Modeling and Data Assimilation, Volume 44

Randal D. Koster, Editor

Estimation of the Ocean Skin Temperature using the NASA GEOS Atmospheric Data Assimilation System

Santha Akella
Science Systems and Applications, Inc., Lanham, MD

Ricardo Todling
NASA Goddard Space Flight Center, Greenbelt, MD

Max Suarez
NASA's Goddard Space Flight Center, Greenbelt, Maryland

Abstract

This report documents the status of the development of a sea surface temperature (SST) analysis for the Goddard Earth Observing System (GEOS) Version-5 atmospheric data assimilation system (ADAS). Its implementation is part of the steps being taken toward the development of an integrated earth system analysis. Currently, GEOS-ADAS SST is a bulk ocean temperature (from ocean boundary conditions), and is almost identical to the skin sea surface temperature.

Here we describe changes to the atmosphere-ocean interface layer of the GEOS-atmospheric general circulation model (AGCM) to include near surface diurnal warming and cool-skin effects. We also added SST relevant Advanced Very High Resolution Radiometer (AVHRR) observations to the GEOS-ADAS observing system. We provide a detailed description of our analysis of these observations, along with the modifications to the interface between the GEOS atmospheric general circulation model, gridpoint statistical interpolation-based atmospheric analysis and the community radiative transfer model.

Our experiments (with and without these changes) show improved assimilation of satellite radiance observations. We obtained a closer fit to withheld, in-situ buoys measuring near-surface SST. Evaluation of forecast skill scores corroborate improvements seen in the observation fits. Along with a discussion of our results, we also include directions for future work.

Contents

List of Tables

List of Figures

1   Introduction

The development of a coupled data assimilation system is motivated by the goal to achieve an internally self-consistent state of the entire earth system, and also its temporal evolution across different components (Dee *et al.*, 2014). In such an integrated earth system analysis (IESA), dynamical evolution of one component would be directly constrained to the state and observations in other components. In the context of a coupled atmosphere-ocean data assimilation system, such an IESA could provide better air-sea fluxes and interface states (such as the sea surface temperature, surface pressure, winds, currents, etc), that have the potential to improve prediction of tropical cyclogenis and seasonal forecasts by making them less prone to initialization shocks (Brassington *et al.*, 2015).

At the NASA Global Modeling and Assimilation Office (GMAO) an atmosphere-ocean coupled IESA is being developed by focusing on the air-sea interface, and the sea surface temperature (SST). The GMAO Goddard Earth Observing System (GEOS) Version-5 atmosphere and ocean data assimilation systems require SST information (used by the atmosphere as a *boundary condition* and by the ocean as *observed data*). It is currently specified from an existing analysis for the bulk SST (such as those described by Donlon and coauthors (2007); Reynolds *et al.* (2007)). In the current GEOS atmospheric data assimilation system (ADAS) SST comes from the Operational Sea Surface Temperature and Sea Ice Analysis (OSTIA) system (Donlon *et al.*, 2012). In the ocean data assimilation system (Vernieres *et al.*, 2012), the observed SST is from Reynolds *et al.* (2007).

Based on observations in the vicinity of the air-sea interface, the bulk and interface temperature (or, skin SST) could differ by $\sim 1 - 4^o K$ (Fairall *et al.*, 1996). However, the GEOS atmospheric general circulation model (AGCM) simply sets the skin SST to be almost equal to the bulk SST (Rienecker and coauthors, 2008), with the net surface heat budget being a diagnostic variable (Molod *et al.*, 2012). Also the ADAS does not assimilate any SST relevant satellite or in-situ observations (Rienecker *et al.*, 2011). As for the ocean data assimilation system (DAS), near sea-surface temperature observations are not assimilated at the temporal frequency of their availability; instead; daily average temperatures are assimilated. Also, the atmospheric states are based on an existing atmospheric analysis (Vernieres *et al.*, 2012), and hence there is no feedback between the oceanic and atmospheric analyses. Therefore, coupling the ocean DAS analyzed bulk SST to the ADAS skin SST is a logical first step towards the development of a GEOS coupled atmosphere-ocean IESA . In this report, we document the steps that were taken in the ADAS only; IESA related developments of the ocean assimilation system and its coupling to the ADAS will be addressed in the near future.

1.1   Document organization

This document is organized as follows: section 2 provides relevant background information and literature on differences between bulk and skin SSTs; we also review related work and highlight contributions of this study. In section 3 we describe our modeling of the relationship between bulk and skin SSTs. Additions to the near sea-surface observational component of the ADAS and also their inter-connectivity with the AGCM is detailed in section 4. The experimental set up is given in section 5 and is followed by an analysis of results in section 6. We also discuss the changes in the performance of the ADAS using various forecast prediction metrics in section 7. Finally in section 8 we conclude with a summary of the work done and results.

2   Background

The skin SST (henceforth denoted by $\mathbf{T_s}$) serves as a proxy for the air-sea interface temperature (Curry and coauthors, 2004). It is an important variable for the AGCM because it is used

to compute air-sea fluxes and air temperature (Brunke *et al.*, 2008). It is essential for ADAS as well, since it is used to compute the simulated brightness temperatures by radiative transfer models (Han *et al.*, 2006) for analysis of satellite radiance observations.

The $\mathbf{T_s}$ in the AGCMs and ADAS is typically set equal to the bulk SST (Dee *et al.*, 2011; Rienecker *et al.*, 2011) from upper ocean temperature analysis products, such as those described by Donlon *et al.* (2012); Reynolds *et al.* (2002, 2007); Roberts-Jones *et al.* (2012). But the near-surface ocean thermal structure is highly variable, as shown via observations (Fairall *et al.*, 1996; Gentemann and Minnett, 2008; Saunders, 1967; Soloviev and Lukas, 1997; Ward, 2006), and thus it is important to distinguish between different temperatures (skin, sub-skin, etc; see Donlon and coauthors (2007) for further details), and processes that lead to diurnal differences between the bulk SST and $\mathbf{T_s}$. During daytime (under solar insolation) and in calm winds, a stratified *diurnal warm* layer forms, which causes $\mathbf{T_s}$ to be warmer than bulk SST. However, very close to the air-sea interface, the ocean loses heat due to the net longwave, latent and sensible heat fluxes, and this results in the formation of a *cool skin* layer, causing a drop of about 0.5^oK in temperature. Radiometric measurements (infrared and microwave) and in-situ buoys close to the sea surface have the capability to measure these changes (see Donlon *et al.* (2002) for further details).

Several diagnostic/empirical models have been proposed to simulate the $\mathbf{T_s}$ variation (Fairall *et al.*, 1996; Filipiak *et al.*, 2010; Gentemann *et al.*, 2009; Price *et al.*, 1986). (Also see review by Kawai and Wada (2007) and references therein.) In the context of AGCMs, prognostic models have been tested and implemented (Beljaars, 1997; Takaya *et al.*, 2010a; Zeng and Beljaars, 2005) in the operational version of the European Center for Medium-Range Weather Forecasts (ECMWF) model; see Bellenger and Duvel (2009) for a discussion of the main differences between the prognostic model of Zeng and Beljaars (2005) and the diagnostic model of Fairall *et al.* (1996). The Zeng and Beljaars (2005) prognostic model has also been used by Brunke *et al.* (2008) in the Community Atmosphere Model version 3.1 (CAM3.1). Results from these models indicate that they can realistically simulate the near-surface observed (buoy and radiometric) temperature variations (Takaya *et al.*, 2010a), and also impact the model mean climatologies of precipitation, outgoing longwave radiation (OLR), latent and sensible heat fluxes (Brunke *et al.*, 2008).

2.1   Related work

Before proceeding further, we would like to point out recent related data assimilation studies that also used the Takaya *et al.* (2010a) (hereafter T10) model. With the ultimate goal of producing a near real time global analysis of diurnal SST, While and Martin (2013) tested a prototype system by sampling a T10 model-generated *true* state to obtain synthetic observations of a diurnally varying $\mathbf{T_s}$. A time-series of those observations were assimilated using the same model in an attempt to recover the true initial state of the model, net heat flux and wind speed at every time step. Their data assimilation experiments show that they could improve the fit to the true state (compared to first guess) and also recover the initial model state and heat fluxes, but not the wind speed. One of their conclusions was that the accurate specification of errors in forcing fields (heat fluxes and winds) and observations (of SST) is very important for a diurnal analysis of the global SST field. McLay *et al.* (2012) also implemented a modified version of the T10 model, but without a cool skin layer, in the Navy Operational Global Atmospheric Prediction System (NOGAPS). They obtained an improvement in precipitation (midday peak value and daily accumulation) and statistically significant differences in latent and sensible heat fluxes, OLR, 2m air temperature, etc. Overall, the diurnal $\mathbf{T_s}$ model provided improved forecasts in the tropics, and its impact was lower the midlatitudes.

2.2 Objectives

Here we estimate $\mathbf{T_s}$ using satellite radiance observations, the diurnal warming model of T10, and the cool skin model of Fairall *et al.* (1996) (hereafter F96) after implementing them into the GEOS-AGCM. Therefore *additional* background (or, first guess) fields of surface skin temperature are available to carry out an atmospheric analysis using the Gridpoint Statistical Interpolation (GSI), Kleist *et al.* (2009a,b); $\mathbf{T_s}$ is analyzed along with the upper air analysis. From an observations standpoint, we focus on the surface sensitive infrared (IR) channels; in particular, Advanced Very High Resolution Radiometer (AVHRR) observations have been added to the GSI observing system. For this *direct* assimilation of SST-relevant observations, the interface between GSI and Community Radiative Transfer Model (CRTM), Chen *et al.* (2008); Han *et al.* (2006) has been slightly modified. We would like to emphasize that with these changes in place, the CRTM uses a diurnally varying $\mathbf{T_s}$ to simulate brightness temperatures (for all sensors and channels), as opposed to using a bulk SST field. The analysis increment (including $\mathbf{T_s}$) is then used to force the AGCM via an Incremental Analysis Update (IAU) approach (Bloom *et al.*, 1996; Rienecker *et al.*, 2011). We expect that this procedure (for concurrent estimation of the atmospheric fields and $\mathbf{T_s}$) contributes to the preparedness of the GEOS-ADAS for an IESA.

3 Skin SST model in GEOS-AGCM

We first describe the status of $\mathbf{T_s}$ in the GEOS-AGCM before discussing changes that account for the incorporation of diurnal variations. The skin temperature for model grid points (more specifically, *tiles*) that are over land, lakes, sea ice and land ice is computed based on the net surface heat budget (Molod *et al.* (2012), pp. 29). But over the ocean, $\mathbf{T_s}$ is obtained by relaxing to a bulk SST (denoted by T_d) data product,

$$\mathbf{T}_s = \frac{\mathbf{T}_s + \gamma T_d}{1 + \gamma}; \; \gamma = \frac{\Delta t}{\tau_{sst}}; \; \Delta t \text{ is model time step.} \tag{1}$$

The (default) relaxation time-scale, τ_{sst}, is set to 10^{-3} seconds; hence $\gamma \gg 1$, $T_s \approx T_d$ and net surface heat flux simply serves as a diagnostic variable (Molod *et al.*, 2012). As for the T_d, GEOS-ADAS versions 5_11_0 and onwards have been using OSTIA SST for the bulk SST (Rob Lucchesi, personal communication, 2014). This data product has been designed to be a *foundation* SST and therefore has minimal diurnal variations, see Donlon *et al.* (2012).

Following F96, we compute the near sea surface temperature at depth (z),

$$T(z) = T_d + \Delta T_w(z) - \Delta T_c, \tag{2}$$

where T_d is the OSTIA SST and where ΔT_w and ΔT_c denote diurnal warming and cool-skin temperature changes respectively, as described below. $\mathbf{T_s}$ is simply given by $T(z = 0)$. By setting τ_{sst} to a large value (e.g., 10^{15} seconds), we no longer relax of $\mathbf{T_s}$ to T_d. Backward compatibility has been preserved for the usage of (1) , and options have been provided to to enable/disable the cool-skin and diurnal diurnal warming temperature changes.

3.1 Cool skin

Below the air-sea interface, a layer of a few millimeters thickness exists where there is a net heat loss (due to the cooling effect of net longwave, sensible and latent heat fluxes). Because this negative heat flux dominates the absorbed shortwave radiation, we observe cooling just below the surface

(see F96, Curry and coauthors (2004); Saunders (1967) for further details). We follow F96 and Zeng and Beljaars (2005) (hereafter ZB05) to diagnostically compute the thickness and temperature drop within this cool layer. The temperature drop is computed with

$$\Delta T_c = \frac{\delta}{\rho_w \, c_w \, k_w} Q_{net}^c, \tag{3}$$

where ρ_w, c_w and k_w denote density, heat capacity and thermal conductivity of sea water, respectively. δ is the thickness of this layer:

$$\delta = \frac{\lambda \, \nu_w}{u_{*,w}}, \tag{4}$$

where ν_w is kinematic viscosity and $u_{*,w}$ is the friction velocity over water ($= u_{*,a}\sqrt{\rho_a/\rho_w}$, where $u_{*,a}$ is the atmosphere friction velocity and ρ_a is air density). The parameter λ is computed as in F96:

$$\lambda = 6 \left[1 + \left\{ \left(\frac{\alpha_w g Q_b}{\rho_w c_w} \right) \left(\frac{16 \rho_w^2 c_w^2 \nu_w^3}{\kappa_w^2} \right) \frac{1}{u_{*,w}^4} \right\}^{3/4} \right]^{-1/3}, \tag{5}$$

where g denotes the acceleration due to gravity and α_w is the water thermal expansion coefficient. The virtual surface cooling, Q_b, due to buoyancy effects of salinity due to evaporation, is:

$$Q_b = Q^* + \left(\frac{S\beta c_w}{\alpha_w L_e} \right) H_l, \tag{6}$$

Here, $Q^* = H_l + H_s + LW_{net}$, where H_s, H_l, LW_{net} denote the net surface sensible, latent, and long-wave heat fluxes, respectively[1]. L_e denotes the latent heat of vaporization, S is the mean salinity, and β is its expansion coefficient; as in F96 we set $S\beta = 0.026$.

The net heat flux, Q_{net}^c, in this cool layer is computed as:

$$Q_{net}^c = (H_s + H_l - LW_{net}) - f_c SW_{net}^s \tag{7}$$

where SW_{net}^s denotes the net surface shortwave heat flux. Only a fraction of SW_{net}^s is absorbed in the cool-skin layer; this fraction, f_c, is computed (as in eqn.5 of ZB05) as $f_c = 0.065 + 11\delta - \frac{6.6 \times 10^{-5}}{\delta} [1 - \exp(-\frac{\delta}{8 \times 10^{-4}})]$. Also as in F96 and ZB05, we assume a linear variation of temperature within this layer: $T(z) = T_\delta - \Delta T_c (1 - \frac{z}{\delta})$, $0 \leq z \leq \delta$. The temperature at the bottom of the cool layer, $T_{z=\delta}$, is explained below.

3.2 Diurnal warming

In order to compute the diurnal warming we follow the one-dimensional (in the vertical, z-direction), single column prognostic model of T10,

$$\frac{\partial(T_\delta - T_d)}{\partial t} = \frac{(\mu_s + 1)Q_{net}^w}{\mu_s \rho_w c_w d} - \frac{(\mu_s + 1)\kappa u_{*,w} f(La)}{d \phi_h(\zeta)} (T_\delta - T_d), \tag{8}$$

where T_δ is the temperature at $z = \delta$, i.e., at the top (bottom) of the warm (cool) layer, d denotes the depth below the cool layer, and $\kappa = 0.4$ is von Kármán's constant. The stability parameter $\zeta = z/L$, where the Obukhov length, L, is computed with $L = \frac{\rho_w c_w u_{*,w}^3}{\kappa g \alpha_w Q_{net}^w}$. The similarity function is:

$$\phi_h(\zeta) = \begin{cases} 1 + \frac{5\zeta + 4\zeta^2}{1 + 3\zeta + 0.25\zeta^2} & \text{if } \zeta \geq 0, \\ (1 - 16\zeta)^{-1/2} & \text{if } \zeta < 0. \end{cases} \tag{9}$$

---

[1] Our sign convention for heat fluxes is positive downward (i.e., those fluxes which increase water temperature have a positive sign); this is the same convention used by F96 and ZB05

where μ_s is an empirical parameter (≤ 1), with smaller values leading to a stronger near-surface peaking of the temperature profile within the warm layer: $z \in [\delta, d]$, $T(z) = T_\delta - \left(\frac{z-\delta}{d-\delta}\right)^{\mu_s}(T_\delta - T_d)$, $\Delta T_w(z) = T(z) - T_d$. As in T10, the Langmuir number $La = \sqrt{\frac{u_{*,w}}{u_s}}$, where u_s is the surface Stokes velocity; we also use the same function for $f(La): f(La) = La^{-2/3}$. However, due to the absence of a wave model in GEOS-5, we simply set $u_s = 1\texttt{cm/s}$ globally. This value was obtained based on trial and error and off-line matching with the buoy-observed temperature time series. For the same reason, we do not adjust the second term on the right hand side of (8) as done in T10 and ZB05 to obtain a slow decay of ΔT_w after sunset (when $SW_{net}^s \approx 0$). In the future we will revisit this implementation of the T10 diurnal warming model in coordination with the development of a wave model to simulate the relaxation of $T_\delta \to T_d$.

The net heat flux in the warm layer is computed with:

$$Q_{net}^w = SW_{net}^w + (LW_{net} - H_s - H_l), \tag{10}$$

where SW_{net}^w ($= SW_{net}^s - \text{PEN}$) is the net shortwave radiation absorbed in the warm layer. In order to compute the penetrating shortwave radiation, PEN, a three-band absorption profile of Soloviev (1982) was used by ZB05, T10 and F96. However, as shown by Wick *et al.* (2005) and Ohlmann and Siegel (2000), PEN is sensitive to upper-ocean chlorophyll concentration, solar zenith angle, and cloud cover, and it can impact the diurnal warming; this topic was left as future work by T10. A comparison of Soloviev (1982) and following methodology to compute PEN and the resulting diurnal warming will be addressed in our own future work. We follow Chou and Suarez (1994) and compute

$$\begin{aligned} PEN &=& [(1 - ALB_{VR})DR_{UVR} + (1 - ALB_{VF})DF_{UVR}]\exp(-dK_{UVR}) + \\ && [(1 - ALB_{VR})DR_{PAR} + (1 - ALB_{VF})DF_{PAR}]\exp(-dK_{PAR}) \end{aligned} \tag{11}$$

where ALB_{VR} and ALB_{VF} denote surface visible beam and diffuse albedos respectively over water. The surface downwelling beam and diffuse fluxes in the ultraviolet (UVR) are given by DR_{UVR} and DF_{UVR}, and DR_{PAR} and DF_{PAR} denote the direct and diffuse photosynthetically active radiation (PAR) fluxes respectively (for details regarding these fluxes in the GEOS-AGCM, see Chou and Suarez (1994); Rienecker and coauthors (2008)). The extinction coefficient K_{UVR} is set to a constant value of $0.09\,\mathrm{m}^{-1}$, whereas $K_d(PAR)$ is specified based on a climatology of chlorophyll concentration and is the same as used by Vernieres *et al.* (2012) and Ham *et al.* (2014) in the GEOS atmosphere-ocean coupled model; it is plotted in Figure 1. Typically, higher concentrations of chlorophyll are found near coastlines or in regions where upwelling of cold water takes place. Turbidity of water is higher in these regions, and hence the corresponding values of $K_d(PAR)$ are high (for more details, please see Morel *et al.* (2007)); consequently shortwave radiation does not penetate deep into the water column. On the contrary, locations with smaller chlorophyll concentration have lower values of $K_d(PAR)$, and sunlight penetrates deeper into the ocean. Values of other parameters used in this study are given in section 5. We integrate (8) in time, using an implicit scheme to predict T_δ; then, using (3) and (2), we compute $T(z)$.

4 Assimilation for skin SST using GEOS-ADAS

We assimilate satellite and in situ observations in the framework of GEOS-5 ADAS (Rienecker and coauthors, 2008; Rienecker *et al.*, 2011); therefore the GEOS-5 AGCM is used to generate first guess, or *background*, fields. In order to perform atmospheric analysis in a 'first-guess-at-appropriate-time' fashion, we save background fields every six hours at synoptic times ($00, 06, 12, 18$ UTC)

and at plus/minus three hours (see section 4 of Rienecker and coauthors (2008) for further details). The analysis is performed using the GSI (Kleist *et al.*, 2009a,b) three-dimensional variational data assimilation (3D-Var); for a more recent overview of the GEOS-ADAS infrastructure see Todling (2013) and Bosilovich and coauthors (2015).

Before the development of the skin SST model, the GSI used the bulk SST from the AGCM as the background field for $\mathbf{T_s}$, and hence the CRTM (Chen *et al.*, 2008; Han *et al.*, 2006) also used it to compute background brightness temperature (henceforth denoted by $\mathbf{T_b}$) and to compute the observation minus background (OMB) residuals; in this study we used CRTM version 2.1.3.

The GSI analysis includes $\mathbf{T_s}$ as a control variable, and it is analyzed along with the rest of the upper air analysis. However, the analysis increment, T_s^{inc} (difference between analyzed and background $\mathbf{T_s}$), $T_s^{ana} - T_s^{bkg}$, is not taken into account by the ensuing AGCM integration (Derber and Wu, 1998; Rienecker and coauthors, 2008). In order to estimate $\mathbf{T_s}$, the following changes were made to the GEOS-ADAS.

4.1   Background fields

With the availability of the $\mathbf{T_s}$ model (section 3), the GEOS-AGCM provides additional two dimensional background fields: $d, \delta, \Delta T_c, T_\delta$ and T_d. Given an observation at any location (x_i, y_j and depth: z_{ob}) and time, we compute the corresponding first guess temperature at the appropriate time by following these three steps: i) temporally (linearly) interpolate the above background fields to the observation time, (ii) spatially interpolate them to the observation location using a bilinear interpolation, and (iii) compute the temperature at the observation depth following the temperature profile in the cool-skin (section 3.1) and diurnal warm (section 3.2) layers:

$$T(z_{ob}) = \left\{ \begin{array}{ll} T_\delta - \Delta T_c \left(1 - \frac{z_{ob}}{\delta}\right) & \text{if } 0 \leq z_{ob} \leq \delta \ \rightarrow \textbf{Cool Layer}, \\ T_\delta - \left(\frac{z_{ob}-\delta}{d-\delta}\right)^{\mu_s} (T_\delta - T_d) & \text{if } \delta < z_{ob} \leq d \ \rightarrow \textbf{Warm Layer}. \end{array} \right. \tag{12}$$

For observations that are close to the sea surface, $z_{ob} \approx 0$, and hence $T(z_{ob}) \approx T_s$; these observations are influenced by diurnal warming and cool skin. On the other hand, observations taken below the cool layer ($z_{ob} > \delta$) feel the presence of the warm layer only (Donlon and coauthors, 2007).

The term z_{ob} for in situ observations refers to the measurement depth, whereas for satellite observations, the relevant depth is non-trivial and is related to the wavelength of the electromagnetic radiation (Wieliczka *et al.*, 1989), angle of incidence and surface environmental conditions (C. Gentemann, personal communication, 2012). We follow table 1 of Donlon and coauthors (2007) and set the following z_{ob} values for all infrared (IR) and microwave (microwave (MW)) sensors:

$$z_{ob} = \left\{ \begin{array}{ll} 15 \, \mu\text{m} & \text{all IR}, \\ 1.25 \, \text{mm} & \text{all MW} \end{array} \right. \tag{13}$$

A more precise wavelength-dependent computation of the z_{ob} for IR and MW sensors is beyond the scope of this study.

If the observation is an in situ measurement, computation of $T(z_{ob})$ and hence OMB is trivial. For satellite radiance observations, on the other hand, we first compute $T(z_{ob})$ using (13) and (12). This temperature at z_{ob} and upper-air atmospheric fields are then used by the CRTM to compute simulated (or background) $\mathbf{T_b}$, by which we obtain the OMB. The CRTM also computes the sensitivity, $\partial T_b / \partial T_z$. However, the GSI analysis control variable is T_s, so we need $\partial T_b / \partial T_s$ for the 3D-Var cost functional minimization, and this is obtained via: $\partial T_b / \partial T_z = (\partial T_b / \partial T_s)(\partial T_s / \partial T_z)$. Here we use a simple approximate value for the Jacobian by setting $\partial T_s / \partial T_z = 1$. This approximation is reasonable for the IR observations because we assumed that the penetration depth is $15 \, \mu\text{m}$

(very close to the air-sea interface, $T(z = 15 \, \mu\text{m}) \approx T_s$), but it is not accurate for MW observations, since $z_{ob} \sim O(mm)$, a much larger value. In other words, for MW observations this approximation for $\partial T_s / \partial T_z$ is no longer realistic and will require further (future) investigation (for example, when MW satellite radiance observations are used for $\mathbf{T_s}$ analysis).

Regarding the $\mathbf{T_s}$ background error, we use the same covariance structure as in Derber and Wu (1998); following their procedure, it is assumed to be independent of other analysis control variables. The error variance is plotted in Figure 2. It was designed for analyzing ozone and as already noted by Derber and Wu (1998), this covariance structure can be improved to model the contrasting error correlations in the skin SST that are typically observed at ocean surface (for e.g. different correlation length scales are observed in different ocean basins). Addressing this topic is part of our current work (section 8).

4.2   Observations and analysis

Observations relevant to SST are available from in situ platforms such as ships, moored and drifting buoys, etc. While they directly measure the temperature, they are limited by spatial coverage and temporal frequency. Also, they do not measure within microns (or even millimeters) of the air-sea interface (Donlon *et al.*, 2002). Measurements that are most proximate to the skin SST are provided by the drifting buoys (see Lumpkin *et al.* (2013) for further details); they record hourly temperature at $\sim 20 cm$ depth and therefore provide near-continuous (in time) observations of the SST *close* to the air-sea interface. However, the global coverage is not uniform , and there are significant gaps at high latitudes. Because our immediate goal is to focus on the skin SST, we concentrate on satellite observations Donlon and coauthors (2007) and withhold in situ SST observations to passively *monitor* the OMB to identify any systematic biases.

Satellite measurements in the IR ($3.7 - 12 \, \mu\text{m}$ wavelengths) and MW ($6 - 11 \text{GHz}$ frequency) provide long term, continuous measurements of near-surface temperature (Castro *et al.*, 2008; Donlon and coauthors, 2007; Hosoda, 2010). In the GEOS-ADAS, analysis of MW observations in the SST-relevant frequency range is currently under development, and we do not consider them in this work. As for the IR observations, due to the extensive usage of the AVHRR observations for SST retrievals (May *et al.*, 1998; Reynolds *et al.*, 2007), we added $\mathbf{T_b}$ observations from NOAA-18 and Metop-A satellites to the GEOS-ADAS. Level 1B, global area coverage (GAC), ocean only data was obtained from the Environmental Modeling Center (EMC); it is at a resolution of $\sim 4 \text{ km}^2$ resolution, includes a cloud mask, and has information in three IR window channels (3B centered around $3.7 \, \mu\text{m}$, channels 4 and 5 approximately around 11 and $12 \, \mu\text{m}$ wavelengths, respectively). Due to solar *contamination* (Liang *et al.*, 2009), channel 3B (henceforth referred to as channel 3) daytime data are not used. The procedure for reading, spatial thinning, observational scoring and quality control (QC) of the data follows the same treatment as for any IR sounding observations handled by the GSI; see appendix B for a summary of the QC procedure. Abundant precautions have been taken to detect clouds and to reject observations that are deemed to be affected by them. Channel 3 is most sensitive to skin temperature, and therefore it has the greatest *potential* to drive the $\mathbf{T_s}$ analysis increment. However, similar wavelength IR channels (on other sensors) are currently inactive (i.e., not assimilated) in the GEOS-ADAS, and in general, it is challenging to assimilate such observations because of the complexities in radiative transfer modeling at such wavelengths (Chen *et al.*, 2012). Nevertheless we have attemped to *conservatively* assimilate observations from this channel (as already mentioned, only at local nighttime), by having a smaller contribution to the 3D-Var cost function (and its gradient), achieved by downweighting the observational error variance computed using the GSI QC procedure (Derber and Wu (1998), appendix B). Figure 3 shows the spatial coverage of AVHRR observations (channel 4, and on April 1, 2012 between 9-15 UTC), before and

after applying QC. Within a 6 hr analysis window approximately 36 thousand observations (in all 3 AVHRR channels, and on both NOAA-18 and Metop-A satellites) are retained after thinning and scoring, of which about 65% observations are rejected by QC. Though these observations have a global coverage, they do not provide sufficiently repeated measurements at the same locations to adequately provide diurnal variability information (see Gentemann *et al.* (2003) for details).

All of the satellite observations are bias-corrected using the variational bias correction (VarBC) procedure (Dee, 2004). As for the observational error variance, σ_o, we set it equal to $0.60, 0.68$, and 0.72^oK for channels 3, 4 and 5 respectively, of AVHRR (both NOAA-18 and Metop-A). These values were chosen such that the observational variance is lower than that specified for other surface-sensitive IR observations, due to better quality skin SST-relevant information provided by the the AVHRR instrument.

Using all of the observations (those regularly analyzed by GEOS-ADAS, plus AVHRR) and background fields (section 4.1), we obtain analyzed fields for upper-air and also for $\mathbf{T_s}$. The increments (difference between analysis and background fields) are applied to the GEOS-AGCM, i.e., via an IAU approach (Bloom *et al.*, 1996; Rienecker and coauthors, 2008). Since the analysis is performed over all surface types (ice, land, water, etc, see Derber and Wu (1998)), we apply the increment over all surface types, for all of the analyzed variables except for $\mathbf{T_s}$. For $\mathbf{T_s}$, we are concerned with the increment (T_s^{inc}) only over the *open ocean*; therefore it is applied only where the fraction of water is 100%.

The presence of aerosols and, in particular, dust impacts the SST (May *et al.*, 1992; Merchant *et al.*, 2006), and through atmospheric processes, there is a two-way feedback between the AGCM and the CRTM simulated $\mathbf{T_b}$. Here we have made no attempt to diagnose those mechanisms; for now, we leave this topic as future work. We have used the Goddard Chemistry, Aerosol, Radiation, and Transport (GOCART) model, which is already available in the GEOS-ADAS (Rienecker and coauthors, 2008); therefore the presence of aerosols can impact the skin SST simulated by the AGCM.

5 Experimental setup

In this paper, we compare four experiments to each other. The first is the control experiment (hereafter referred to as *CTL*); it mimics the operational configuration of the GEOS-ADAS (using version EnADAS-5_13_1). It uses OSTIA SST as the skin temperature (by the AGCM and GSI), and AVHRR observations are not assimilated. The second experiment, called *AVH*, is exactly like the CTL, but it assimilates the NOAA-18 and Metop-A AVHRR data (section 4.2) in addition to the observations assimilated in the CTL experiment. Also as in the CTL, when the CRTM computes $\mathbf{T_b}$, *AVH* uses OSTIA SST for $\mathbf{T_s}$. The third experiment, called *tSkin*, is similar to the CTL and does not assimilate AVHRR data; however it has the skin SST model (section 3) turned on, and therefore model-produced diurnal warming and cool skin affect the computation of $\mathbf{T_s}$, which is then used by the CRTM (to simulate $\mathbf{T_b}$). Finally, the experiment *Assim* combines all of the developments to the GEOS-ADAS described sections 3 and 4. It uses the skin SST model and assimilates the AVHRR data. The CRTM used $T(z_{ob})$ (given by (12)), with the values of z_{ob} for all IR and MW instruments given in (13). Also in Assim experiment, the analysis increment in $\mathbf{T_s}$ is used by the AGCM to forecast for the next analysis cycle. A summary of the experimental setup is given in Table 1.

The above choice of experiments is based on: (a) the changes made to the GEOS-AGCM (skin SST model), (b) the addition of AVHRR observations to the GSI analysis, and (c) usage of the increment in skin SST by the AGCM. Indeed combinations of items (such as (b) and (c) above) could be examined with additional experiments. Instead we choose to highlight the impact of the

above modifications using the aforementioned set of four experiments; a brief description of the results of combinations that are not explicitly presented will be provided in section 6.

Table 1: Summary of experimental setup

Exp. Name	skin SST model	skin SST used by CRTM	AVHRR obs	T_s Analysis Increment
CTL	off	OSTIA SST	passive (not used)	not used
AVH	off	OSTIA SST	active (analyzed)	not used
tSkin	on	OSTIA SST $+ \Delta T_w - \Delta T_c$	passive	not used
Assim	on	$T(z_{ob})$; see section 4.1	active	used

Using initial conditions from the above ADAS experiments, we also performed forecast experiments from a numerical weather prediction (NWP) perspective; these will be discussed in section 7. Except for these NWP forecasts, all experiments involve data assimilation cycles over the experiment period.

The experiments were configured at $\sim \frac{1}{2}^o$ (576×361) horizontal resolution on a cube sphere (C180) grid (Putman and Lin, 2007), with 72 vertical levels (Rienecker and coauthors, 2008), and the time step was set to 450 seconds. Data is assimilated every six hours, followed by a nine-hour forecast (first 6-hours with the application of IAU). All experiments started with the same initial conditions. A time period of 15-days (16-31 March 2012) was used as spin-up, and the experiments are evaluated for the month of April 2012[2]. We set depth $d = 2\,\mathrm{m}$, and we followed the procedure described in ZB05 for the parameter μ_s, setting it to 0.2.

6   Results and discussion

In this section we compare results from our experiments (Table 1). To evaluate our results, because these are data assimilation experiments, we provide direct comparisons with the observations (e.g., OMB, observation minus analysis (OMA)). We make no attempt to evaluate the state of the climate (e.g., by comparing to reanalyses); however, we provide comparisons among the experiments for the averages of a few important fields. Since we did not apply the $\mathbf{T_s}$ analysis increment (T_s^{inc}) over land and sea ice (section 4.2), we focus only on the open ocean.

We start with a description of the differences in the monthly mean climatologies for a few important variables (subsection 6.1) and then focus on the results from the skin SST model (subsection 6.2). The impact on the observing system (including withheld in situ SST observations) is presented in subsection 6.3, followed by a comparison of the $\mathbf{T_s}$ analysis increments (subsection 6.4).

6.1   Monthly mean climatology

The following is a description of the differences we obtained in monthly means (for April 2012) of $\mathbf{T_s}$, wind, sea level pressure (SLP), temperature, and humidity. We focus on these fields because the GEOS-ADAS assimilated them before the addition of $\mathbf{T_s}$. We also discuss the changes in surface heat fluxes.

The mean skin SST for the CTL (i.e., OSTIA SST in this case) and the differences from CTL for the AVH, tSkin and Assim experiments are shown in Fig. 4, with land and sea ice masked out.

---

[2] AVHRR satellite bias correction coefficients (for both NOAA-18 and Metop-A) were spun up from zero values using low resolution experiments.

Based on the setup of the AVH experiment, the $\mathbf{T_s}$ for AVH and CTL is identical, verified by the zero difference shown in Fig. 4(b). In contrast, experiments tSkin and Assim show positive (due to diurnal warming) and negative (cool skin) differences from CTL. The decrease is about 0.3^o to 0.5^oK, with lower values in the extratropics; a similar result was obtained by Beljaars (1997). The decrease in $\mathbf{T_s}$ is due to the persistent cool skin, which dominates the increase due to diurnal warming (sections 3.1 and 3.2) in the monthly averaged difference. This is because diurnal warming follows insolation and erodes at night time or during periods of strong winds, except for a few regions (mostly in the tropics, which have low wind speeds) where a residual amount is retained overnight; diurnal averages that illustrate these differences are presented in subsection 6.2. We also notice small differences in Figures 4(c) and (d), e.g., in the Indian Ocean and east of Gulf of Saint Lawrence. This is due to the differences between the tSkin and Assim experiments (Table 1); details follow shortly.

Fig. 5 shows the mean SLP for the CTL and the differences from it for the other experiments. Due to the addition of AVHRR (AVH experiment), there is an increase of about 4 hPa in the western Pacific and southern Oceans, a decrease of ~ 3 hPa or less everywhere else. Usage of the skin SST model (Fig. 5(c)) causes the SLP to increase ($\sim 4-6$ hPa) in the eastern Pacific Ocean and in the Atlantic and Indian Oceans. Results for the Assim experiment (Fig. 5(d)) are similar to those for AVH, except for an increase in the west Indian and a decrease in the south Atlantic (Angola current region) Oceans. There is a relatively small change (< 1 m/s) in the wind speed, as shown in Fig. 6; this is mostly restricted to the tropics, with minor differences among the AVH, tSkin and Assim experiments.

The zonally averaged temperature field for CTL and the differences from this field for the other experiments from the surface (1000 hPa) to 500 hPa is shown in Fig. 7. The difference between AVH and CTL is less than 0.01^oK everywhere. For the tSkin and Assim experiments, however, we obtain a warming of $\sim 0.01^oK$ in the tropics below 950 hPa and a cooling everywhere else. The peak cooling (around 900 hPa) is about 0.025^oK in the northern hemisphere extratropics (NHE), 0.09^oK in the tropics, and 0.06^oK in the southern hemisphere extratropics (SHE). For the near surface (below 950 hPa) and between $800-600$ hPa, we obtain slightly more ($\sim 0.01^oK$) cooling for the Assim experiment than for the tSkin experiment.

Fig. 8 depicts the zonal means of specific humdity for the CTL and the differences from these zonal means obtained in the other experiments. Differences between AVH and CTL are again negligible. As for the tSkin and Assim experiments, the differences from CTL are very similar and small; the experiments produce a drying effect in the NHE, SHE, and tropics, perhaps due to near-surface cooling, since this drying is mostly limited to about 900 hPa. The largest decrease in specific humidity was in the tropics (~ 0.12 mg/Kg) between $1000-900$ hPa, and between 900 and 850 hPa, we obtained a very small moistening effect (~ 0.04 mg/Kg). The differences in the zonal and meridional wind components are also tiny. The zonal mean of u-wind is plotted in Fig. 9. Larger differences are obtained with increasing elevation; for example, in the tropics at 500 hPa, the differences are about -0.1 m/s for the tSkin and Assim experiments. The differences are almost an order of magnitude smaller in the NHE and SHE and, for the latter, are limited to ~ 900 hPa. Similarly tiny differences are seen for the v-wind as well (not shown).

Fig. 10 shows the average net shortwave radiation at the surface for the CTL along with the differences obtained in the other experiments. The differences between AVH and CTL are negligible. However, there are coherent differences found for the tSkin and Assim experiments, with both showing an increased heat flux of ~ 10 W/m^2 in the tropics. (Elsewhere the differences are negligible.) This increased surface radiation is due to a decrease in the *high*-level (> 400 mb) cloud fraction (CF) of about 0.1 (not shown) in the tropics. The *low*-level CF (< 700 mb) also decreased by ~ 0.05, and there was no change in the mid-level CF (also not shown).

Changes in the average net longwave radiation at the surface is shown in Fig. 11. The net longwave radiation (LW_{net}) is given by the difference $LW_\downarrow - LW_\uparrow$, i.e., by the difference between the downward and upward fluxes. The upward flux is proportional to $\mathbf{T_s}^4$ (Stefan-Boltzmann law) and cools the ocean surface. The difference in LW_{net} between AVH and CTL is negligible, and the increase of $\sim 3\text{W/m}^2$ for tSkin and Assim in the extratopics is due to the decrease in $\mathbf{T_s}$ seen in Fig. 4; there was no change in $LW_\downarrow$ (not shown).

The CTL fields of net latent (H_l) and sensible (H_s) surface heat fluxes are shown in Figures 12 and 13, respectively, together with the differences obtained in the other experiments. The pattern of differences in H_l and H_s between AVH and CTL experiments is similar to that in the net longwave heat flux. For the tSkin and Assim experiments, we obtained a decrease in both $H_l (\sim 5 - 12\text{W/m}^2)$ and $H_s (\sim 3\text{W/m}^2)$ except for an increase in the latent heat flux of about 4W/m^2 that appears in the easten tropical Pacific Ocean (a region characterized by low wind speed and large diurnal warming). The decrease in H_l and H_s is spatially correlated with the change in wind speed shown in Fig. 6. A similar change in latent and sensible heat fluxes related to wind speed was noted by F96.

The resulting change in the net heat flux at the surface is plotted in Fig. 14. As expected, there is hardly any change for AVH. However, due to an increase in SW_{net}^s and LW_{net}, and due to a decrease in H_l and H_s, Q_{net}^s for tSkin and Assim is increased by about 10-20W/m^2.

6.2 Skin SST

We focus here on the contributions of the skin SST model: cool skin and diurnal warming. The skin SST model was used in the tSkin and Assim experiments (Table 1). In order to delineate the impact of AVHRR observations and the $\mathbf{T_s}$ analysis increment, first we discuss results from tSkin experiment. We present thereafter the differences between Assim and tSkin.

6.2.1 Cool-skin layer

The April 2012 mean of the temperature drop resulting from the cool-skin layer in the tSkin experiment is shown in Fig. 15. ΔT_c peaks at $\sim 0.4 - 0.5^o K$ in light wind conditions (tropics) and decreases to about $0.05^o K$ with increasing wind speed (for instance in the Southern Ocean); this is consistent with the values reported by Saunders (1967) and F96. The correlation between ΔT_c and wind speed is in fact due to the inverse relation (4) between the thickness of cool layer (δ) and the friction velocity over water ($u_{*,w}$); their averages are plotted in Figures 16 and 17, respectively. Based on (3), we also expect a direct correlation between ΔT_c and the net heat flux in the cool layer (Q_{net}^c); Fig. 18 depicts the mean Q_{net}^c.

During the day we obtain a variation of about 0.1^o to $0.2^o K$ in ΔT_c due to (7), which includes a negative contribution from the net surface shortwave radiation (SW_{net}^s). This diurnal variation in ΔT_c is plotted in Fig. 19. Regions of low wind speed (e.g., the tropical eastern Pacific and Indian Oceans) undergo the largest daily variability. Similar daily variations were also reported in F96.

The differences in ΔT_c obtained in the Assim and tSkin experiments were very small ($\sim 0.02^o K$). They were mostly restricted to the low wind speed regions in the tropics (not shown).

6.2.2 Diurnal warm layer

The diurnal warming is driven by insolation and modulated by winds (8). The monthly mean diurnal variation of ΔT_w for tSkin is shown in Fig. 20. The tropical oceans (with low wind speed) have the largest diurnal warming (as also reported in ZB05 and T10); for example, in the Indian Ocean we obtained maximum $\Delta T_w \sim 2^o K$. The net heat flux in the warm layer, Q_{net}^w, is plotted in Fig. 21. When

heat is gained by the ocean (i.e., $Q_{net}^w \geq 0$), ΔT_w is positive, and it quickly goes to zero (section 3.2) after sunset (when $SW_{net}^w \sim 0$ and $Q_{net}^w \leq 0$). In the extratropics we obtained a smaller diurnal warming than in the tropics due to the typically higher wind speeds and the reduced insolation.

The sensitivity of our diurnal warming to the wind speed and net heat flux is show in Fig. 22. After 21UTC in the eastern Pacific, ΔT_w quickly approaches zero with decreasing insolation; similar behavior was also obtained by While and Martin (2013) with the T10 model. T10 stressed that an accurate Langmuir number (La) is very important for the diurnal warming. As mentioned in section 3.2, we took a simple approach to computing La, leading to a range of $f(La)$ between unity and ~ 1.6, as plotted in Fig. 23; these values are comparable to the global constant value used by McLay et al. (2012), who also had no access to a wave model and set $f(La) = 1.4$. Therefore the fast decay of ΔT_w past sunset could be addressed with the aid of a more reastic Stokes velocity (section 3.2), and also perhaps by following ZB05 when $Q_{net}^w \leq 0$; these topics will be addressed in our future work.

Regarding the absorption of penetrating shortwave radiation PEN (section 3.2), Fig. 24 shows the averaged $SW_{net}^w(d)/SW_{net}^s$, which mostly follows an inverse relation to the spatial distribution of $K_d(PAR)$ shown in Fig. 1. On the other hand, the three band shortwave absorption model of Soloviev (1982) used in F96, ZB05 and T10, with $d = 2\,\mathrm{m}$, yields a constant value of $SW_{net}^w(d)/SW_{net}^s = 0.61$ globally; therefore our diurnal warming model had a smaller input of insolation in the tropics. Our follow-up work (in preparation) is directed towards comparing our results with those using the Soloviev (1982) absorption model. However, based on Fig. 24, and given the results presented thus far, we do not expect a significant qualitative change in our current results by using a different shortwave absorption model.

We obtained the following difference in the diurnal warming between the Assim and tSkin experiments: an increase of about 0.2^oK during afternoon- evening local time in the tropics, and a decrease of about $\sim 0.05^o - 0.1^oK$ in the extratropics (before local noon), as shown in Fig. 25 for difference between Assim and tSkin experiments. These differences are mostly caused by a change in the local stability, as indicated by the difference in similarity function (ϕ_h, section 3.2) shown in Fig. 26; this in turn is caused by the differences in the warm layer net heat flux (Q_{net}^w) and wind speed among the tSkin and Assim experiments (described in section 6.1).

6.2.3 Net impact on the skin SST

The combined effect of diurnal warming and cool skin impacts the difference between the OSTIA SST (T_d) and $\mathbf{T_s}$ due to (2), as shown in Fig. 27 for the Assim experiment. Variability and magnitudes are clearly related to the temperature drop due to ΔT_c and increase due to ΔT_w. This difference between skin and bulk SSTs is remarkably similar to that obtained within the ECMWF integrated forecast system for the same period as in our experiment (A. Beljaars, personal communication, 2014). The difference ($\mathbf{T_s}$-T_d) between Assim and tSkin is $\sim 0.2^oK$, mostly due to the above decribed changes in ΔT_w.

T10 used the diurnal SST amplitude (DSA) metric to compare their modifications to the ZB05 scheme; it has also been used in other studies, for instance see McLay et al. (2012) and Bellenger and Duvel (2009). At any given location, T10 defined DSA to be equal to $\mathbf{T_s}$(max)- $\mathbf{T_s}$(min) during 00 to 24 hours local mean time. T10 used hourly output between latitudes of $\pm 40^o$ (whereas Takaya et al. (2010b) considered $\pm 30^o$) over a period of 17 years to plot average DSA as a function of average 10 m wind speed and insolation. They also compared their results with empirical estimates based on Gentemann et al. (2003); see T10 for further details. In an attempt to validate our skin SST model results, Fig 28 shows April 2012 averaged DSA (for tSkin and Assim experiments) as a function of 10 m wind speed and insolation, and between 60^oS and 60^oN. Because of the relatively

small sample size (only 1 month and between 60^oN/S), our plot does not include a value for an insolation of $350 W/m^2$ and has only one data point for the $10 ms^{-1}$ wind speed regime. Assim has a larger DSA for all wind speeds and insolations, particularly at low wind speeds. It peaks at about $3^o K$, whereas in the case of T10 it was about $2.25^o K$ for $300 W/m^2$ insolation; also the rate at which the DSA rises for low wind speed values seems to be too steep for the present study when compared to T10. However, when considering DSA as a function of insolation (right panel of Fig. 28), our plot is close to that of T10. We do not show here a comparison with the empirical estimates of Gentemann *et al.* (2003) because we arrive at similar conclusions (C. Gentemann, personal communication, 2014).

Spatial distribution of DSA is shown in Fig.29. The Assim experiment shows about $0.5^o K$ larger DSA than the tSkin experiment (please recall differences in ΔT_w, Fig. 25) in the Indian Ocean and about $0.2^o K$ less than tSkin in, for example, the eastern Pacific. The excessive values of DSA near coastlines are perhaps due to the $\frac{1}{2}^o$ AGCM resolution; further refinement of the model tends to lessen this feature (caused by surface tile to grid interpolation). However, the fact that DSA $\sim 3^o K$ for low wind speeds and the presence of high values in the Indian Ocean underscore the need to improve our similarity function and our treatment of turbulent diffusivity (mixing due to surface waves). Similar issues regarding validation of DSA have also been noted by Takaya *et al.* (2010b) and McLay *et al.* (2012). Moreover, DSA is not directly measured by observations, and its estimation has limitations (please see T10, sections 3.3 and 4). In section 6.3.3, we directly compare our near-surface temperature profiles, $T(z)$, with in situ measurements.

To summarize, we acknowledge some drawbacks with our approach such as the rapid erosion of diurnal warming just after dawn and the high sensitivity to low values of wind speed (section 6.2.2); these issues will be addressed by future improvements. Overall, our diagnostics indicate that the range of our skin SST, its spatial distribution, and its diurnal variation are comparable to the values reported by F96, ZB05, and T10.

6.3 Residuals of observation minus background

The GEOS-ADAS assimilates a wide variety of satellite-based and in situ (*conventional*) observations, as described by Rienecker and coauthors (2008) and more recently by Bosilovich and coauthors (2015). The majority of these observations are satellite radiance data from different polar orbiting and geostationary satellites (section 3.5 of Rienecker and coauthors (2008)). For example, in our CTL experiment, for the 01 Apr 2012 00 UTC analysis, we utilized about 3.3 million observations, of which 2.6 million ($\sim 80\%$) were satellite brightness temperature ($\mathbf{T_b}$) observations; winds (satellite and conventional) contributed $\sim 12\%$, conventional temperatures contributed 3%, surface pressure and GPS measurements contributed 1% each, and the rest of the assimilated data was made up of moisture and ozone observations. Given this abundant usage of $\mathbf{T_b}$ observations by the ADAS, we start this section by describing the changes to the OMB for satellite radiance observations, followed by changes to the OMB in conventional (in situ) data.

6.3.1 Satellite radiance observations

We added AVHRR to the analysis observing system (section 4.2), and the AVH and Assim experiments assimilated these observations (Table 1). By comparing their AVHRR-OMB, we try to assess the impact of skin SST and $\mathbf{T_s}$ analysis versus using OSTIA SST. Fig. 30 shows a time-series of the OMB statistics for the AVHRR Ch 3 (on NOAA-18). We use this channel only during local nighttime (section 4.2); as a result, in comparison to the Ch 4 observations shown in Fig. 3b, the number of observations from Ch 3 is only about a thousand. Based on Fig. 30, Assim assimilated

a few more observations than AVH. Also for Assim, the mean OMB was closer to zero, whereas for AVH it was about -0.1^oK; also there was a larger bias correction of about 0.12^oK for AVH. As for the standard deviation, both experiments were well below the specified value of 0.6^oK observational error variance (section 4.2). Tables 2 and 3 provide a summary of the OMB statistics for other AVHRR channels on NOAA-18 and on Metop-A. There is a decrease in the mean OMB for Ch 3 on Metop-A as well; results for channels 4 and 5 were comparable for AVH and Assim.

We obtained minor improvements to the analysis of other IR and MW sensors that are currently being assimilated by the GEOS-ADAS. OMB statistics for hyperspectral IR instruments such as Atmospheric Infrared Sounder (AIRS) (on AQUA) and Infrared Atmospheric Sounding Interferometer (IASI) (on Metop-A) suggest a positive synergetic contribution from the skin SST, inclusion of AVHRR observations, and $\mathbf{T_s}$ analysis. Fig. 31 compares the monthly mean of the OMB for Ch 123 of AIRS before bias correction was applied for our experiments. Focusing only over the oceans, we notice that CTL and AVH are alike, whereas both tSkin and Assim have a reduced bias in the SHE. We also observe that in the tropics (central Pacific) the tSkin experiment has a larger warm bias than CTL and AVH, while Assim is closer to CTL and AVH. Besides the small reduction in mean bias for the surface peaking window channels, we also obtained a reduction in the standard deviation for the water vapor sensitive and lower troposphere peaking channels, as shown in Figures 32 and 33 for AIRS and IASI respectively. For both AIRS and IASI, the reduction was larger for Assim than for tSkin, whereas AVH did not show any significant change from CTL.

Fig. 34 shows the mean of the total bias correction, defined as OMB (bias corrected) - OMB (before bias correction), for the 18 UTC analyses for a window channel (number 8) of the first detector on GOES-15. Since GOES-15 is a geostationary satellite at 135° W, the reduction in the bias around 18 UTC west of the California coast is perhaps due to the diurnal warming from skin SST in the tSkin and Assim experiments (Fig. 27). Fig. 35 shows the monthly mean OMB for all the assimilated channels of the first detector on GOES-15. Using the skin SST (tSkin and Assim experiments) provides a decrease in the mean OMB, whereas simply adding AVHRR observations and using OSTIA SST for $\mathbf{T_s}$ (AVH experiment) did not change the statistics we obtained with the CTL. We obtained a similar result for other detectors on GOES-15 and also for GEOS-13 (not shown).

MW sensors such as the Advanced Microwave Sounding Unit (AMSU)-A also showed a small decrease in the mean bias; for example, Fig. 36 shows the mean OMB statistics (over ocean) for the assimilated channels on AQUA. This suggests that the improvements we obtained for the IR sensors also extend to the MW part of the electromagnetic spectrum; similar results were obtained for AMSU-A on the Metop-A and NOAA-19 satellites.

Table 2: Comparison of mean OMB statistics (in ^oK) for the AVHRR observations on board NOAA-18 for the AVH and Assim experiments. The specified value of observational error variance is given by σ_o. The average number of observations (NOBS), mean and standard deviation (SDEV) of bias corrected OMB, and mean bias correction (= OMB (bias corrected) - OMB (no bias correction)) were computed using all the analyses within the experiment time period.

Ch. Num.	σ_o	Exp. Name: AVH				Exp. Name: Assim			
		Nobs	Mean	SDEV	Mean Bias Corr	Nobs	Mean	SDEV	Mean Bias Corr
3	0.60	871	-0.102	0.32	0.116	934	-0.031	0.32	0.045
4	0.68	2168	0.008	0.40	-0.068	2251	0.026	0.41	-0.108
5	0.72	2488	0.040	0.51	-0.065	2562	0.049	0.52	-0.093

Table 3: Same as in Table 2 but for the AVHRR observations on board Metop-A.

Ch. Num.	σ_o	Exp. Name: AVH				Exp. Name: Assim			
		Nobs	Mean	SDEV	Mean Bias Corr	Nobs	Mean	SDEV	Mean Bias Corr
3	0.60	1054	-0.041	0.32	0.212	1079	0.014	0.33	0.109
4	0.68	2267	0.030	0.42	-0.041	2314	0.048	0.43	-0.106
5	0.72	2545	0.086	0.53	0.036	2596	0.097	0.54	-0.014

6.3.2 In situ observations

The impact of new skin SST on the analysis of conventional upper-air measured temperature, winds, moisture, and surface pressure for the experiments was minimal in comparison to the CTL. This is perhaps due to the fact that most of these observations are in the northern hemisphere over land and are not directly impacted by the skin SST changes considered here. We also remind the reader that the background error for $\mathbf{T_s}$ was univariate (section 4.1); therefore it does not relate to the errors in upper-air background fields.

For the sake of completeness, table 4 summarizes the changes we obtained to the OMB for these observation types. The $J_o = \sum_{i=Nobs} \text{OMB}_i^2/\sigma_i^2$ is the least-squares cost functional that is minimized in the 3D-Var analysis; the observation errors σ_i are the same for all the experiments, and *Nobs* denotes the number of observations. Therefore smaller (larger) J_o for any observation implies a better (worse) fit of the background field. With respect to the CTL, for Assim there were tiny deteriorations for surface pressure and temperature observations, and improvements for wind and moisture types, all within 1% of $J_o(CTL)$.

Table 4: Summary of monthly mean number of upper-air in situ observations (*Nobs*) and background fit (J_o) to these observations.

Observed field	CTL		AVH-CTL		tSkin-CTL		Assim-CTL	
	Nobs	J_o	$\Delta Nobs$	ΔJ_o	$\Delta Nobs$	ΔJ_o	$\Delta Nobs$	ΔJ_o
Surface pressure	63,282	7.19×10^3	0	4.56	0	-0.43	0	6.0871
Temperature	82,428	8.72×10^4	0	-164.51	0	-140.02	0	88.42
Wind	385,914	3.03×10^5	17	-919.71	25	-373.37	-2	-122.40
Moisture	8,178	4.27×10^3	0	-11.10	0	-23.57	0	-14.33

6.3.3 SST observations

Drifting buoys (section 4.2) measure near-surface SST and are part of the in situ observations that are used in the generation of SST analyses, such as the OSTIA SST (Donlon *et al.*, 2012). They have also been used by Castro *et al.* (2012) for validation of satellite SST data products, and Kennedy *et al.* (2007) used them to create a climatology of diurnal warming. The GEOS-ADAS does not analyze these observations. We obtained them from the NOAA/NESDIS iQuam and used them to validate our near-surface temperature from the tSkin and Assim experiments; hence these data are withheld from the analysis. Using the highest level of quality-controlled observations (Xu and Ignatov, 2014) and measurement depth $z_{ob} = 20$ cm in (12), we computed the first guess de-

paratures (OMB) for these SST observations[3].

Fig. 37 shows the spatial distribution of these observations on 01 April 2012 at 00 UTC, and it also defines the ocean basins for which we computed hourly OMB statistics. The basin-averaged mean OMB, plotted in Fig. 38, shows a diurnal cycle in all basins. Based on the design of the OSTIA SST analysis (Donlon *et al.*, 2012), observations that could have contained any diurnal warming would not have been analyzed, and if we assimilated them, we would have expected a mean OMB close to zero, hence no diurnal cycle in the OMB. However, since these observations were withheld, the only way we could change our fit to the data was with our skin SST model-produced diurnal warming (cool-skin is only about a few millimeters thick) and with the $\mathbf{T_s}$ analysis increment in the Assim experiment. Indeed we obtained a change in the fit to the data, for example, in the T-INDN from morning to afternoon; thereafter our diurnal warming rapidly erodes (section 6.2.2), and our OMB is almost the same as that for the OSTIA SST. Fig. 38 also shows that even though the spatial variation of the DSA shown in Fig. 29 for the Indian Ocean was large, it still fits the observations (though we do not have observations everywhere). Summary statistics are tabulated in Table 5; mean and standard deviations for tSkin and Assim are very similar. There was an increase of bias in the western Pacific ($\sim 0.03^oK$) and Atlantic ($\sim 0.02^oK$) and a decrease in the eastern Pacific and Indian Oceans (0.02^oK); the standard deviation changed by a tiny amount in all four basins. Statistics for other regions (outside the tropics: NHE, SHE) did not show a significant change from the fit of OSTIA SST to observations, perhaps due to stronger winds and a weaker diurnal cycle.

Evaluation based on the tropical moored buoys (TAO/TRITON, PIRATA, RAMA) measured SST at 1 m depth did not show any significant differences. Our diurnal warming was weak at that depth because of our μ_s value of 0.2 (section 3.2), which we specified by following the procedure in ZB05; a smaller value of μ_s yields a sharper peaking diurnal warming temperature profile closer to the surface. Our future work will be directed towards assimilating these observations, and we hope to address this issue in that context.

Table 5: Fit to the (withheld) drifting buoy in situ SST observations for the tSkin and Assim experiments. The locations of the buoys and ocean basins are plotted in Fig. 37. Mean (μ) and standard deviations (σ) are in ^oK, relative change in the σ is in %, and the values shown are averages over the experiment time period and for ocean basins shown in Fig. 37.

Region	No. of obs	obs-OSTIA SST		OMB **tSkin**		OMB **Assim**	
	(per hour)	μ_{OSTIA}	σ_{OSTIA}	μ_{tSkin}	$\frac{\sigma_{tSkin}-\sigma_{OSTIA}}{\sigma_{OSTIA}}$	μ_{Assim}	$\frac{\sigma_{Assim}-\sigma_{OSTIA}}{\sigma_{OSTIA}}$
T-WPAC	29	-0.0878	0.26	-0.1159	-0.19	-0.1201	0.10
T-INDN	16	0.1448	0.26	0.1076	-0.52	0.0946	2.18
T-ATLN	37	-0.0433	0.32	-0.0607	0.17	-0.0605	-0.17
T-EPAC	41	0.0316	0.21	0.0178	-1.10	0.0144	-1.47

6.4   Analysis Increments

Analysis increments provide observational feedback to the model trajectory and are obtained via analyses at the synoptic times (Rienecker and coauthors (2008); section 4) in the GEOS-ADAS. The monthly-averaged analysis increment (00 UTC analyses) in $\mathbf{T_s}$ for the different experiments is shown in Fig.39. By the design of the experiments (Table 1), only the increment in the Assim experiment feeds back on the model; for all other experiments, it serves merely as a diagnostic.

---

[3]Using a different value for z_{ob}, say 25 cm, did not impact results.

Positive (negative) values of the increment indicate that the analyzed $\mathbf{T_s}$ is warmer (cooler) than the background (or, first guess) $\mathbf{T_s}$. As Fig. 39 (a) and (b) indicate, there are tiny differences between CTL and AVH (e.g., Indian Ocean, Agulhas current/tip of Africa, eastern tropical Pacific Ocean) due to the addition of AVHRR observations in AVH. However, the use of the skin SST model produces a larger difference in the increment, as evident in Fig. 39 (c) and (d). Comparing the tSkin and Assim experiments, there are differences due to the use of AVHRR observations and the feedback from the use of the increment itself in the latter experiment. The average impact of the increment is to warm the $\mathbf{T_s}$ in the central Atlantic Ocean by $\sim 0.1^o$ K (local nighttime) and in the west Pacific Ocean (local daytime). A similar pattern is seen for the increments for other analyses at $06, 12$ and 18 UTC; 06 UTC analysis increments are plotted in Fig. 40. The global (open water only) mean and standard deviation of the increment for the different experiments is shown in Fig. 41. If the observation and background errors are well tuned, then the increments are typically unbiased and have a low standard deviation (see appendix C for a simple proof). Indeed the increment for the Assim experiment is least biased and has the lowest standard deviation among the CTL and the other experiments. The feedback of the increment thus seems to have an overall positive impact.

As for the impact on the increments for other analyzed variables, Fig. 42 shows the global mean and standard deviation of the surface pressure increments, which do not appear significantly different between the different experiments. Also, there are no noticeable spatial differences in the increments at different synoptic times; hence these are not shown. Similar results are found for the zonal and meridional components of the three dimensional wind field (also not shown). However, increments in the temperature (Fig. 43) and specific humidity (Fig. 44) fields are slightly changed in the tropics for the tSkin and Assim experiments, albeit the standard deviation of the increments is also increased in the tropics; hence we do not consider the upper-air increments to be significantly different in the context of this study.

7   Impact on predictions

Through five day forecasts (starting at 2100 UTC), and verifying against our own analysis, we assess the duration of the impact of the skin SST model, the assimilation of AVHRR observations, and the $\mathbf{T_s}$ analysis increment, using initial conditions generated within all the data assimilation experiments discussed thus far. Forecast skill is computed for global fields, not just over open water.

Starting on 1 April 2012 and ending on 30 April 2012, i.e., with 30 samples, the anomaly correlation (ACOR) for the geo-potential height field (h) at 500 hPa is shown in Fig. 45. The forecasts from Assim have the highest h-ACOR, followed by tSkin, AVH and CTL, although the differences are statistically insignificant (below the 95% confidence interval); the root-mean-squared-errors (RMSE) also show a similar pattern (not shown). Plots of the differences in 500 hPa h-ACOR for the NHE and SHE are shown in Figures 46 and 47 respectively. In the NHE there is a degradation of the forecast skill for the AVH experiment after 2.5 days, whereas for the other experiments, there is a statistically insignificant degradation; we obtained a similar pattern for other variables, such as surface pressure, temperature, winds, and specific humidity, in the NHE. In the SHE, we obtained a statistically significant improvement in the ACOR after four days. Once again, Assim has the best skill, followed by tSkin and AVH. In fact, in the SHE, the skill (Assim and tSkin experiments) improved for other variables as well, but the improvement diminished with increasing height. For example, in Figures 48 and 49 we plot the differences in the ACOR for the SHE temperature at 1000 hPa and 700 hPa, respectively; the improvement is statistically significant at 1000 hPa but not at 700 hPa. As for the tropics, change in the ACOR (and also the RMSE) was neutral at all pressure

levels and for almost all the fields.

8 Summary and conclusion

Skin SST, which is very important for air-sea interaction, is specified in the GEOS-5 ADAS from an already existing, daily SST product. This prescription of the skin SST therefore neglects a large variability, including a diurnal cycle and very thin, cool skin layer in contact with the atmosphere, that has been observed by radiometric and in situ observations taken close to the sea surface. Here we describe and implement a prognostic $\mathbf{T_s}$ model that produces a realistic evolution of $\mathbf{T_s}$, focusing on its estimation in the context of an ADAS. The model-produced $\mathbf{T_s}$ serves as a first guess for the analysis of $\mathbf{T_s}$-sensitive brightness temperature observations; the increments from such an analysis are then used in the ensuing model integration. In an attempt to obtain a more realistic estimate of the skin SST, the following updates/modifications have been made to the GEOS-ADAS.

8.1 Updates to the AGCM

The skin SST in the original version of the AGCM was based on the daily OSTIA SST product, and the net surface heat flux over the ocean was a diagnostic variable. We added a skin SST model to the air-sea interface component of the AGCM to prognostically compute: (i) a diurnal warming, mostly based on ZB05 and T10, and (ii) a diagnostic cool-skin layer following F96. Both of these effects are applied on top of the OSTIA SST, since it is a foundation SST.

We adapted the T10 diurnal warming model with the following three modifications. First, due to the unavailability of a wave model, we used a global constant value for the surface Stokes velocity. Second (given the first modification), we chose not to follow the T10/ZB05 procedure to simulate the slow decay of diurnal warming past dusk. We are concurrently working on the introduction of a wave component into the GEOS-ADAS and plan to revisit these topics thereafter. Third and finally, instead of a three band shortwave absorption model as used by F96, ZB05, and T10, we used a model that includes absorption in the visible and ultraviolet parts of the spectrum, and we also made use of the photosynthetically active radiation flux, for which the light absorption characteristics of water change based on biological activity. As a result, the ratio of absorbed to incident insolation was about $0.5 - 0.65$, compared to a global constant of 0.61 obtained from the three band model.

8.2 Updates to the atmospheric analysis and ADAS

The GSI-based atmospheric analysis already includes the skin SST as a control variable when analyzing the upper-air fields. However, the increment in $\mathbf{T_s}$ was simply ignored in the next forecast cycle of the AGCM.

Taking advantage of the existing analysis infrastructure, we made following changes: (i) we added the relevant diurnal output from the modified AGCM to compute a near-surface vertical thermal structure (that is, $T(z)$), (ii) we use this $T(z)$ to compute first-guess temperatures at the (approximate) measurement depth, (iii) we added SST-relevant observations (taking AVHRR as a starting point) to the observing system, and (iv) we allowed the increment in skin SST to feed back on the AGCM through the IAU component.

8.3 Experimental results

To test the above updates to the model and analysis systems, we conducted three experiments, comparing each to a control (CTL) in which none of these changes were activated. The AVH

experiment was designed to test the impact of AVHRR observations only, tSkin tested the impact of the skin SST model only, and finally the Assim experiment combined all of the updates (the active skin SST model, AVHRR observations, and the feedback of the T_s analysis increment on the AGCM).

Using the skin SST model in the tSkin and Assim experiments, we obtained the cool skin (depth and amount of cooling) and the diurnal warm layer (depth and amount of warming) fields, along with their net effect on T_s.

As a result of the cool skin layer model, the amount of cooling was inversely proportional to the wind speed; minimum and maximum values of cooling were about 0.05^o and 0.5^oK, respectively. The diurnal variation in the net heat flux produced a maximum variability of about 0.2^oK in areas with large insolation and low wind speed (e.g., the Indian Ocean). In comparing the tSkin and Assim experiments, we noticed a very small impact ($< 0.02^oK$) on the cool skin layer.

We obtained a maximum diurnal warming of about 2^oK in the tropical oceans; this warming was lower in the extratropics. The peak diurnal warming was about 2 to 3 hours after local noon, a result similar to that obtained by ZB05 and T10 and similar to observations reported by F96. However, due to the differences between our diurnal model implementation and that in T10 mentioned above, we obtained a quick erosion of our diurnal warming after sunset, indicating an excessive amount of dissipation. We also obtained a DSA of about $2.5^o - 3^oK$ at low wind speeds, as in ZB05; this is about $\frac{1}{2}^oK$ more than in T10. Considering figure 3 of T10, the difference may also be related to our simplification of the Stokes velocity; however, DSA is not directly measured and there are uncertainties in its estimation. Overall, the difference between skin and foundation (OSTIA) SSTs was between -0.6^o to 1.5^oK. Changes in the local stability caused the Assim experiment to have a larger diurnal warming than the tSkin experiment by about 0.2^oK.

The overall change in climatology of assimilated fields (winds, temperature, humidity, and surface pressure) was insignificant for all three experiments. Due to the cool skin layer of the skin SST model, the monthly mean of T_s was lower by about 0.3^o to 0.5^oK for the tSkin and Assim experiments. We also obtained a change in the surface heat fluxes for these two experiments. The net shortwave radiation increased due to a decrease in the tropical high-level cloud fraction. In the extratropics, the net longwave flux increased, and there was a decrease in the latent and sensible heat fluxes; these changes resulted in an increase of about $10 - 20\text{W/m}^2$ in the net surface heat flux.

Averaged observation minus background (OMB) statistics for satellite observations showed a decrease in the mean OMB with the usage of the skin SST model. This improvement was consistent across the board for IR as well as MW sensors. Hyperspectral instruments (AIRS and IASI) statistics also revealed a positive feedback from the skin SST and the combination of assimilating AVHRR and the T_s increment. The fit to the surface as well as the water vapor-sensitive and lower troposphere peaking channels was improved for both the tSkin and Assim experiments, with more gain in the latter. There was an insignificant change for the AVH experiment.

We attempted to evaluate the temperature within the diurnal warming layer by using withheld observations (at 20 cm depth) from drifting buoys. The OMB was compared with the observation-minus-OSTIA SST as a starting point, because the latter is a foundation SST. The diurnal warming from our skin SST model (and T_s analysis) was closer to the observations, at least for certain times of the day. In the tropics, particularly in the Indian Ocean, where we obtained large diurnal warming, the morning to afternoon (rising part of the diurnal warming cycle) OMB was lower than that for OSTIA SST. However, the late afternoon-evening part of the diurnal cycle did not show any improvement due to a rapid erosion of our diurnal warming. The differences between the tSkin and Assim experiments were small. A weaker diurnal cycle outside of the tropics leads to an insignificant change in the OMB.

Application of the increment in the skin SST seems to provide a positive feedback to the GEOS-

ADAS, as indicated by the global mean and standard deviation of the increment. The overall impact of the analysis increment was to warm the $\mathbf{T_s}$ by about 0.1^oK during both local day and local night. There was no significant difference in the analysis increments of the surface pressure and in the 3-dimensional upper-air increments of temperature, u-and v-winds, and specific humidity.

There was an impact on the predictability of the model. Among our three experiments, the combination of all changes (in the Assim experiment) produced the best forecast skill scores, up to a lead time of 5-days. Statistically significant improvements were obtained in the southern hemisphere for almost all fields; however, the significance diminished with altitude.

8.4 Conclusion

Using an ocean mixed layer model to resolve the SST diurnal cycle in the ECMWF operational system, Takaya *et al.* (2010b) obtained improvements in 3- 5 days ACOR of temperature (at lower levels, e.g., 1000, 850 hPa); these improvements, however, were statistically insignificant, and they also they reported no difference in 500 hPa geopotential height ACOR. Conclusions based on our results using GEOS-ADAS cannot be extrapolated to the performance of other systems, since we verified forecasts against our own analyses. However, Takaya *et al.* (2010b) (on p.27) stress the importance of coupling between SST and errors in air-sea fluxes. In that regard, modeling the skin SST and assimilating SST-relevant observations offers an opportunity to explicitly account for SST errors and air-sea interface fluxes. This was precisely the goal of the Assim experiment, which yielded the most positive results among the experiments considered here.

This point is reinforced by the work of McLay *et al.* (2012) with the US Navy NOGAPS operational ADAS system, which included an SST diurnal cycle (via the T10 model, but with no cool-skin and also no direct assimilation of SST-relevant radiance observations) and perturbations for SST analyses (in an ensemble data assimilation framework), thus taking a step in the direction of explicitly accounting for SST errors. Based on forecasts up to lead times of 10 to 14 days, they reported statistically significant improvements in skin temperature (land and sea), 2-m air temperature, 10 m wind speed, 500 hPa geopotential heights and daily accumulated precipitation.

Takaya *et al.* (2010b), McLay *et al.* (2012) and the present study (with GEOS-ADAS) show, using three different operational systems that incorporate related modifications to the SST, that such modifications mostly lead to positive improvements in the forecasts. Further studies of skin SST modeling, air-sea fluxes, coupling with a wave model, tuning of atmospheric boundary layers, and modeling of the observational and background errors should be pursued along with the incorporation of MW and in situ SST observations in the context of the development of an IESA.

9 Acknowledgments

Discover cluster of the NASA Center for Computational Sciences (NCCS) at the Goddard Space Flight Center.
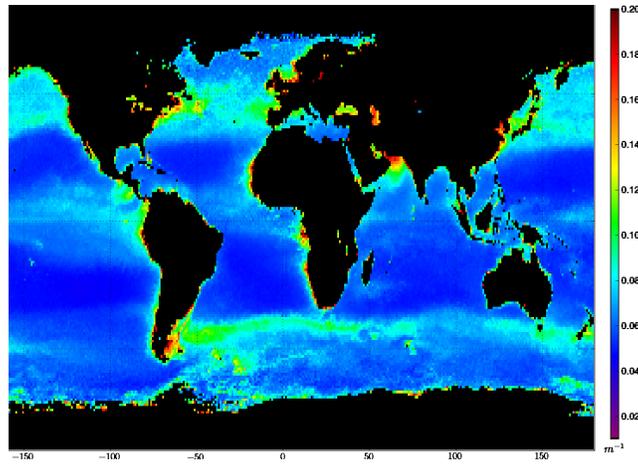
Figure 1: Climatological downward diffuse attenuation coefficient for the photosynthetically available radiation, or, $K_d(PAR)$, for the month of April. *Masked* values are set to one (black color); these appear over land and sea ice and are not used in open ocean computations.
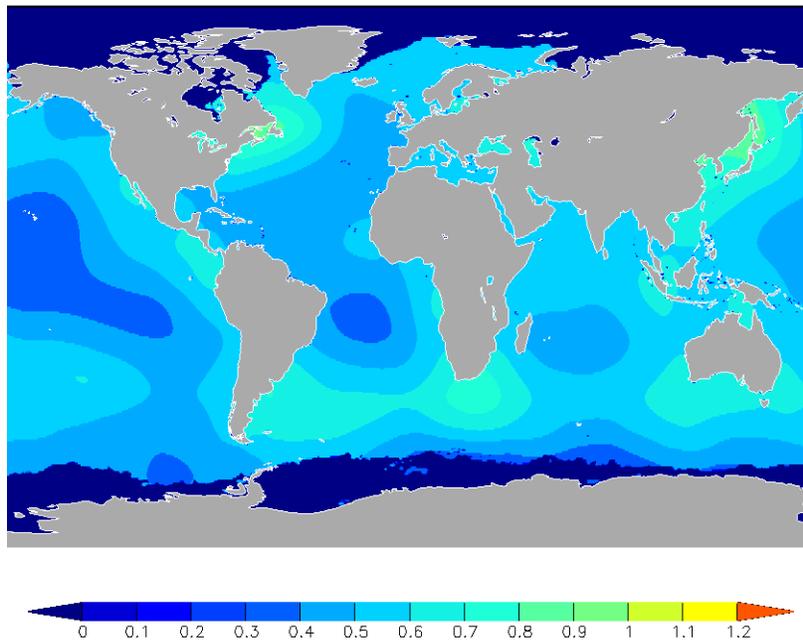
Figure 2: Background error variance used for analyzing $\mathbf{T_s}$ (in $^oC^2$). Values range from zero over sea ice-covered regions to ~ 1 in regions of high variability, such as the Gulf stream and Kuroshio current regions. Land has been masked.
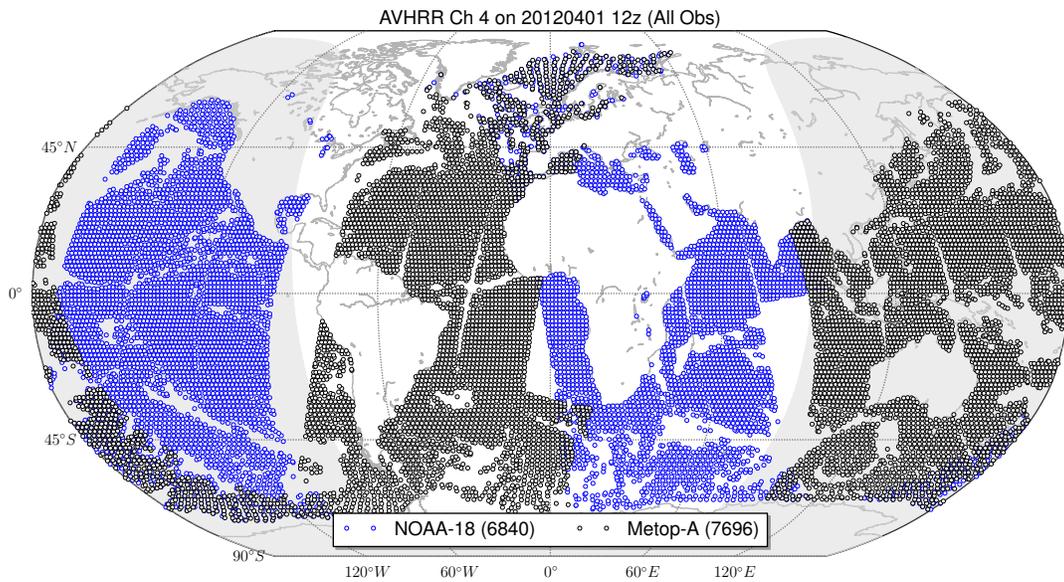
(a) **Before QC**
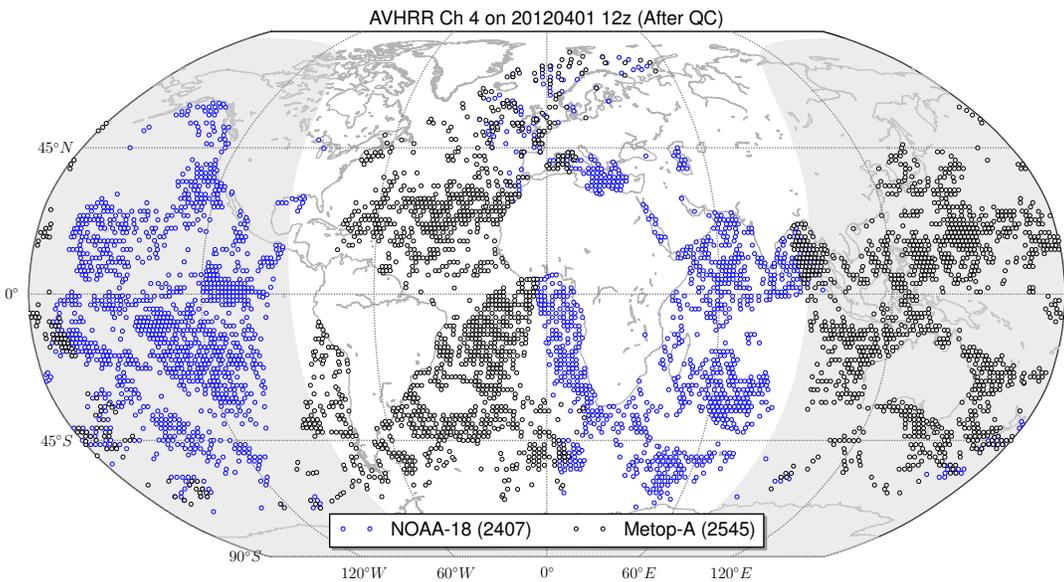
(b) **After QC**

Figure 3: Spatial coverage of AVHRR channel 4 brightness temperature observations taken from NOAA-18 (blue open circles) and Metop-A (black) within the 6-hour assimilation window centered on 01 Apr 2012 at 12 UTC. Shaded portion of the globe depicts nighttime, and the number of observations is shown in parentheses. 3a shows all the observations after thinning and scoring; 3b those retained after quality control (QC).
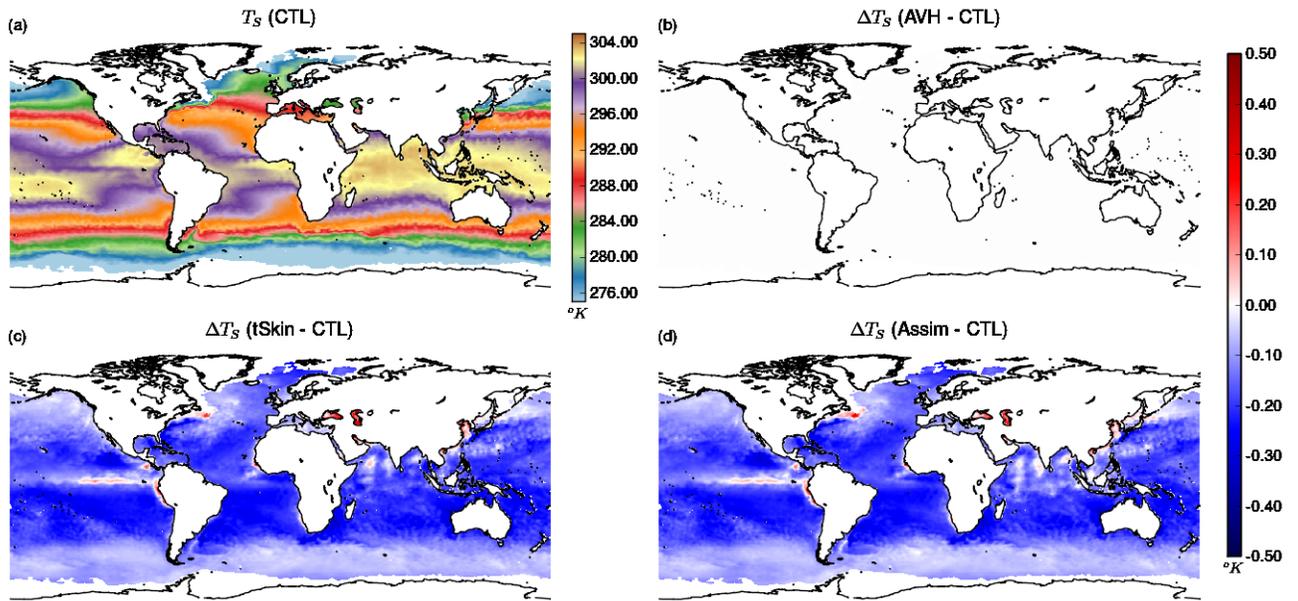
Figure 4: April 2012 monthly mean of the skin SST (^oK) for (a) CTL, and differences in $\mathbf{T_s}$ from CTL for the experiments: (b) AVH, (c) tSkin and (d) Assim. Land and sea ice regions have been masked.
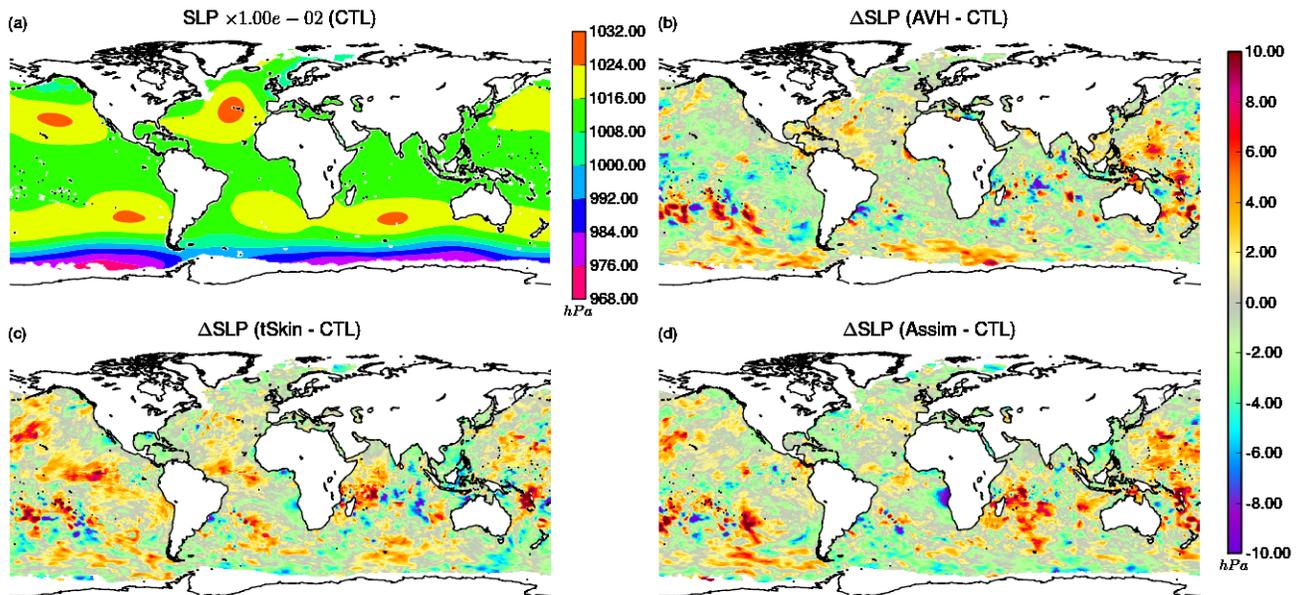
Figure 5: Same as in Fig. 4 but for the sea level pressure (SLP).
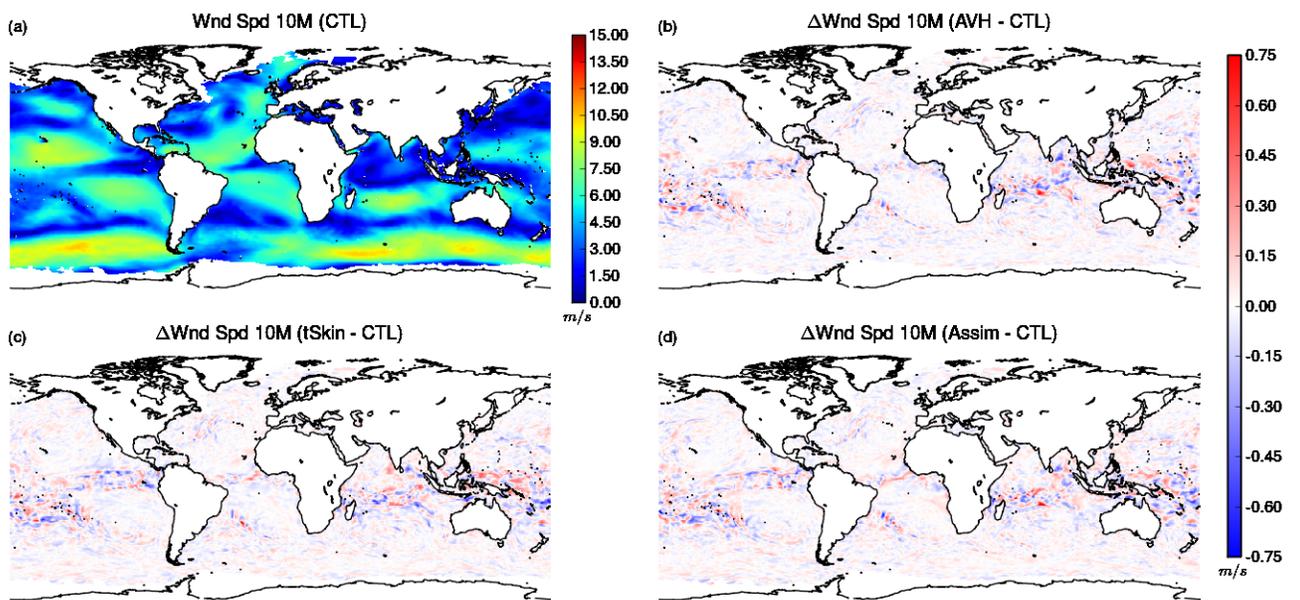
Figure 6: Same as in Fig. 4 but for the wind speed at 10 m.
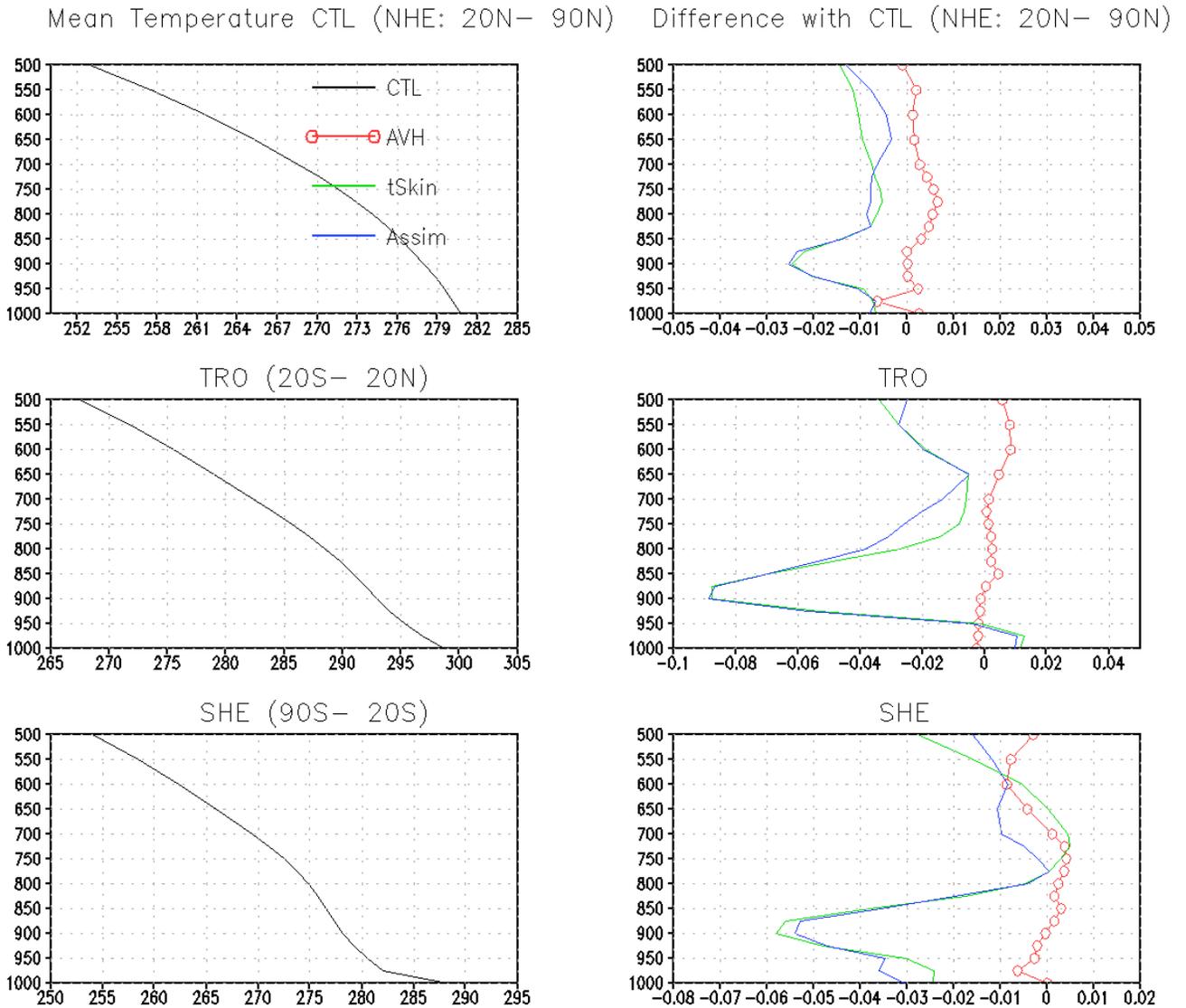
Figure 7: Zonal mean of temperature (^oK) from 1000 to 500 hPa. Top, middle and bottom rows are for northern hemisphere extratropics (NHE), tropics and southern hemisphere extratropics (SHE), respectively. CTL is plotted in the left panels, and the right panels show the difference from CTL for the AVH, tSkin and Assim experiments.
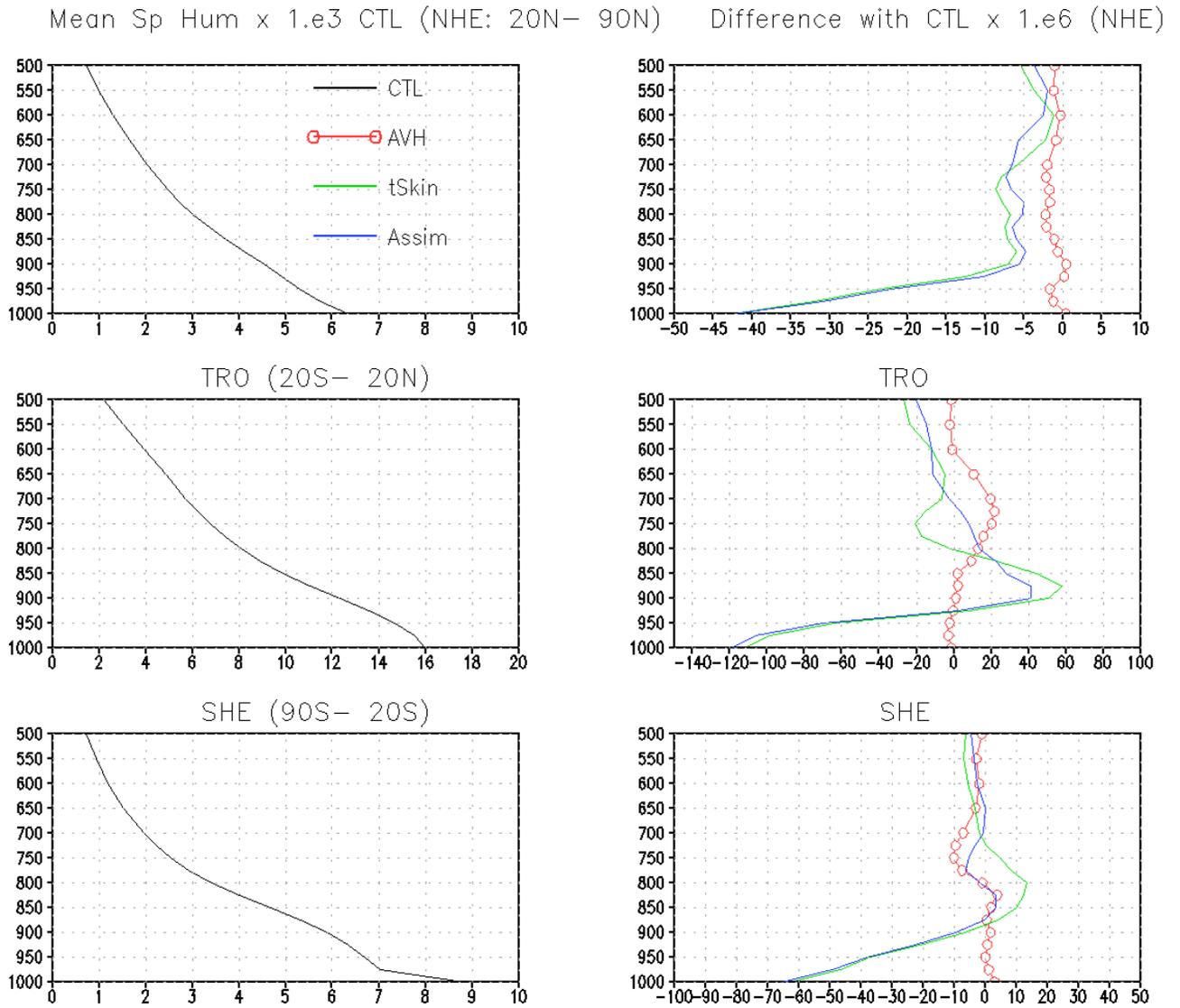
Figure 8: Same as in Fig. 7 but for the specific humidity (g/Kg).
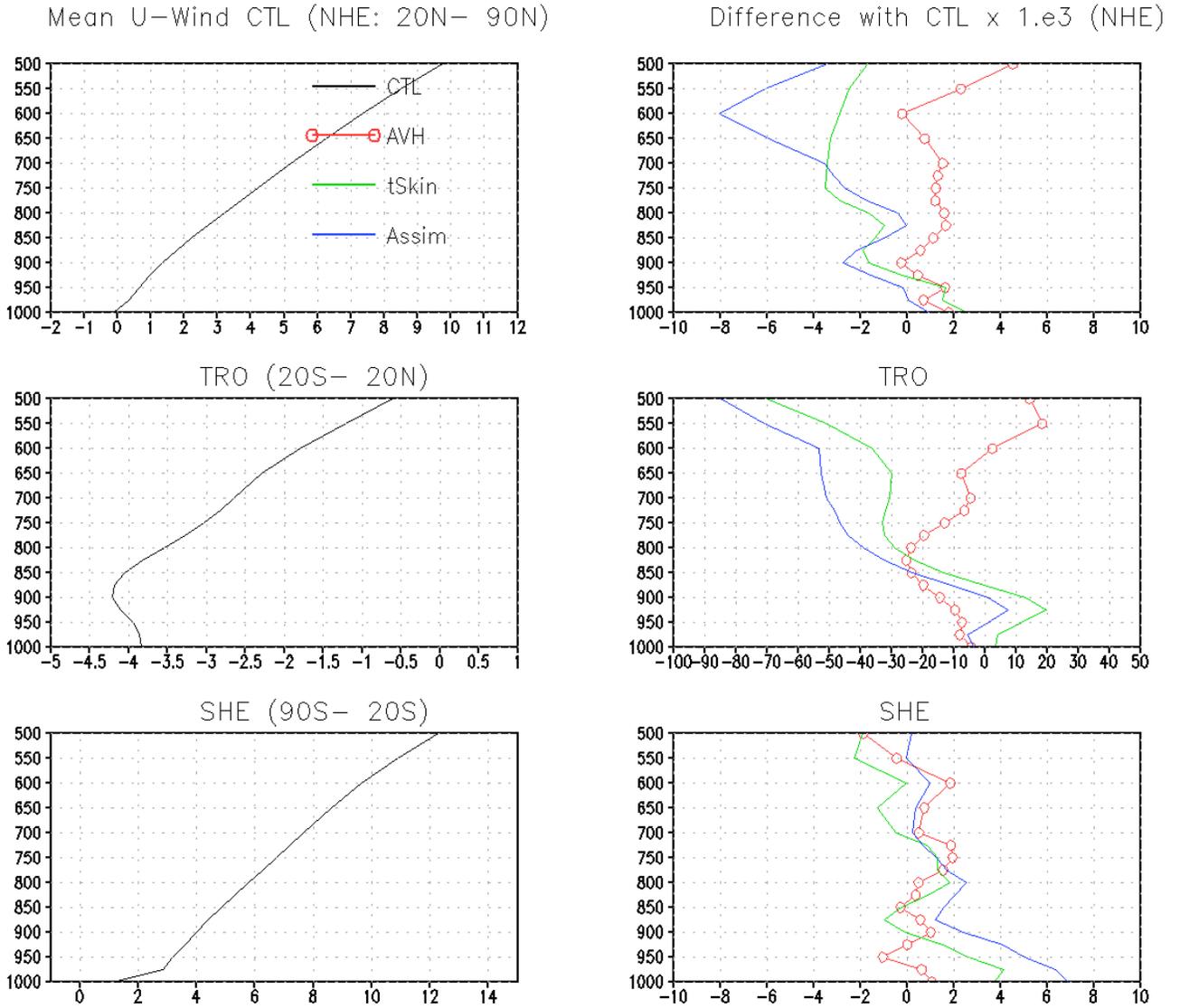
Figure 9: Same as in Fig. 7 but for the zonal component of wind (m/s).
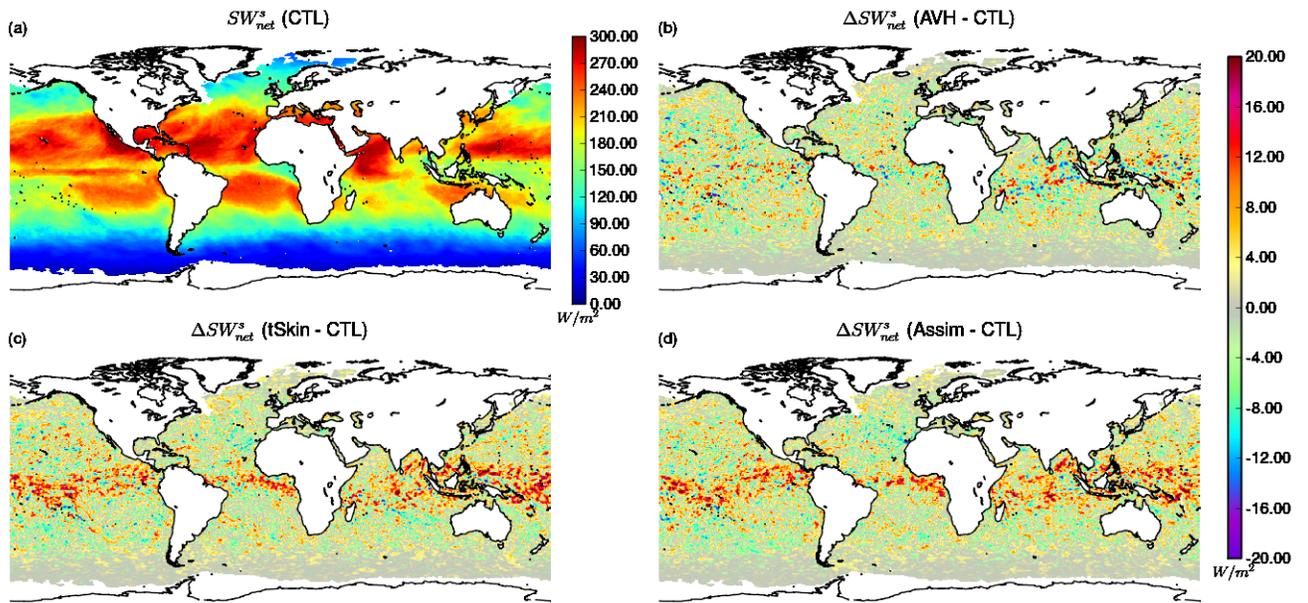
Figure 10: April 2012 monthly mean of the net surface shortwave radiation (SW_{net}^s) for (a) CTL, and differences in SW_{net}^s from CTL for the experiments: (b) AVH, (c) tSkin and (d) Assim. Land and sea ice regions have been masked.
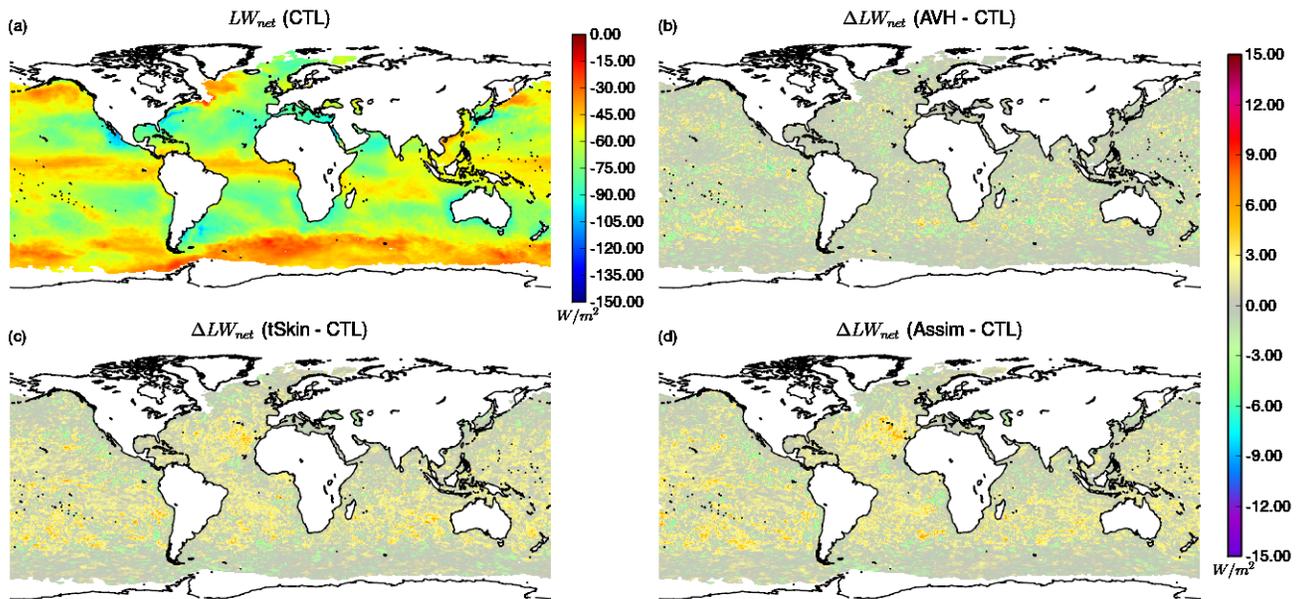
Figure 11: Same as in Fig. 10 but for the net surface longwave radiation LW_{net}.
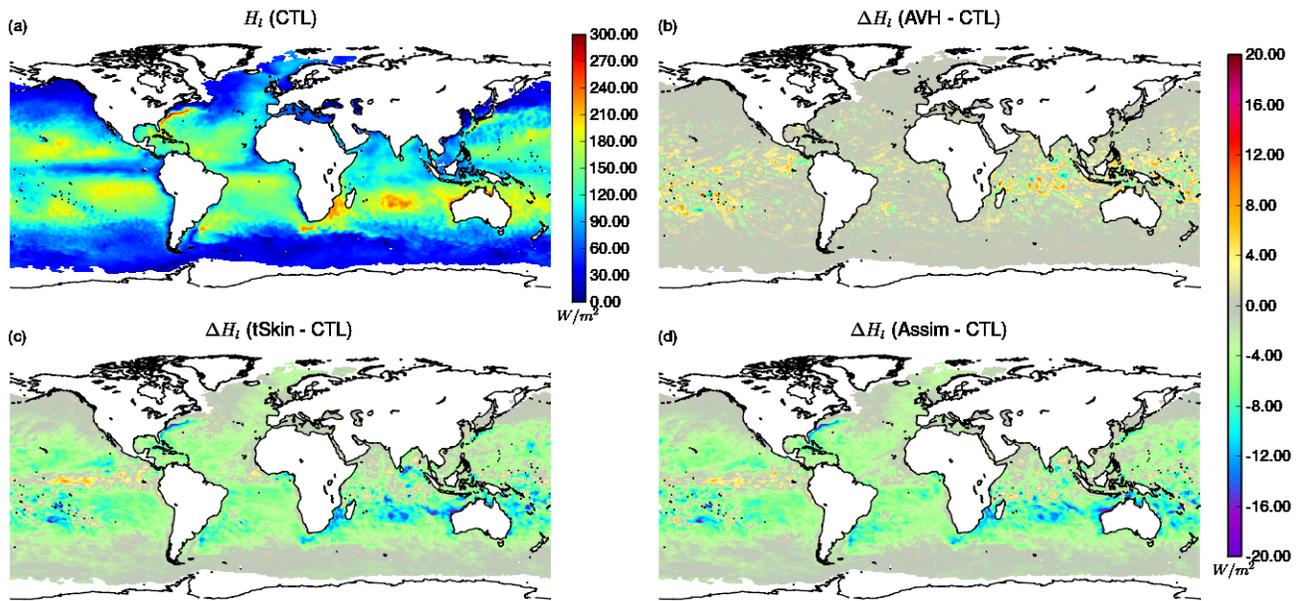
Figure 12: Same as in Fig. 10 but for the net latent heat flux H_l at surface.
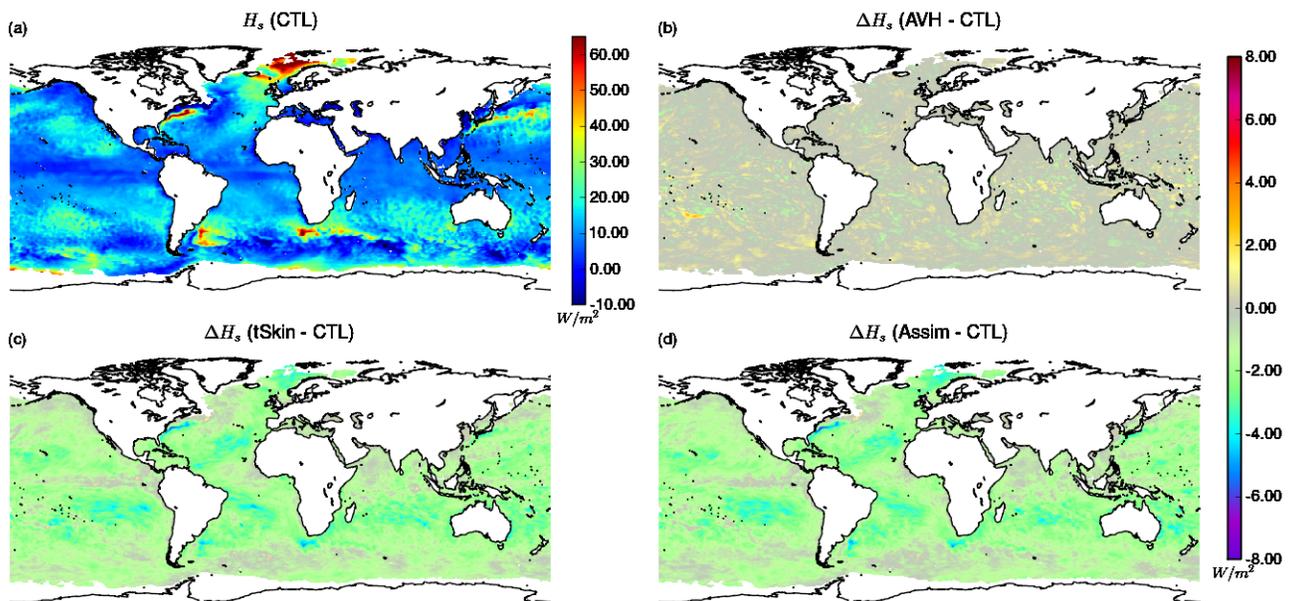
Figure 13: Same as in Fig. 10 but for the net sensible heat flux H_s at surface.
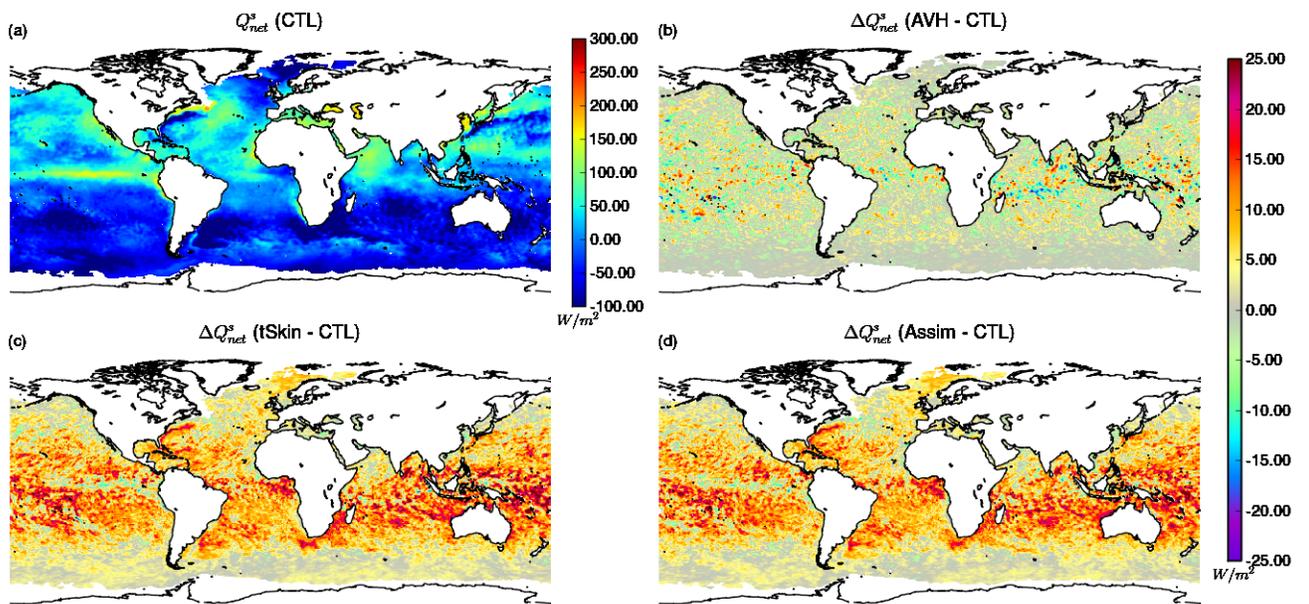
Figure 14: Same as in Fig. 10 but for the net heat flux Q_{net}^s at surface.
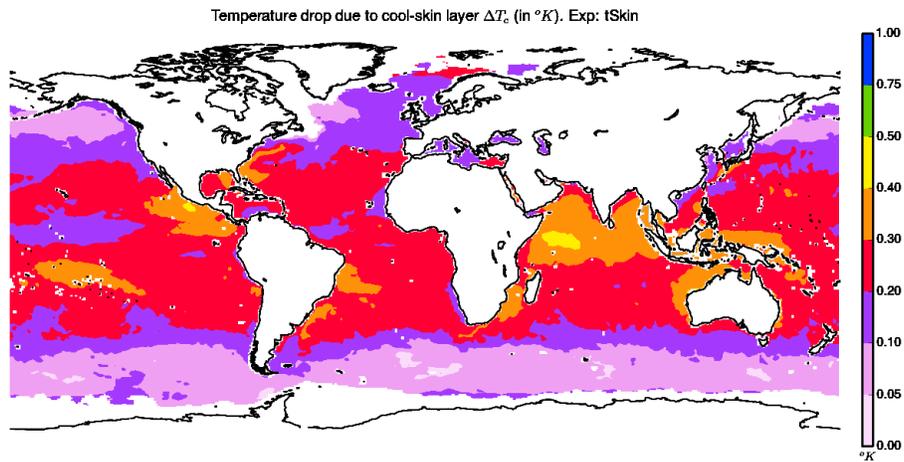
Figure 15: April 2012 monthly mean of the temperature drop ΔT_c (in ^oK) due to the cool-skin layer for the tSkin experiment. Land and sea ice have been masked.
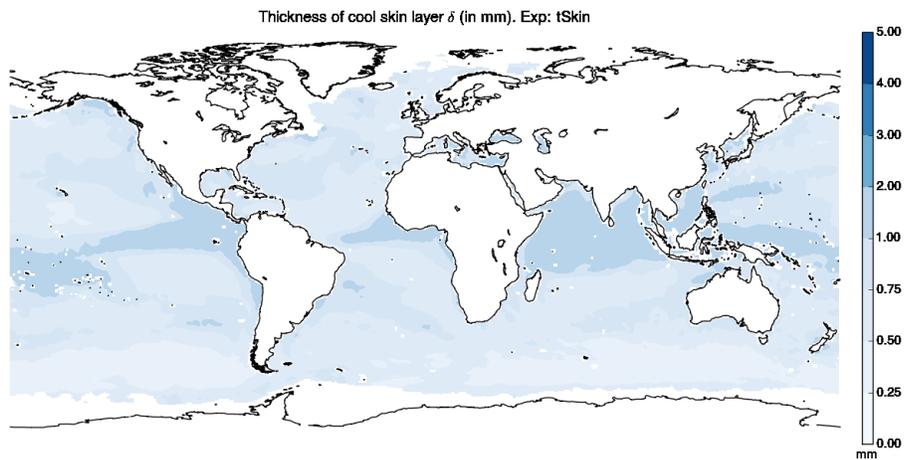
Figure 16: Same as in Fig. 15 but plot is for the depth of the cool-skin layer δ (in mm).
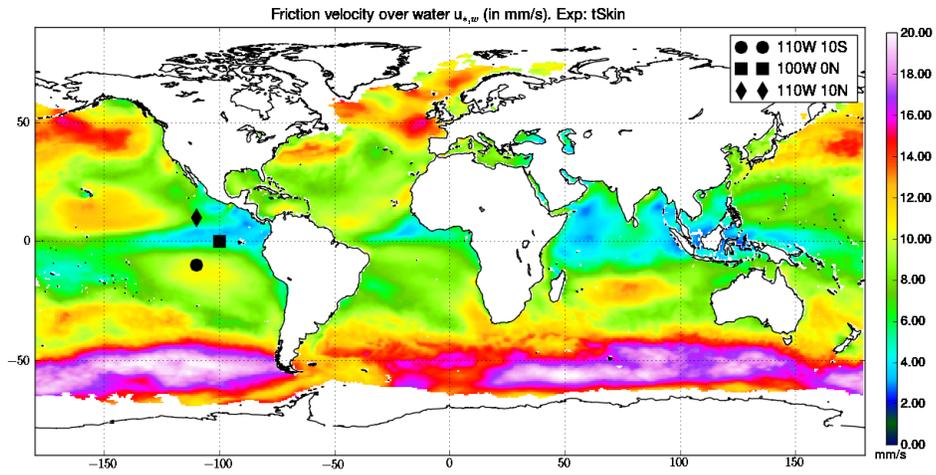
Figure 17: Same as in Fig. 15 but plot is for the friction velocity over water $u_{*,w}$ (in mm/s). Three locations at (110W, 10S), (100W, Eq.), and (110W, 10N) have been marked using a filled circle, square and diamond, respectively.
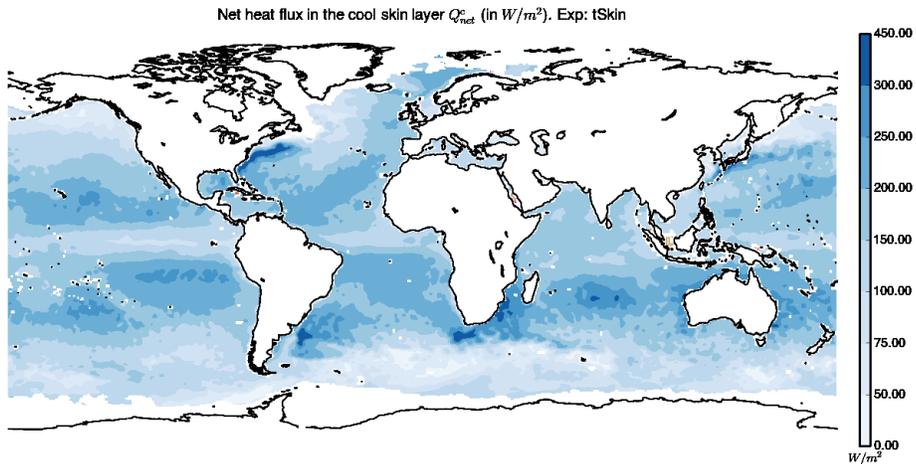
Figure 18: Same as in Fig. 15 but plot is for the net heat flux in the cool skin layer Q_{net}^c (in W/m^2).
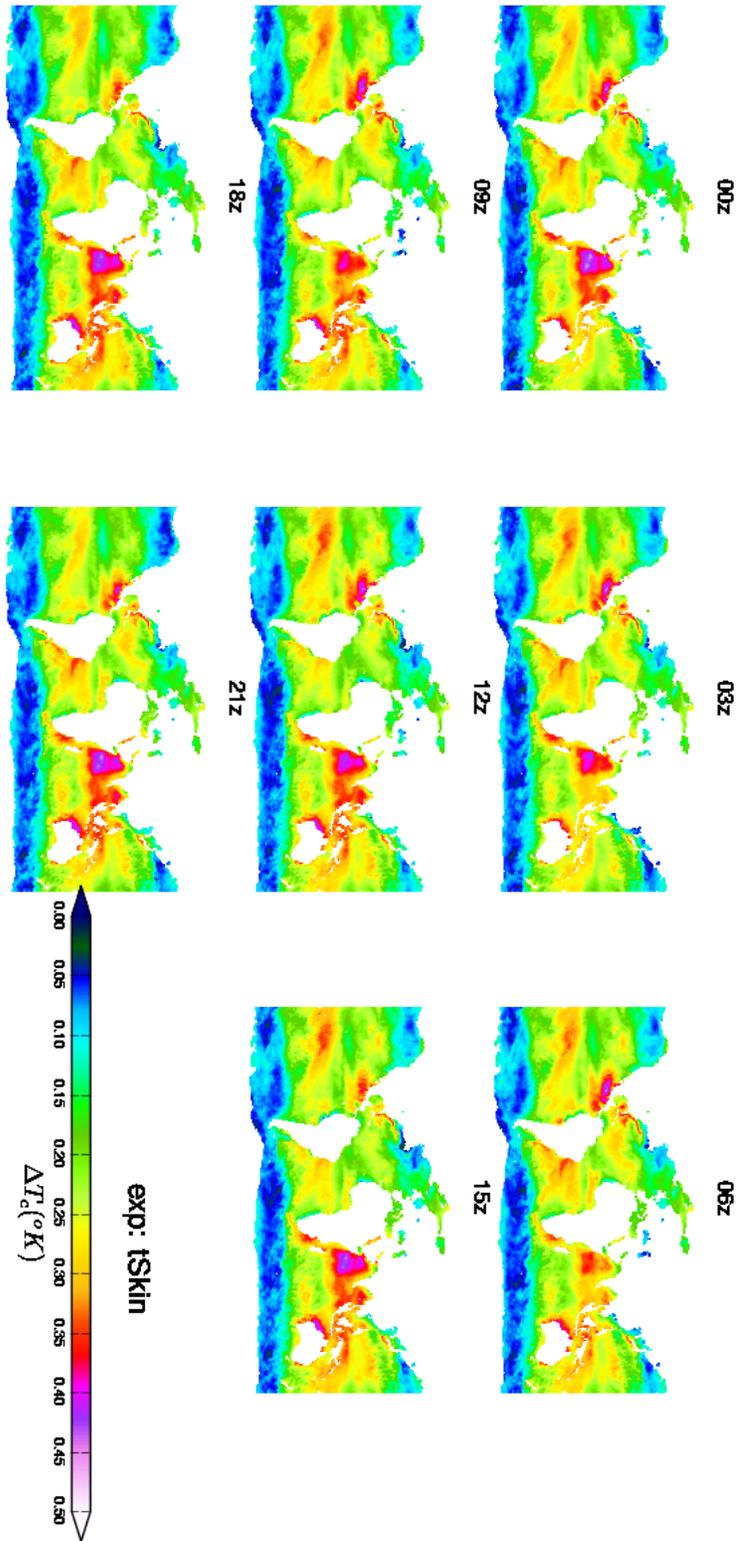
Figure 19: April 2012 monthly mean diurnal variation in ΔT_c (^oK) for the tSkin experiment. Diurnal variation can be seen by comparing ΔT_c at different synoptic times, for instance in the Arabian Sea/Indian Ocean.
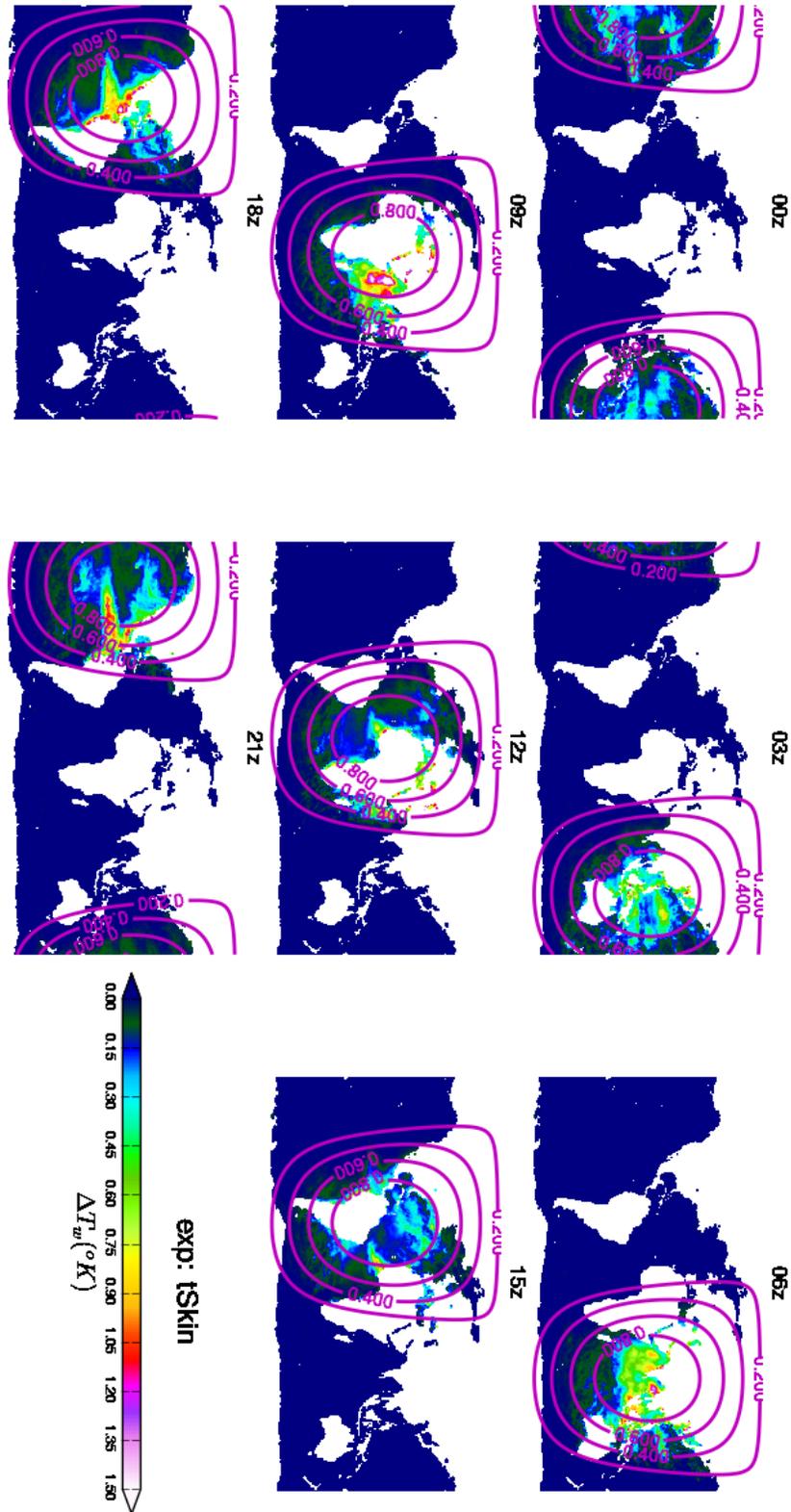
Figure 20: April 2012 monthly mean diurnal variation in ΔT_w (^oK) for the tSkin experiment. The magenta colored contour lines show the cosine of the solar zenith angle.
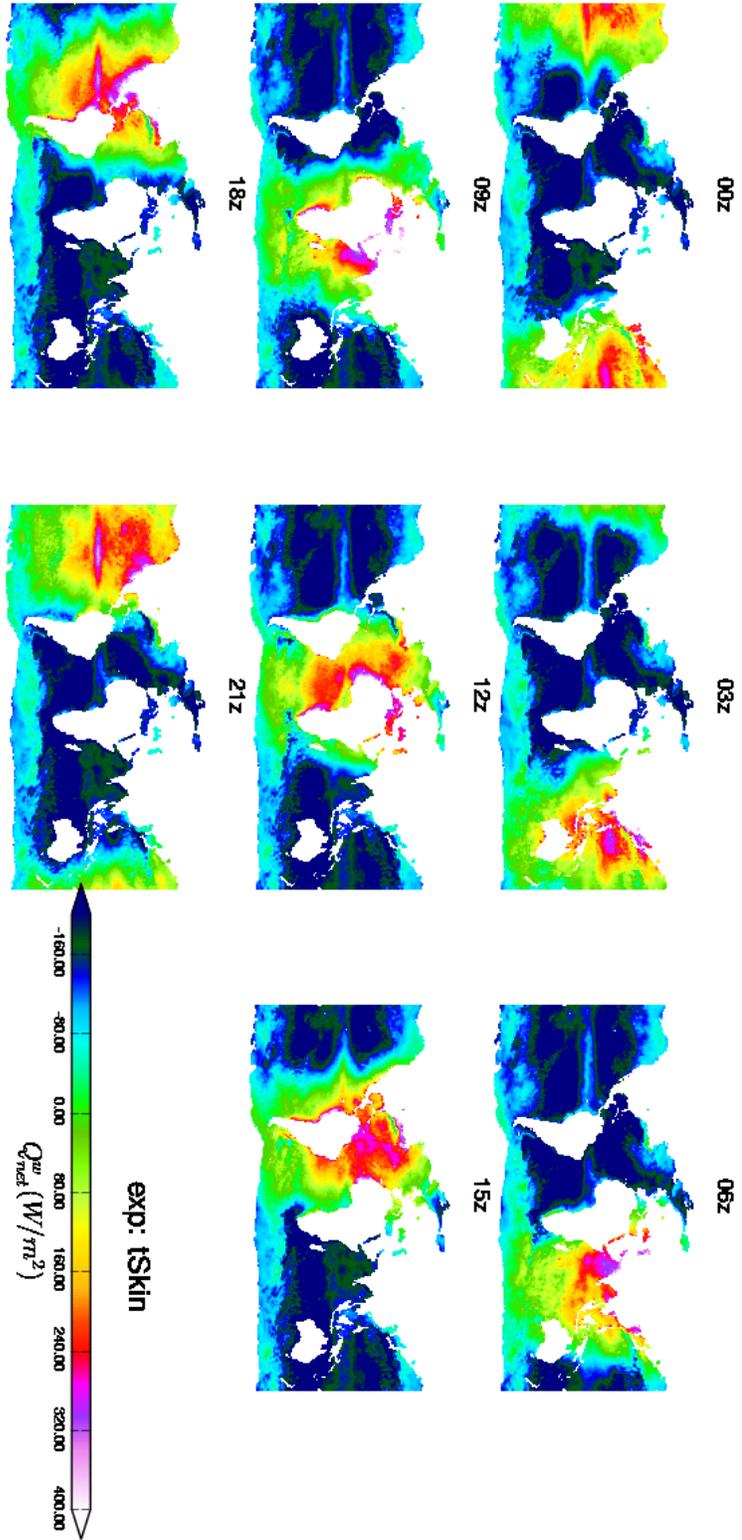
Figure 21: Same as in Fig. 19 but for the net heat flux Q_{net}^w in the warm layer (in W/m^2).
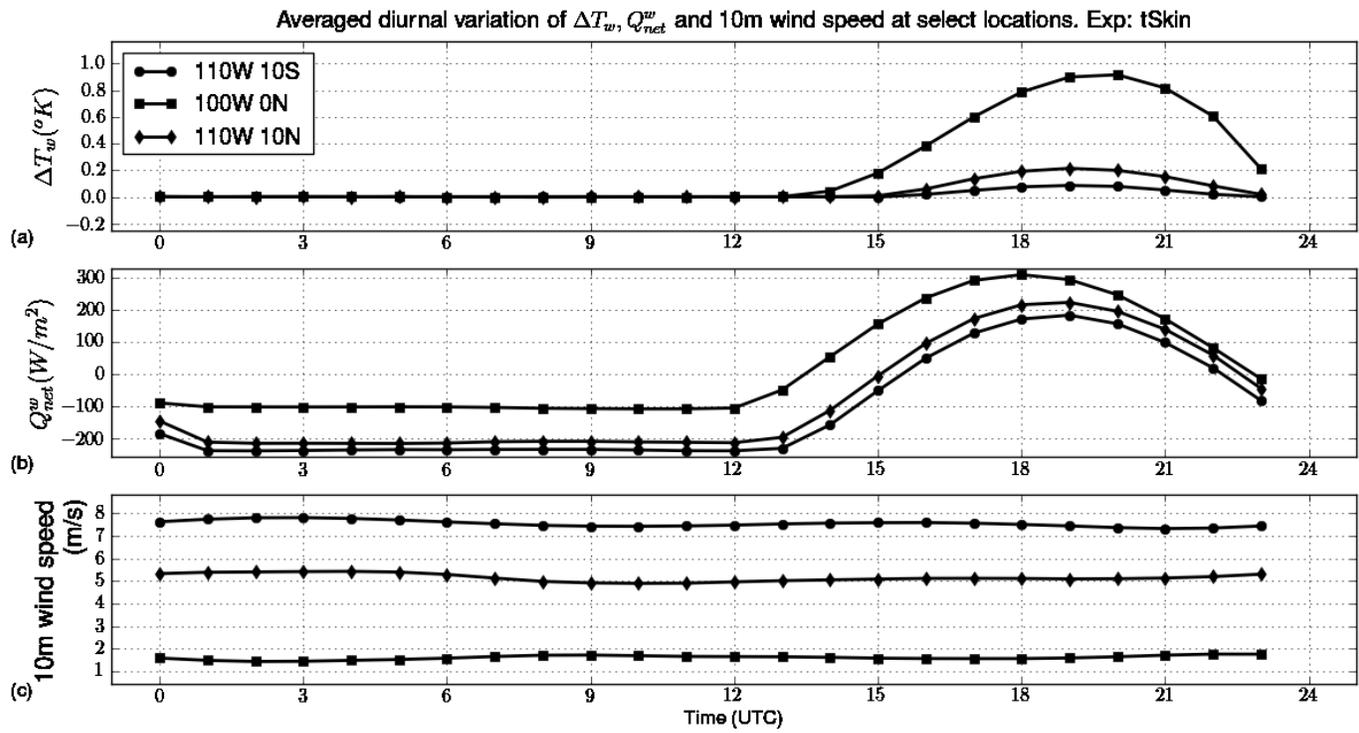
Figure 22: Monthly-averaged diurnal variation of $\Delta T_w, Q^w_{net}$ and 10m wind speed at the tropical locations marked in Fig. 17. Lowest wind speed is at (100W, 0N), where the peak $\Delta T_w \sim 1^o K$ and the minimum is $0.2^o K$ after sunset. The other locations have $\sim 100 W/m^2$ less net heat flux and higher wind speeds, with a maximum $\Delta T_w \sim 0.2^o K$ and with a ΔT_w that approaches zero soon after $Q^w_{net} \rightarrow 0$.
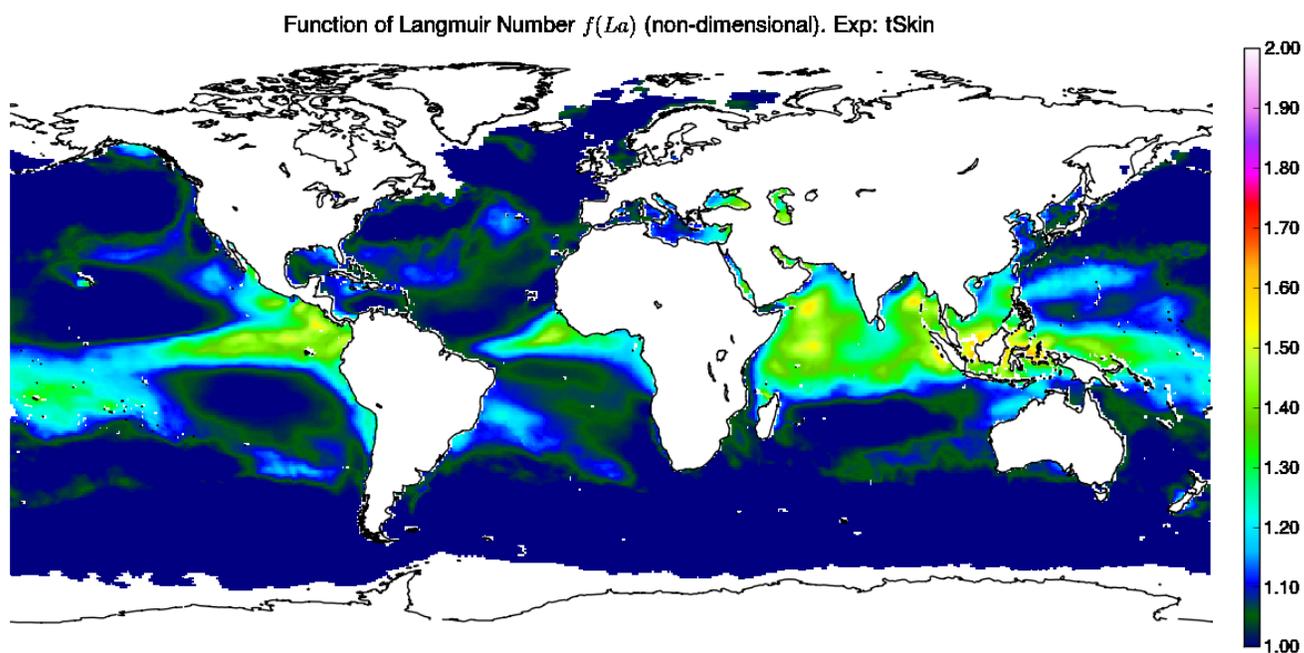
Figure 23: April 2012 monthly mean value of the function of the Langmuir number (La defined in section 3.2): $f(La) = La^{-2/3}$ for the tSkin experiment.
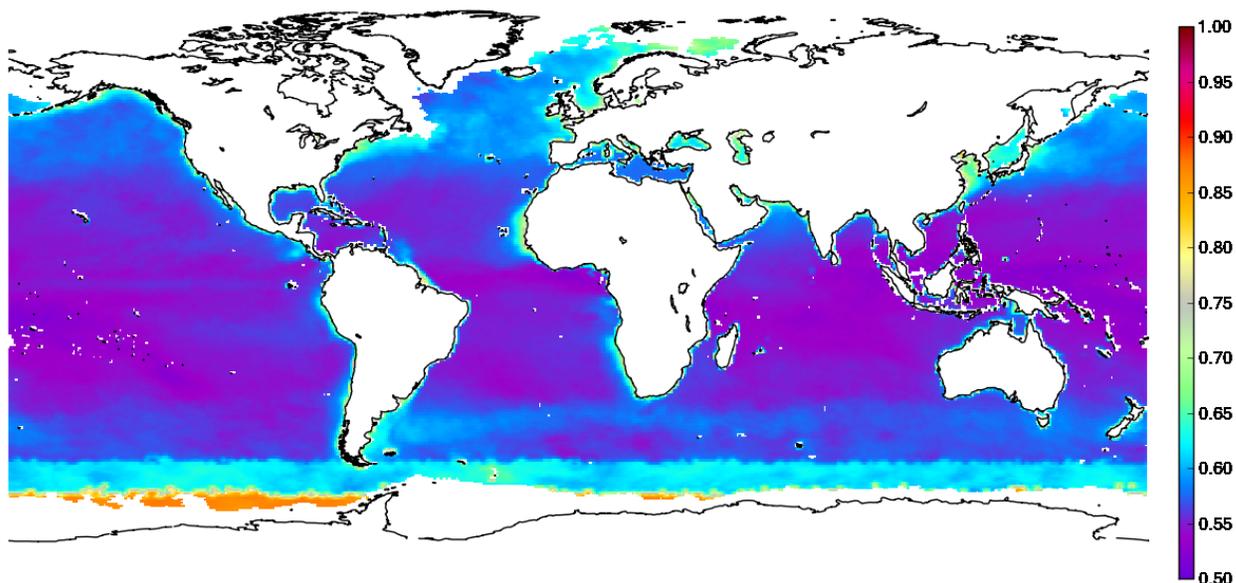
Figure 24: Same as in Fig. 23 but plot is for the ratio between net shortwave radiation absorbed in the warm layer $SW_{net}^w(z = d)$ to that at the surface SW_{net}^s.
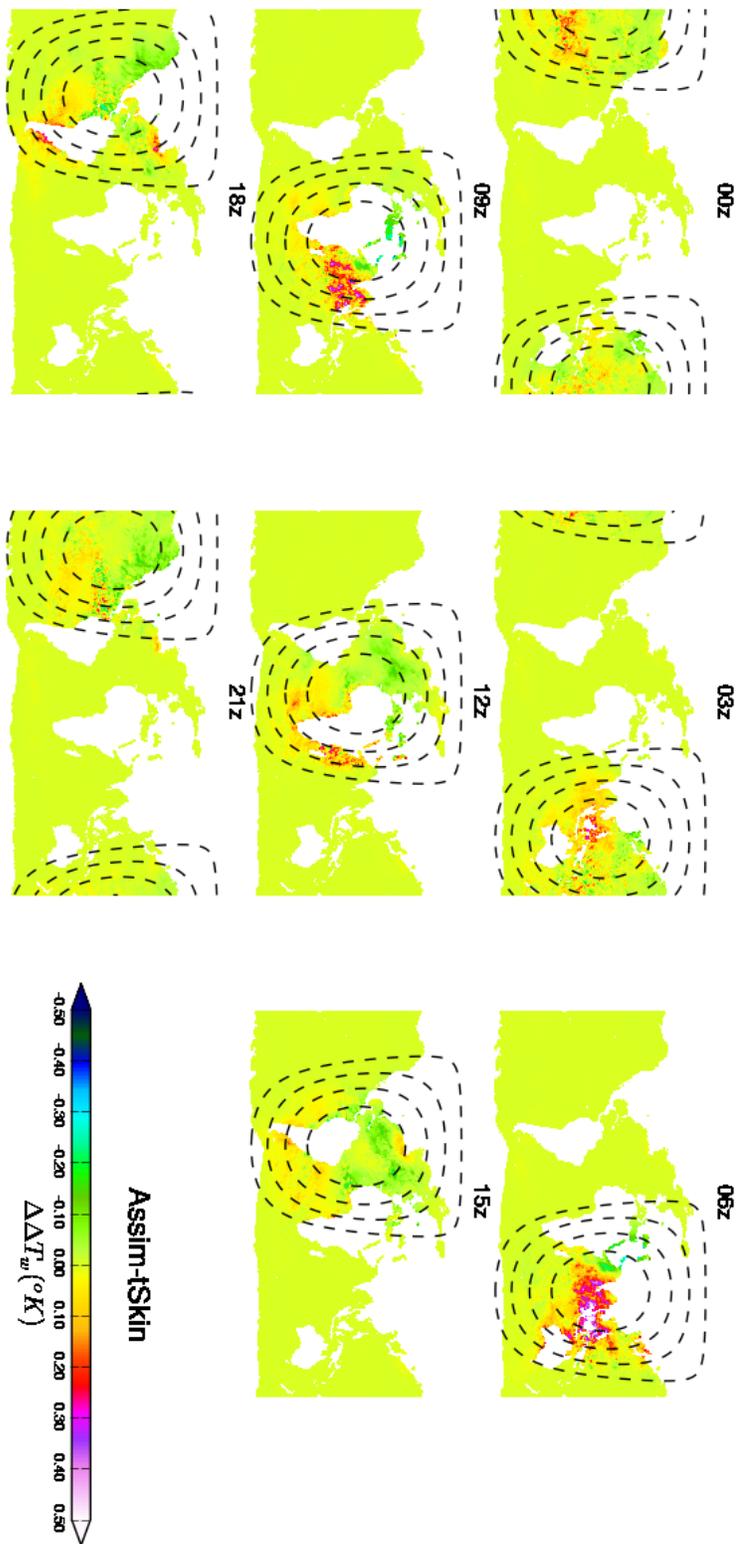
Figure 25: Monthly mean difference in ΔT_w (^oK) between the Assim and tSkin experiments.
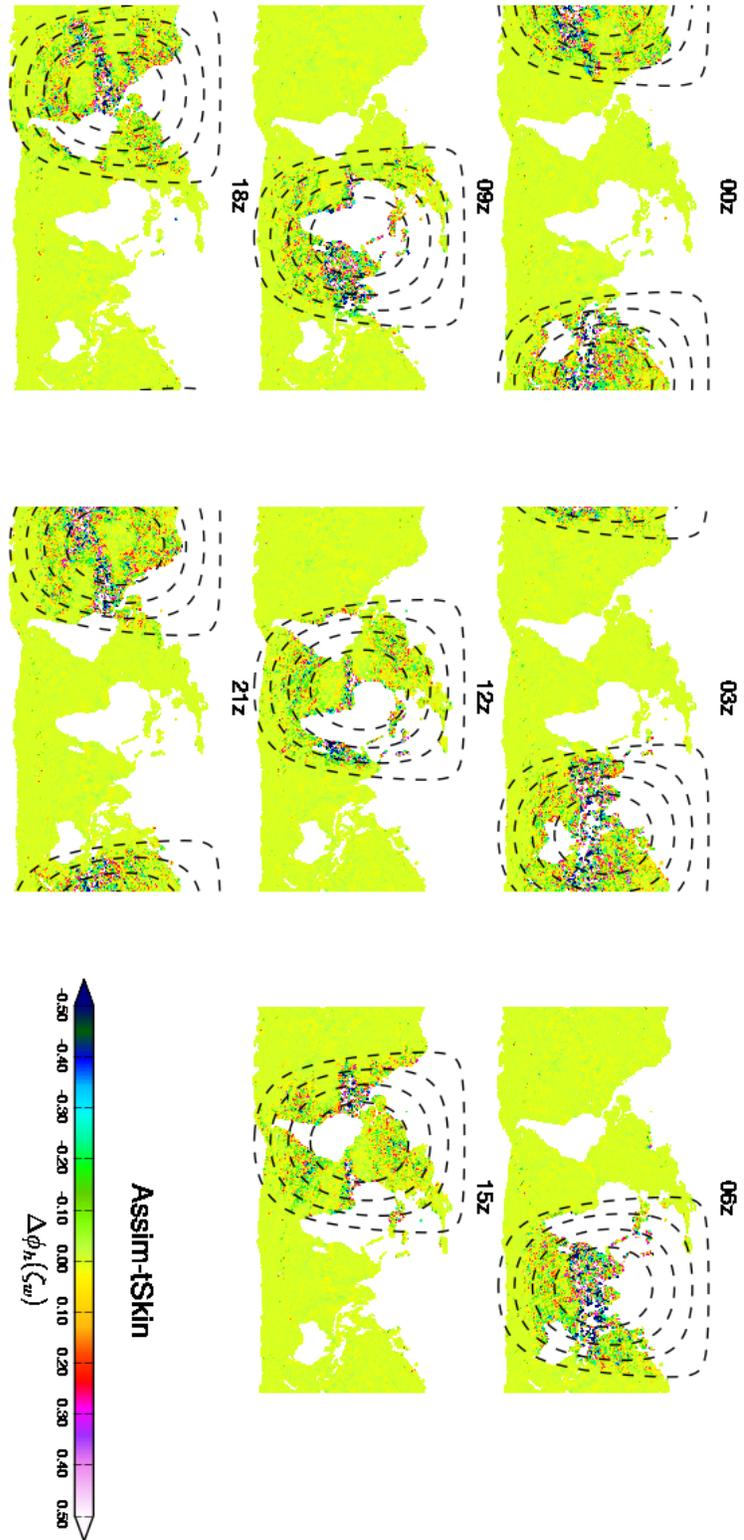
Figure 26: Same as in Fig. 25 but for the non-dimensional similarity function $\phi_h(\zeta)$.
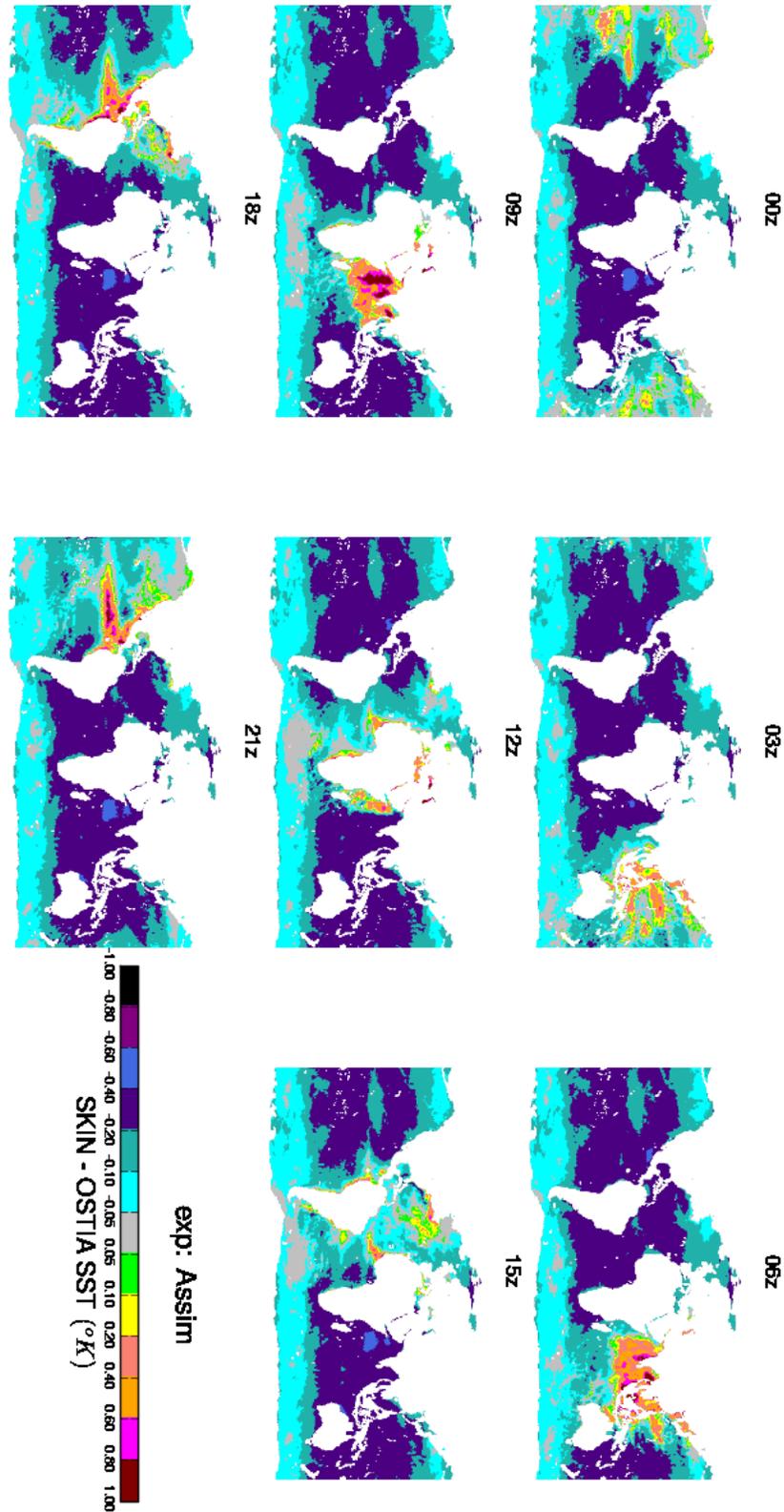
Figure 27: April 2012 monthly mean diurnal variation of difference between skin and OSTIA SSTs ($\mathbf{T_s}$-T_d) for the Assim experiment.
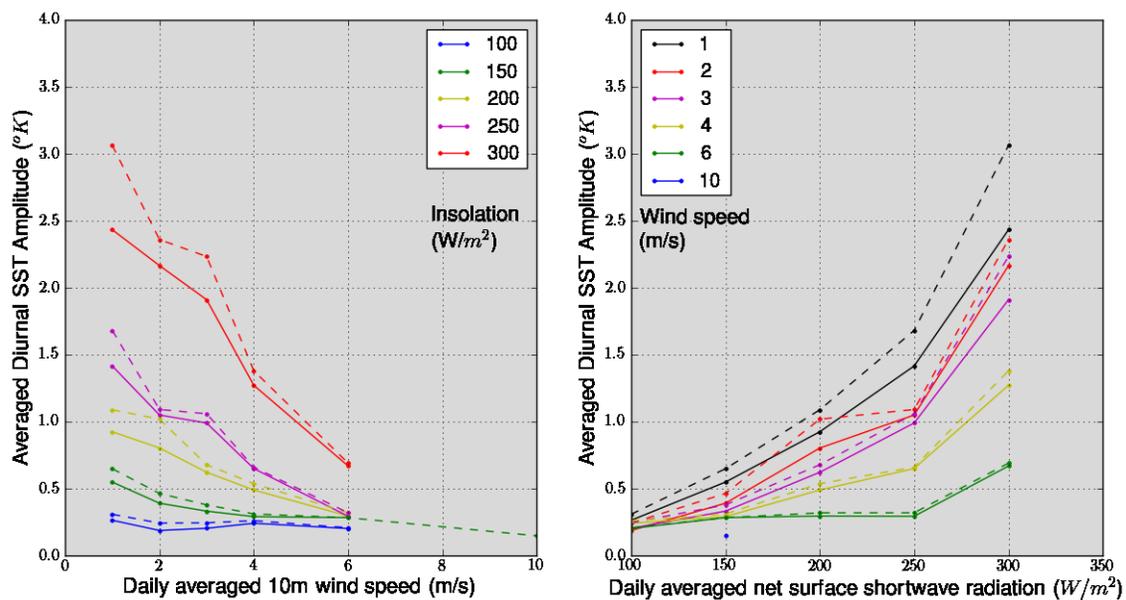
Figure 28: Averaged DSA as a function of 10m wind speed and insolation for Apr 2012. Solid (dashed) lines are for tSkin (Assim) experiment. Binning intervals for wind speed and insolation are 0.2 m/s and 10 W/m^2 respectively. Data is plotted only if sample size is > 100.
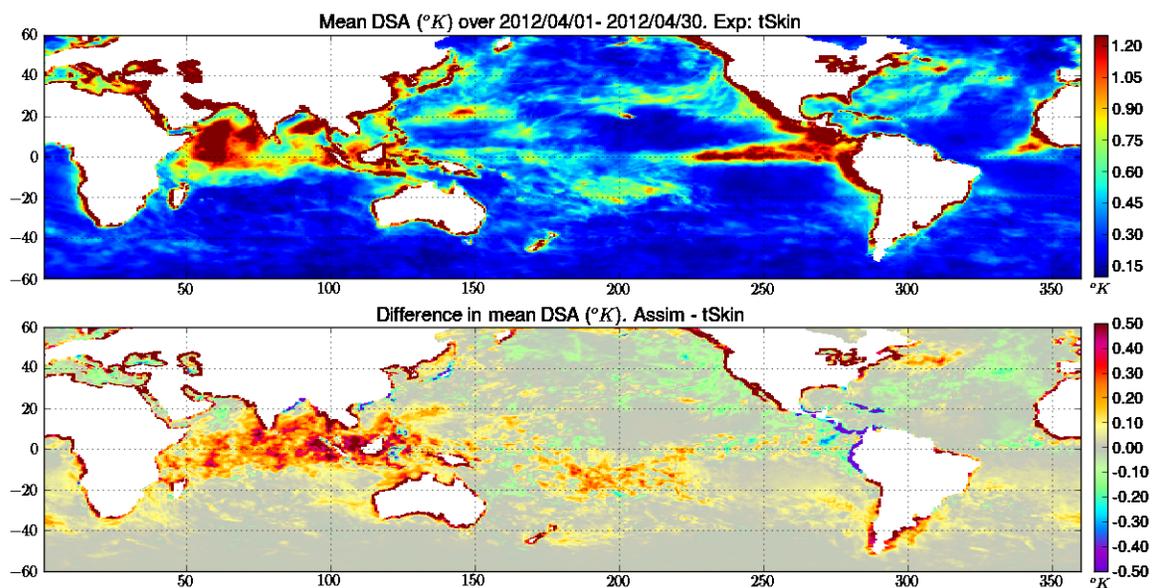
Figure 29: Spatial map of mean DSA. Top panel is for tSkin and bottom panel is difference between Assim and tSkin experiments.
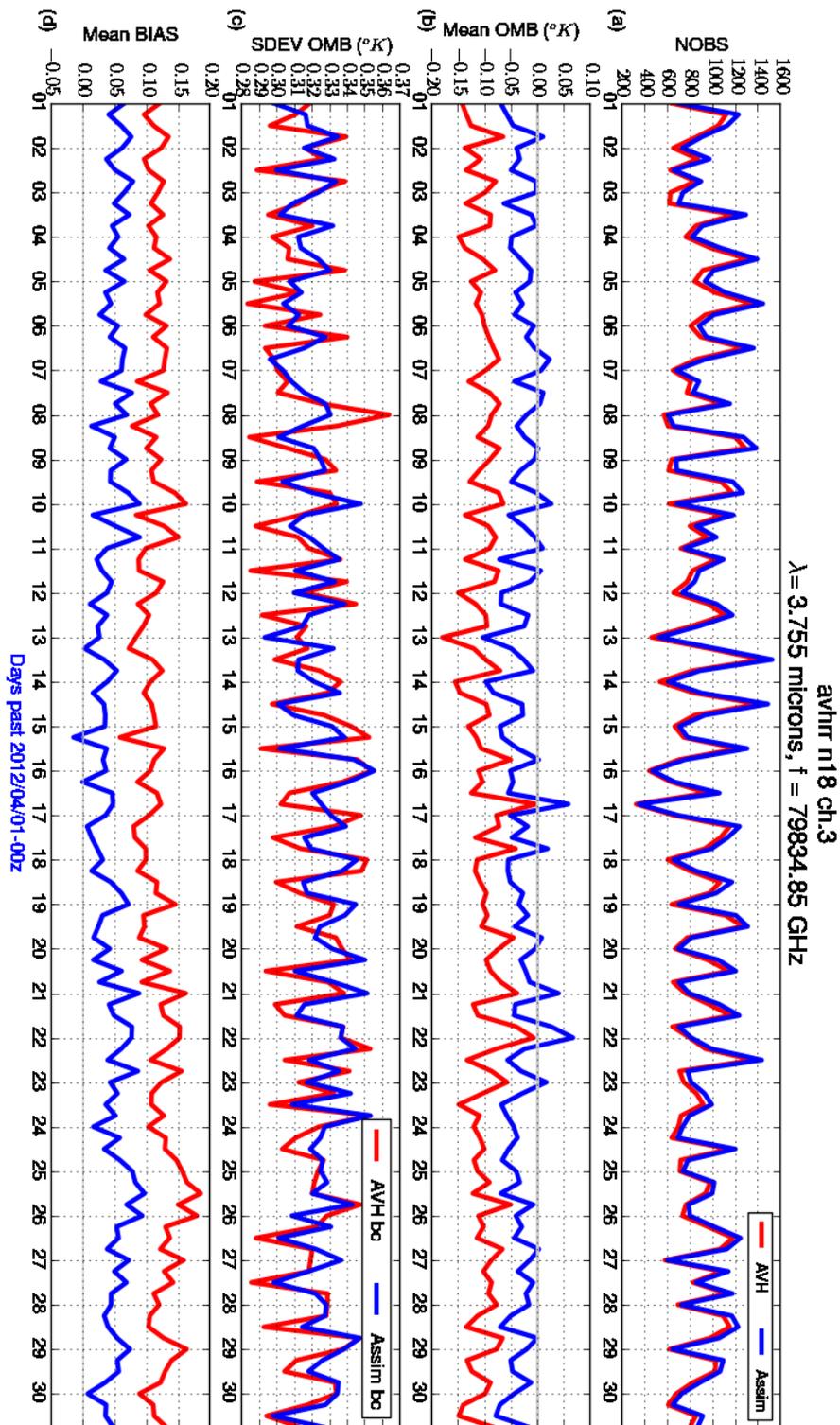
Figure 30: Time series of the global (ocean only) 6-hourly OMB statistics for the AVHRR channel 3 on board NOAA-18. (a) Number of assimilated observations; (b), (c) Mean and standard deviation (SDEV) of bias-corrected OMB; (d) Mean bias correction = OMB (bias corrected) - OMB (before bias correction). Experiment AVH is plotted in red and Assim in blue.

51

(a) CTL
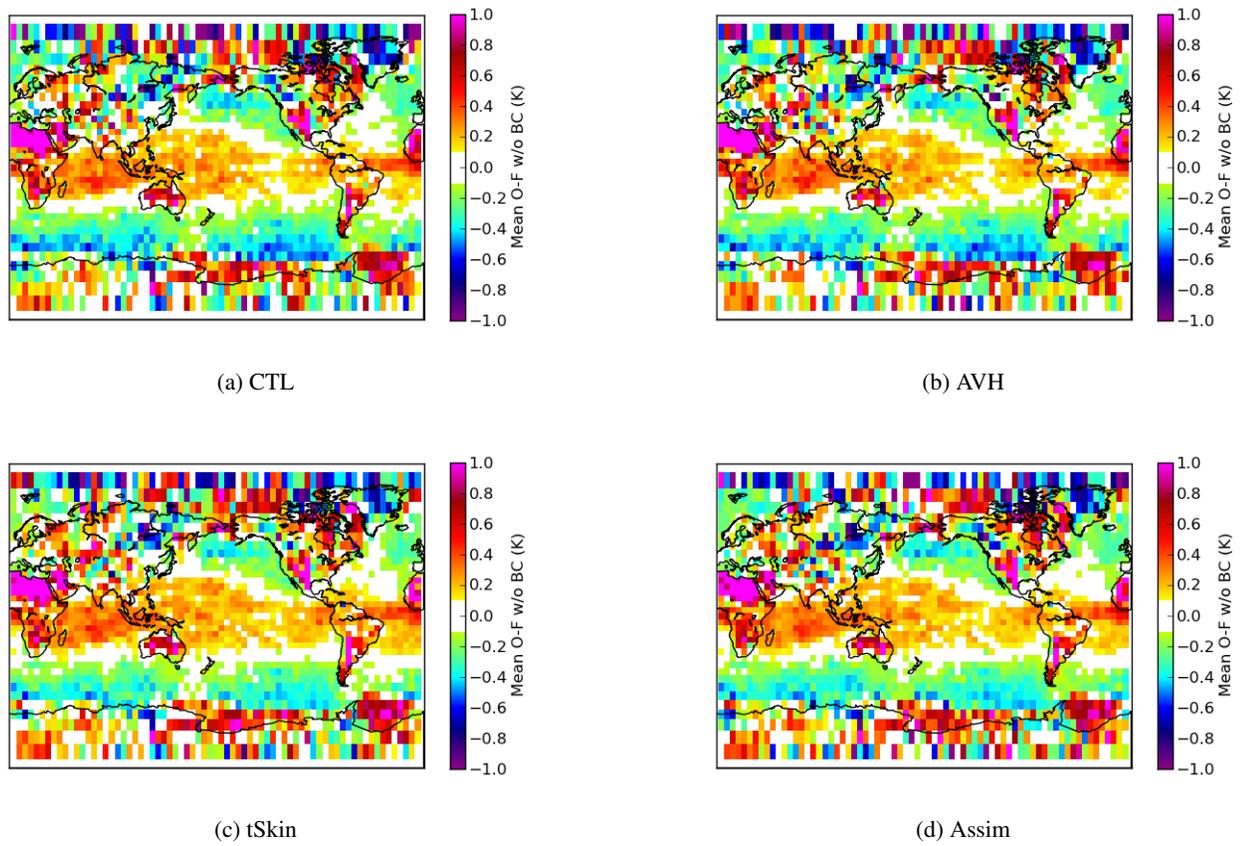
(b) AVH

(c) tSkin

(d) Assim

Figure 31: Monthly mean of the OMB (before bias correction) for Ch 123 (number 587 in full channel number space) of the Atmospheric Infrared Sounder (AIRS) on AQUA satellite: (a) CTL, (b) AVH, (c) tSKin, (d) Assim. This is a surface-sensitive window channel, measuring at wavenumber of $843.9 cm^{-1}$. The monthly mean has been computed by binning to $5^o \times 5^o$ uniform grid.
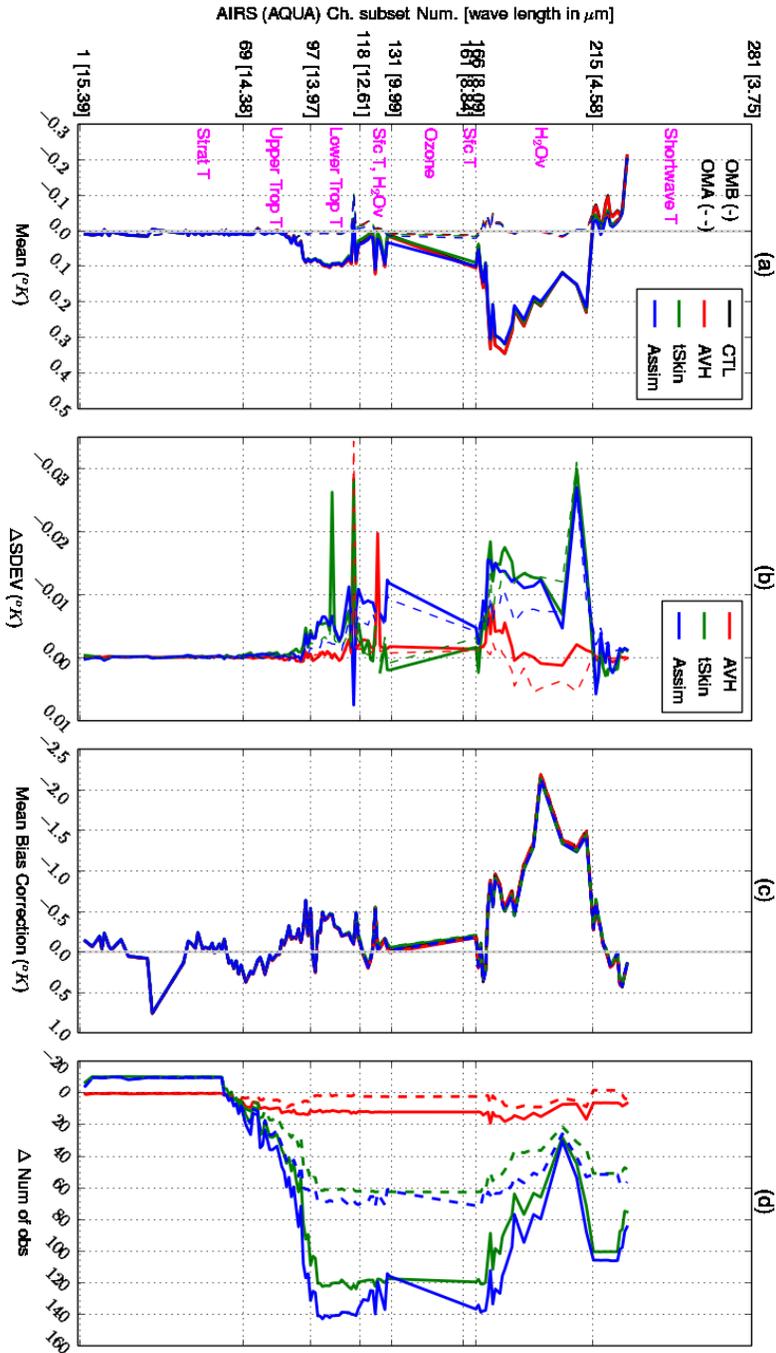
Figure 32: Monthly-averaged OMB statistics for the AIRS on AQUA satellite, with statistics computed only over water. (left to right) Panels (a) and (c) show the mean bias-corrected OMB and mean bias correction (defined in Fig. 30); (b) and (d) depict the difference (from CTL) in the bias corrected standard deviation (SDEV) of OMB and the number of observations, respectively. The ordinate is the same for all panels and is shown in (a). Solid (dashed) lines are for OMB (OMA). Panel (a) shows the approximate regions of the atmosphere where channels *peak*.
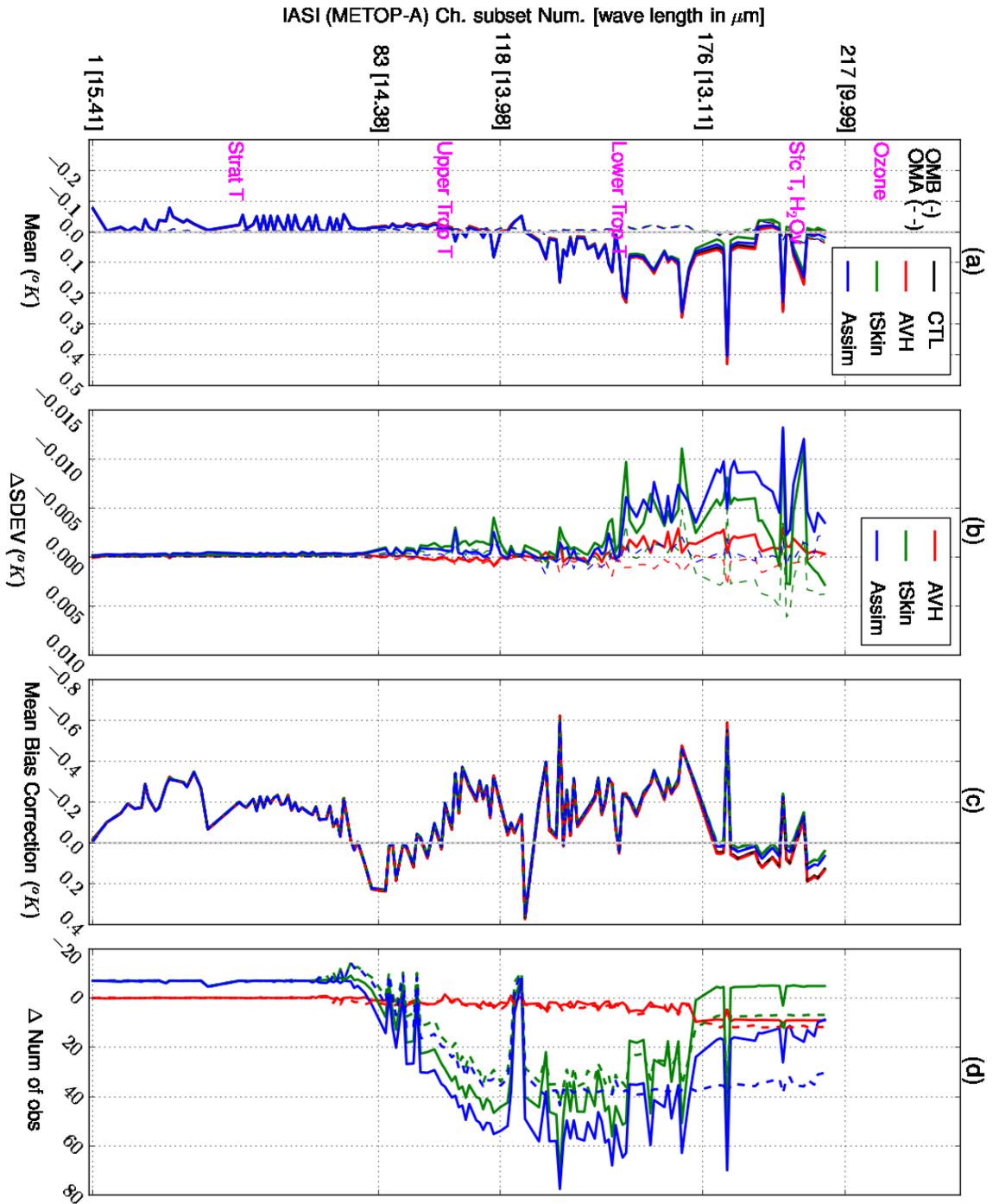
Figure 33: Same as in Fig.32 but for the Infrared Atmospheric Sounding Interferometer (IASI) on Metop-a satellite.
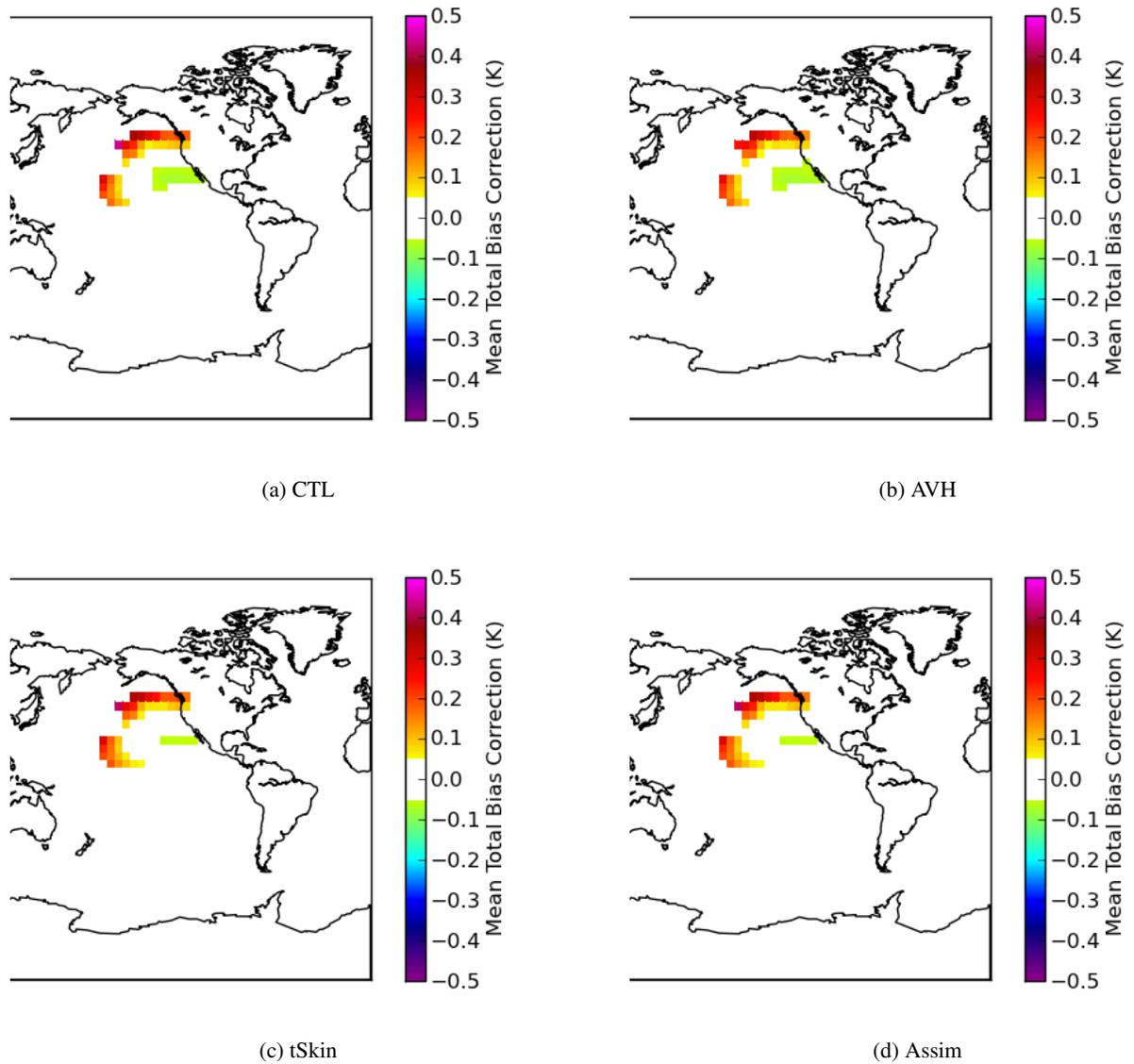
Figure 34: Monthly mean of the total bias correction (defined in Fig. 30 and binning to $5^o \times 5^o$ uniform grid) for 18 UTC analyses, and for Ch 8 of the first detector on GOES-15 satellite: (a) CTL, (b) AVH, (c) tSKin, (d) Assim. This is a surface-sensitive window channel, measuring at a wavenumber of $911.6 cm^{-1}$.
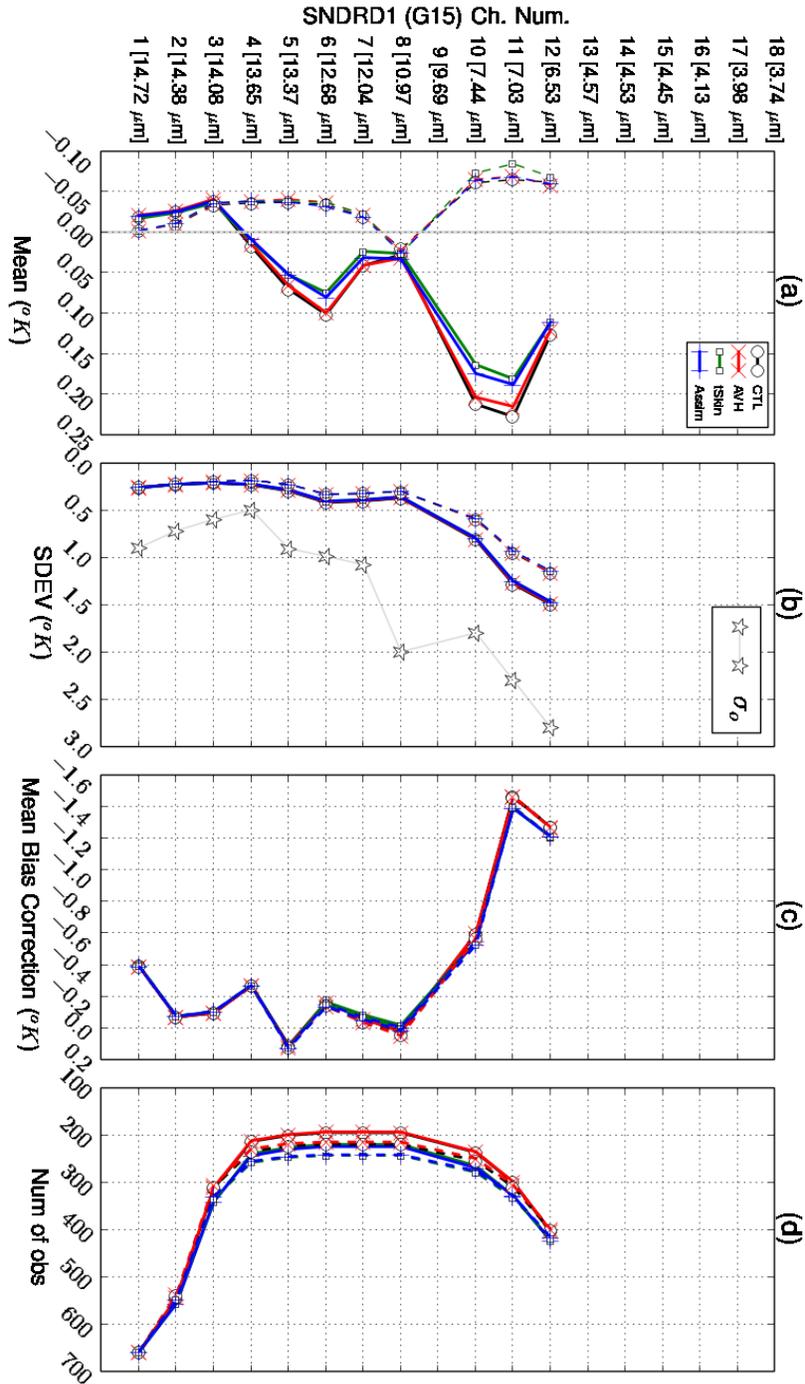
Figure 35: Monthly-averaged OMB statistics for the sounding (SNDR) channels on the the GOES-15 satellite, for the first detector (D1) and for assimilated channels only. (left to right) Panels (a) and (b) show the mean and standard deviation (SDEV) of bias-corrected OMB; (c) and (d) depict the mean bias correction (defined in Fig. 30) and the number of observations, respectively. The ordinate is same for all panels and is shown in (a). Solid (dashed) lines are for OMB (OMA); σ_o shown in (b) is the specified observational error variance. 56
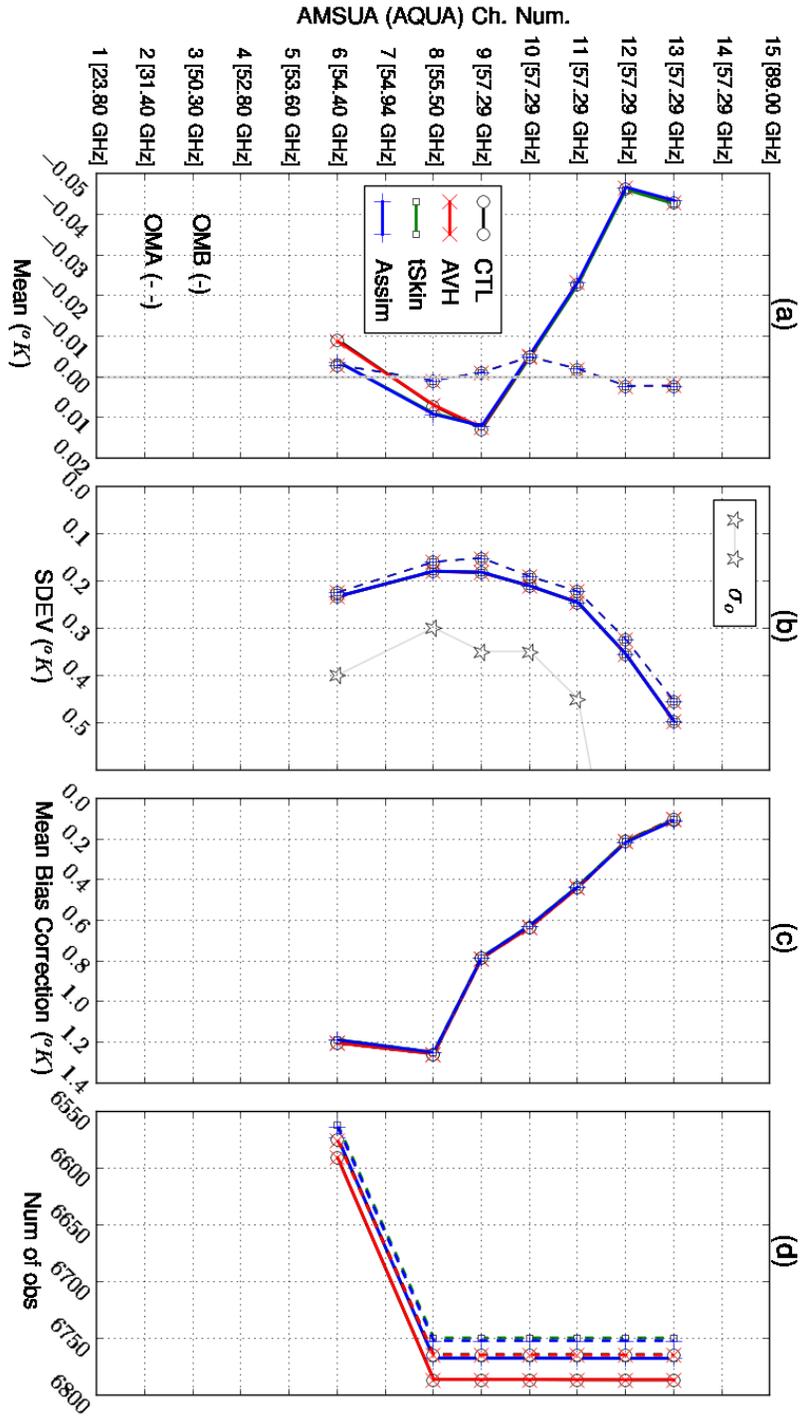
Figure 36: Same as in Fig. 35 but for the assimilated imager channels of Advanced Microwave Sounding Unit (AMSU)-A on AQUA satellite, with statistics computed only over water.
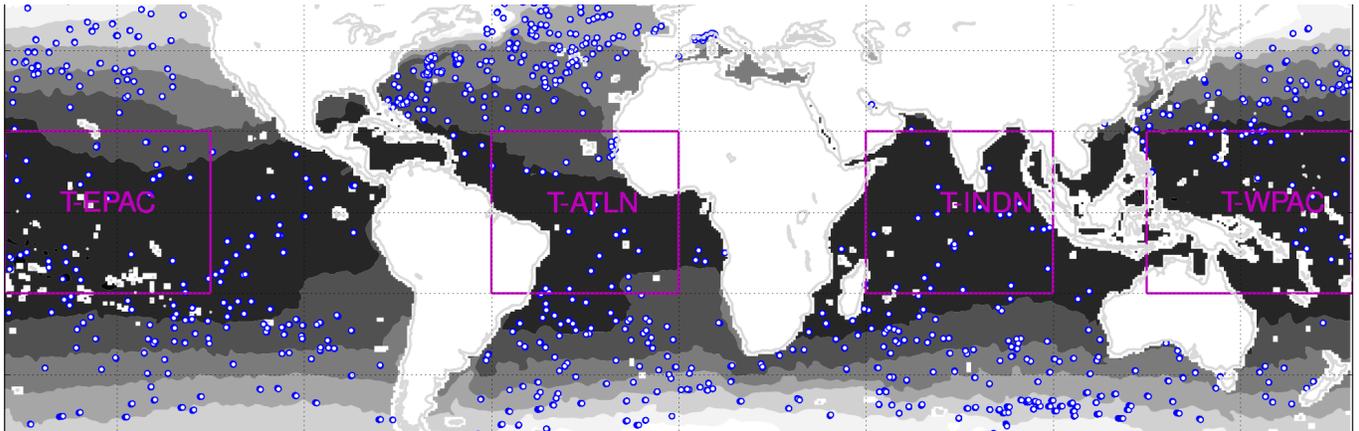
Figure 37: Locations of drifting buoys (on 01 April 2012 at 00UTC), plotted as blue dots. Basin-averaged OMB statistics were computed for the following regions in the tropics between 20S to 20N (right to left): (i) **T-WPAC**: 125E- 180E, (ii) **T-INDN**: 50E - 100E, (iii) **T-ATLN**: 50W - EQ, (iv) **T-EPAC**: 125W- 180W. OSTIA SST for the same date is plotted for reference purposes, to show the separation of fronts; hence the colorbar is not shown.
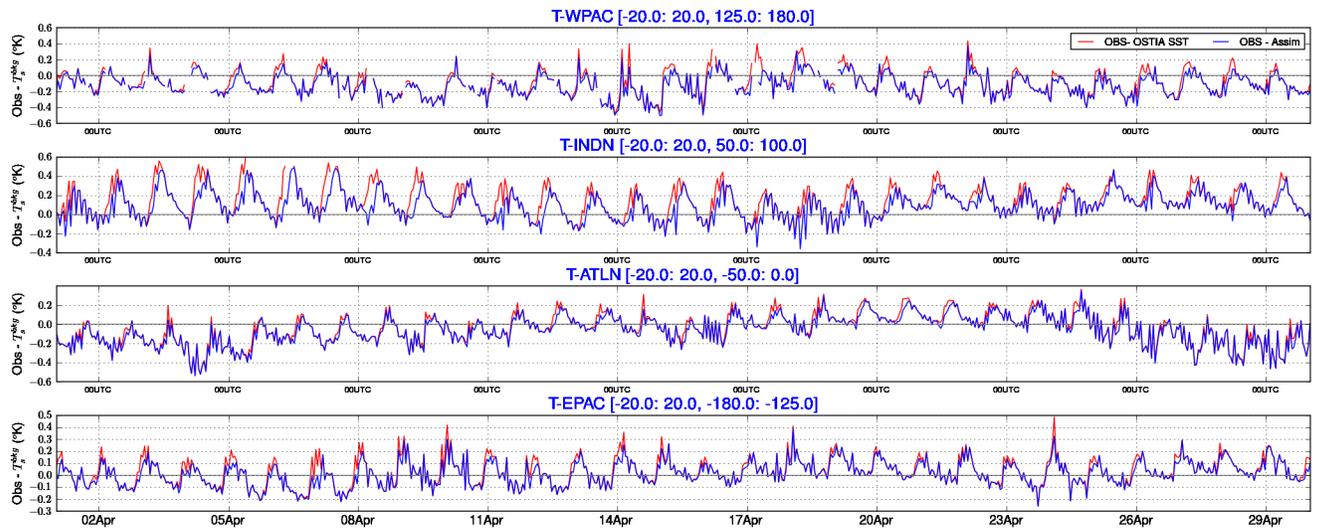
Figure 38: Time-series of the regional (shown in Fig. 37) averaged hourly differences between observed SST from drifting buoys and the temperature at 20cm depth from the Assim experiment (blue). Observation minus OSTIA SST is plotted for reference in red; these observations were withheld from analysis. Gaps at certain hours in the time-series (e.g., top panel (T-WPAC) on 04 Apr) are due to a lack of observed data and/or application of quality control.
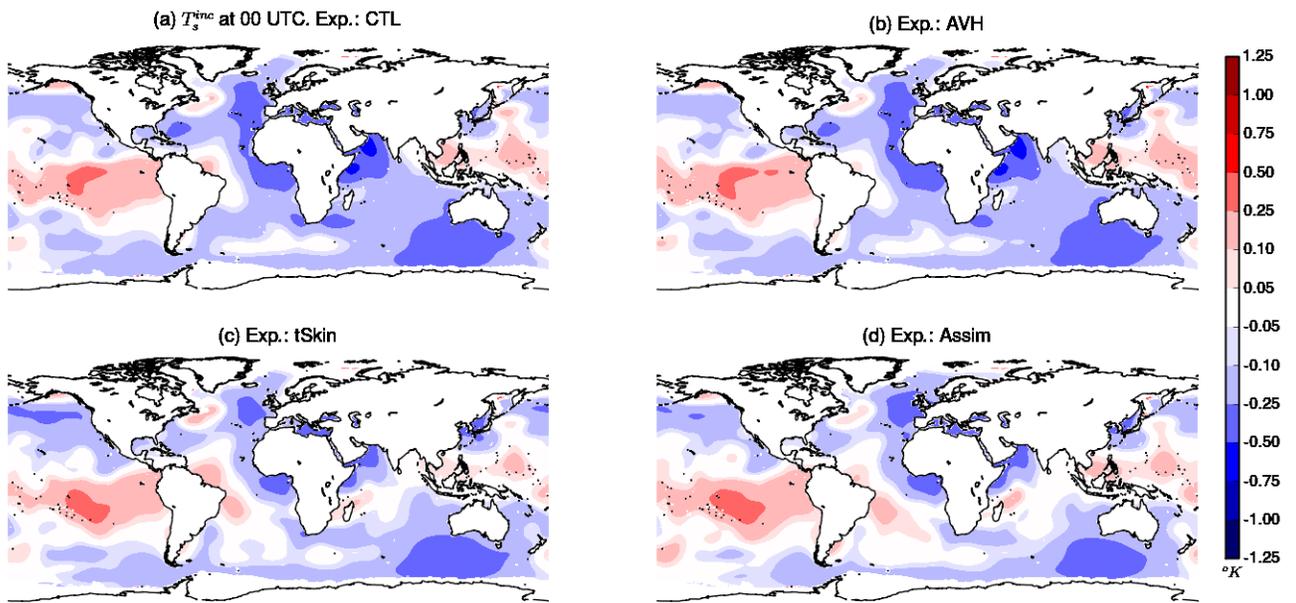
Figure 39: Monthly mean of the analysis increment in skin SST for the 00 UTC analyses: (a) CTL, (b) AVH, (c) tSkin, and (d) Assim. Land and sea ice regions have been masked.
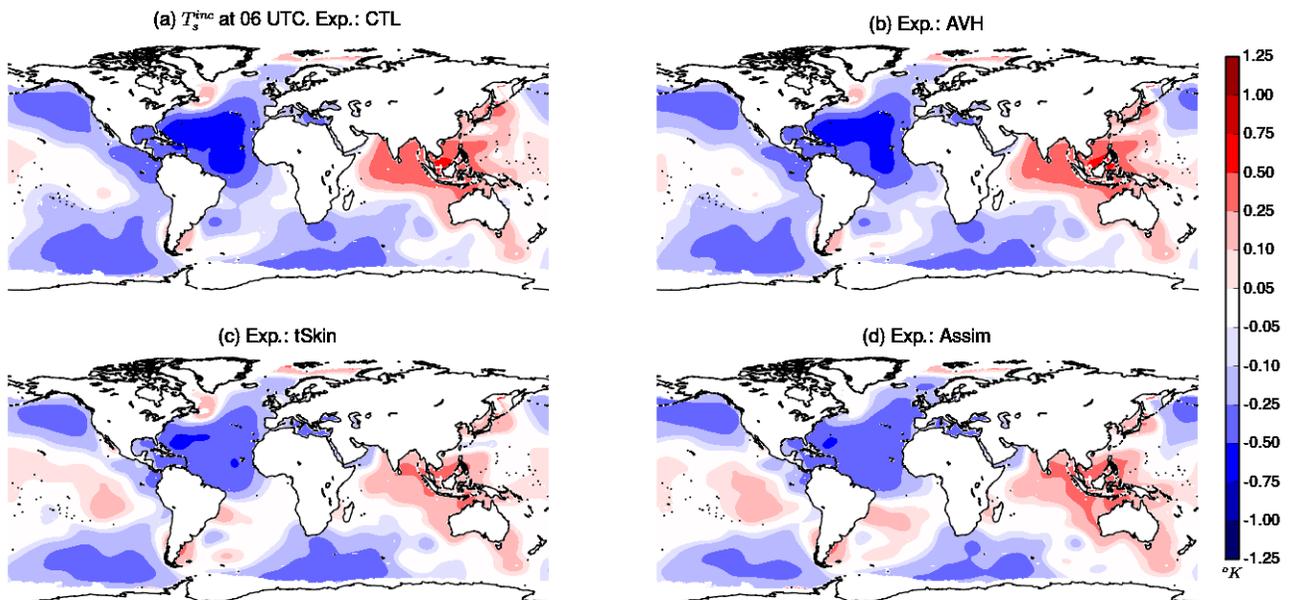
Figure 40: Same as in Fig. 39 but at 06 UTC
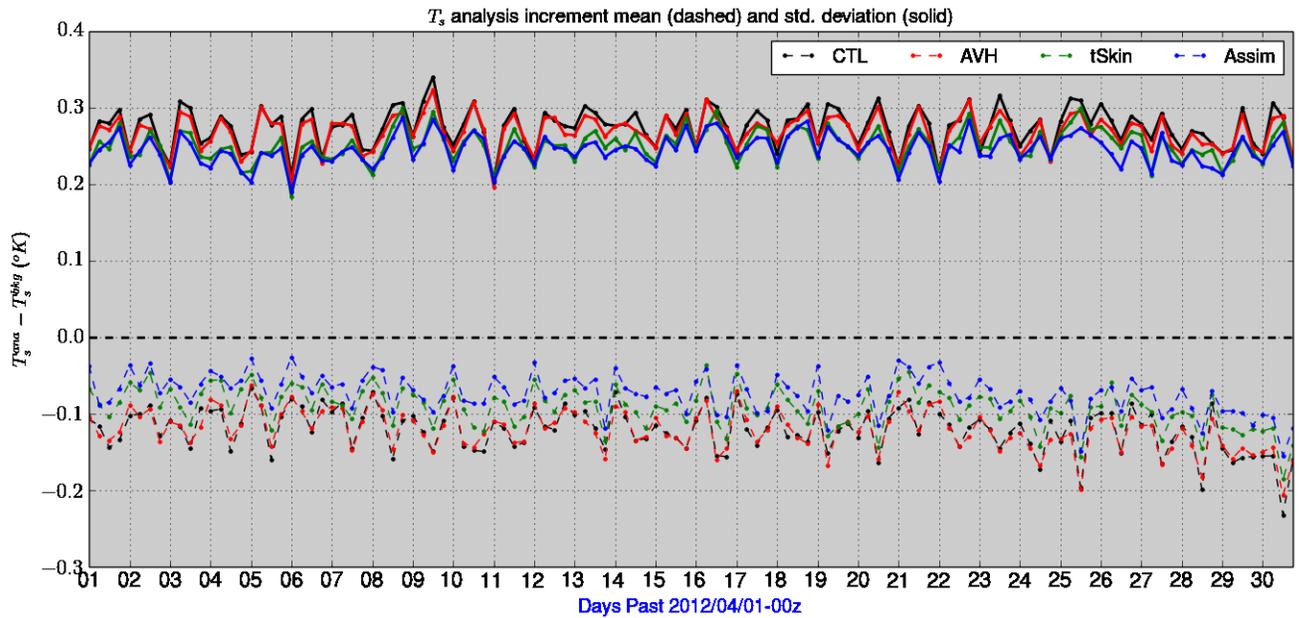
Figure 41: Time series of global mean (dashed lines) and standard deviation (solid lines) of 6-hourly **T$_s$** analysis increment for the CTL, AVH, tSkin and Assim experiments over open water analysis grid points.
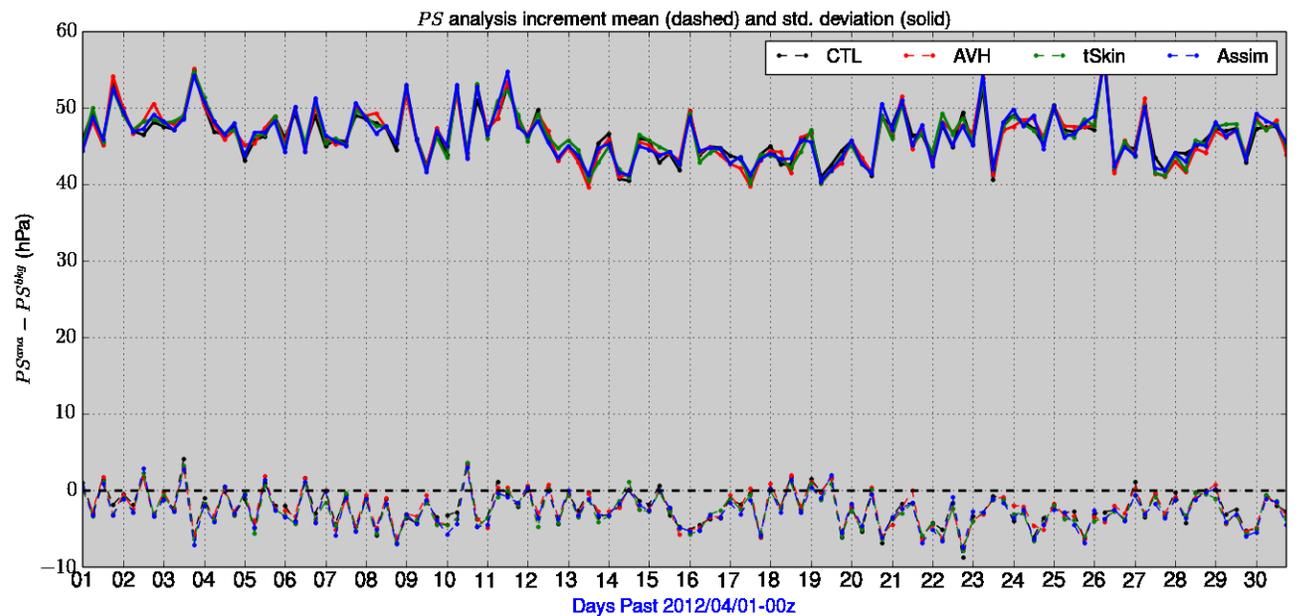
Figure 42: Same as in Fig. 41 but for the surface pressure (PS). Statistics are for global fields, computed over all surface types (not just over water) since PS increment is applied globally.
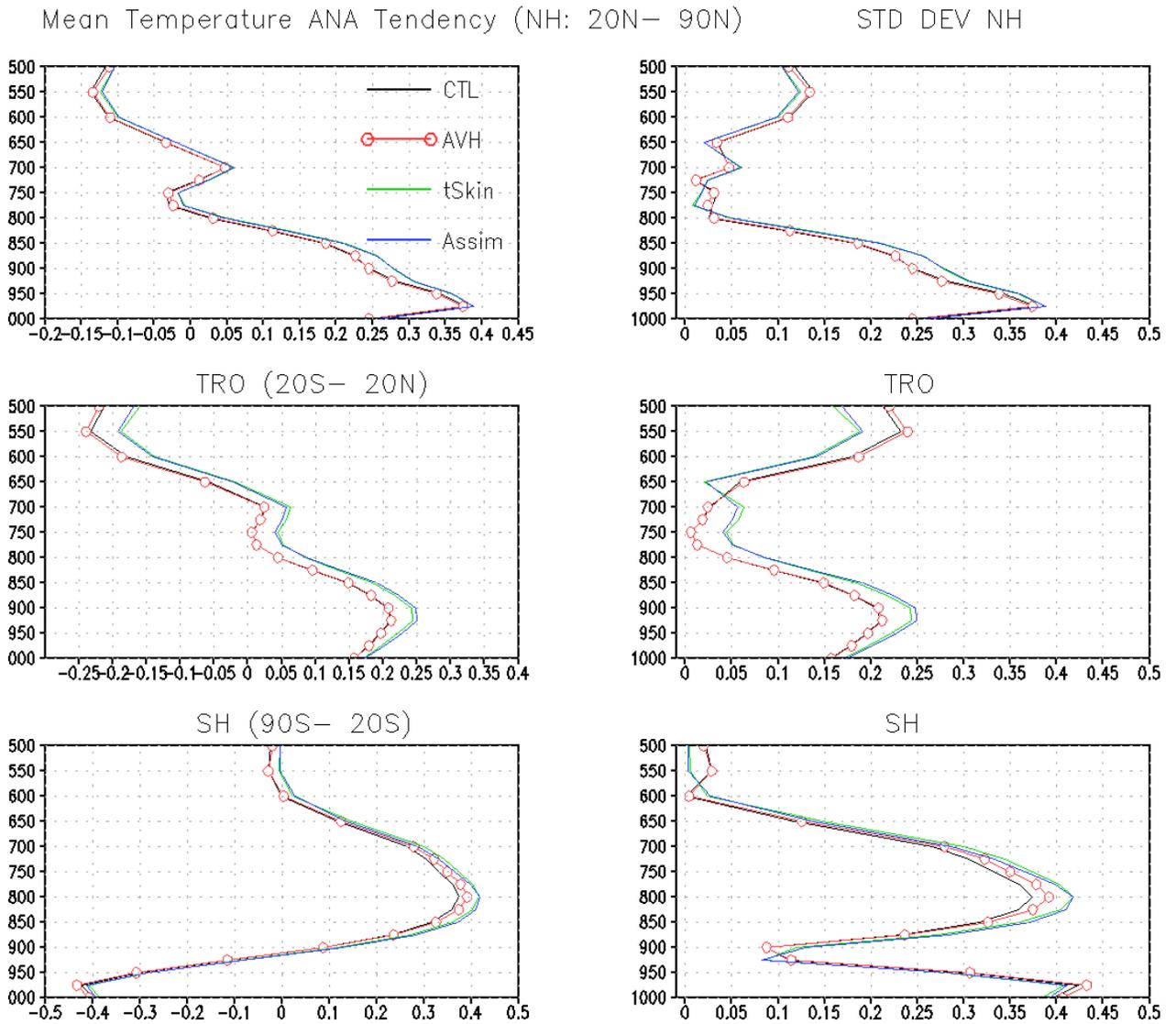
Figure 43: Comparison of zonal average of the monthly mean analysis tendency (increment divided by 6 hours) in temperature (in ^{o}K/day), for CTL, AVH, tSkin and Assim experiments. Top, middle and bottom rows are for NHE, tropics and SHE respectively.

Mean Q ANA x 1.e3 Tendency (NH: 20N- 90N)   STD DEV NH Q INC x 1.e3

TRO (20S- 20N)   TRO

SH (90S- 20S)   SH
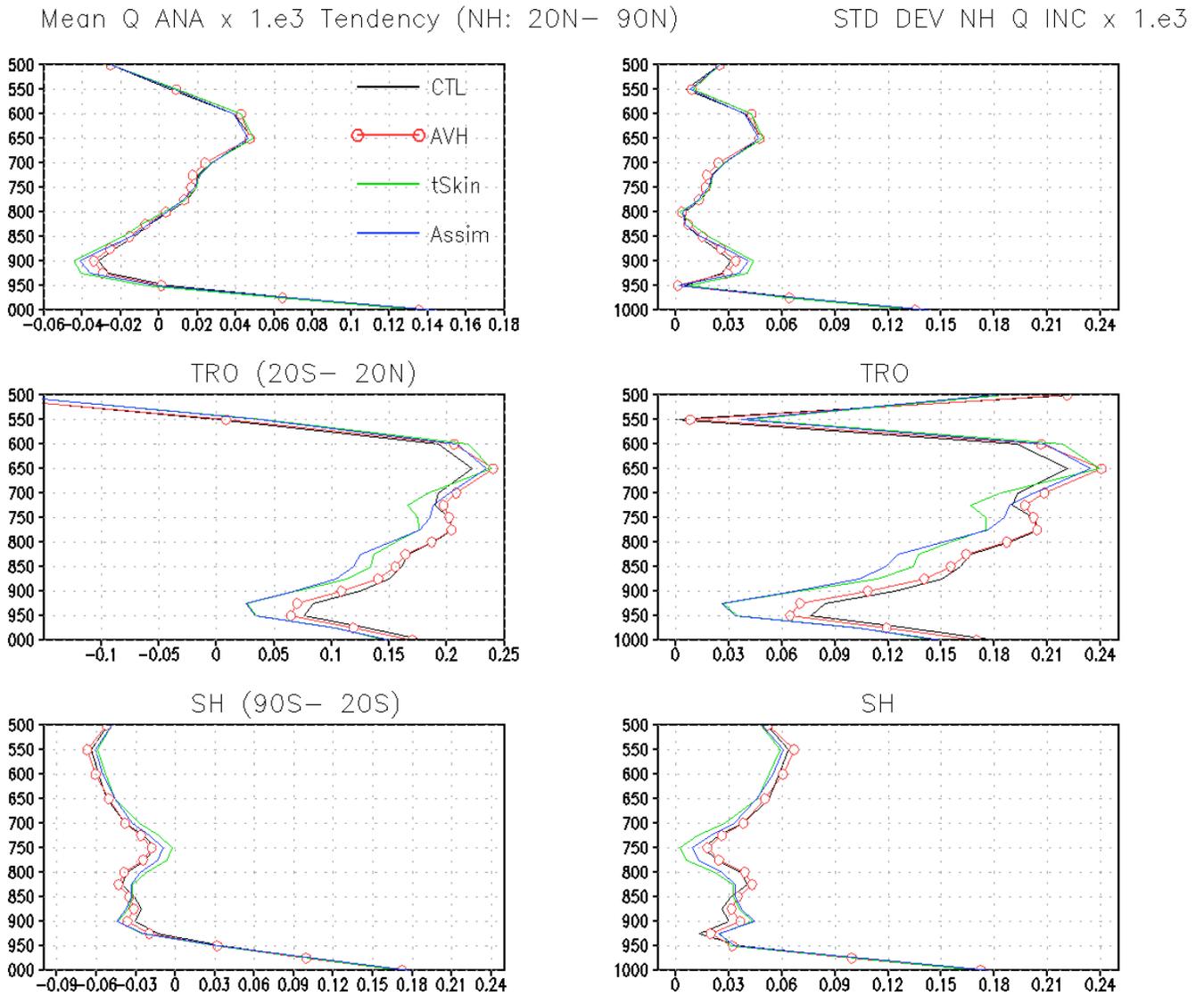
Figure 44: Same as in Fig. 43 but for specific humidity (g/Kg/day)

62
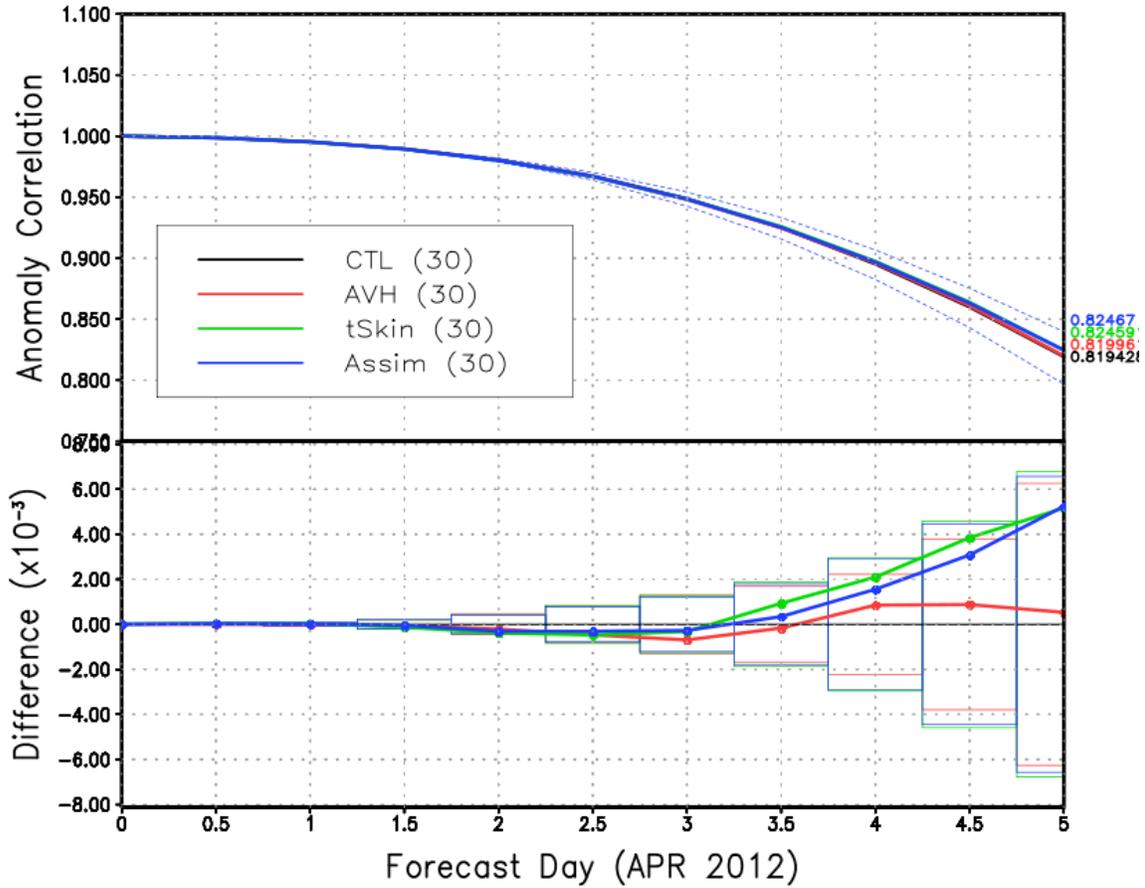
Figure 45: Top panel: anomaly correlation (ACOR) for 500-hPa geopotential height (global) for five day forecasts, and for the experiment period. The number in the parenthesis denotes the number of forecast samples used to calculate the ACOR. Bottom panel: difference in ACOR between the experiments (AVH, tSkin and Assim) and CTL; bars denote 95% confidence intervals.
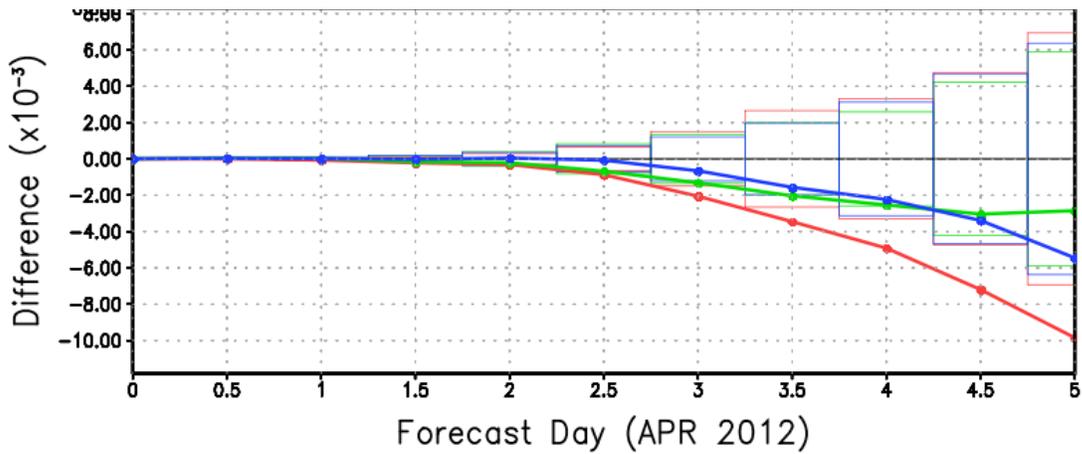
Figure 46: Difference in ACOR for the NHE 500-hPa geopotential height field. Legends are same as in the top panel of Fig. 45.
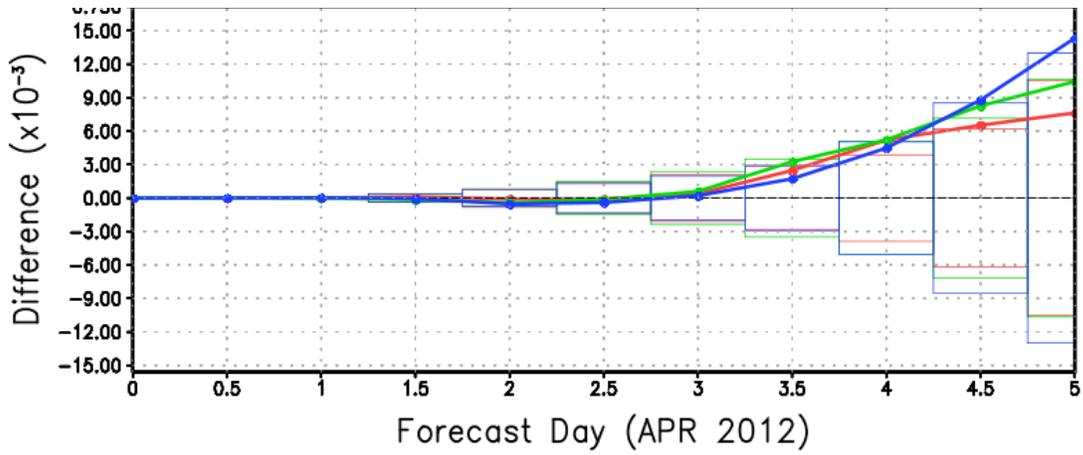
Figure 47: Same as in Fig. 46 but for the SHE.
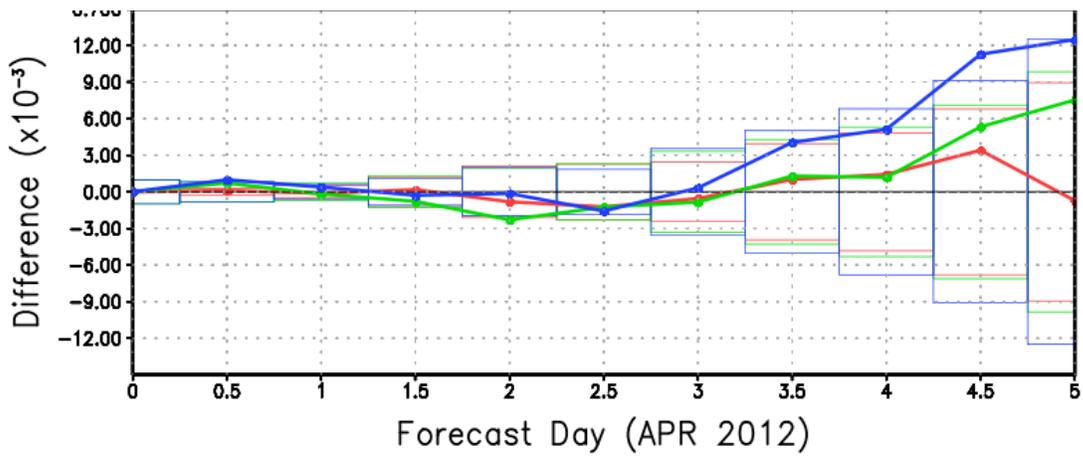
Figure 48: Same as in Fig. 46 but for the SHE temperature at 1000-hPa
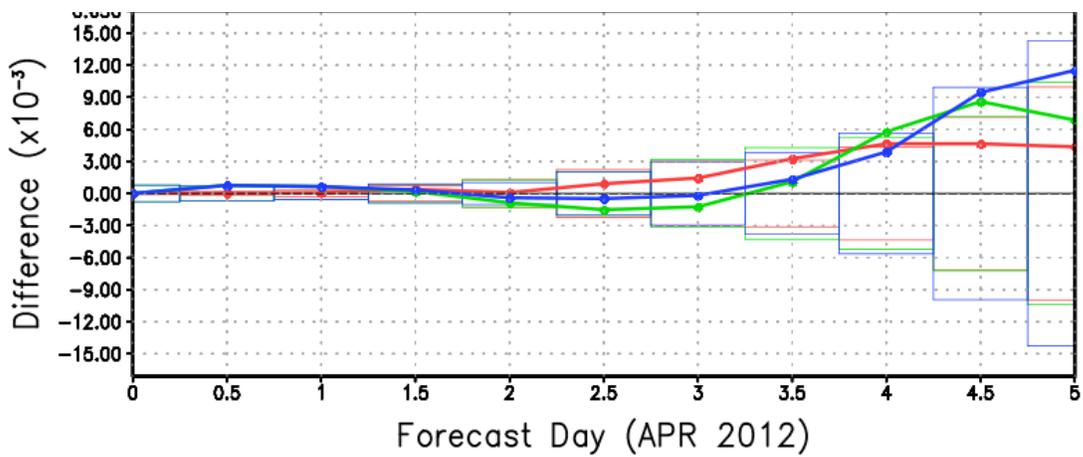
Figure 49: Same as in Fig. 46 but for the SHE temperature at 700-hPa

64

References

Beljaars ACM. 1997. Air-sea interaction in the ECMWF model. Seminar on Atmosphere-Surface Interactions. ECMWF, Reading, U. K.

Bellenger H, Duvel JP. 2009. An analysis of tropical ocean diurnal warm layers. *J. Climate* **22**: 3629– 3646, doi:10.1175/2008JCLI2598.1.

Bloom SC, Takacs LL, da Silva AM, Ledvina D. 1996. Data assimilation using incremental analysis updates. *Mon Weather Rev* **124**: 1256–1271.

Bosilovich MG, coauthors. 2015. MERRA-2: Initial evaluation of the climate. Technical Report Series on Global Modeling and Data Assimilation NASA/TM-2015-104606/Vol 43, NASA Goddard Space Flight Center.

Brassington GB, Martin MJ, Tolman HL, Akella S, Balmeseda M, Chambers CRS, Chassignet E, Cummings JA, Drillet Y, Jansen PAEM, Laloyaux P, Lea D, Mehra A, Mirouze I, Ritchie H, Samson G, Sandery PA, Smith GC, Suarez M, Todling R. 2015. Progress and challenges in short- to medium-range coupled prediction. *J Operational Oceanography.* **8**: s239– s258, doi: 10.1080/1755876X.2015.1049875.

Brunke MA, Zeng X, Misra V, Beljaars A. 2008. Integration of a prognostic sea surface skin temperature scheme into weather and climate models. *J Geophys Res-Atmos* **113**: D21 117, doi: 10.1029/2008JD010607.

Castro SL, Wick GA, Emery WJ. 2012. Evaluation of the relative performance of sea surface temperature measurements from different types of drifting and moored buoys using satellite-derived reference products. *J Geophys Res-Oceans* **117**: C02 029, doi:10.1029/2011JC007472.

Castro SL, Wick GA, Jackson DL, Emery WJ. 2008. Error characterization of infrared and microwave satellite sea surface temperature products for merging and analysis. *J Geophys Res* **113**: C03 010, doi:10.1029/2006JC003829.

Chen Y, Han Y, Weng F. 2012. Comparison of two transmittance algorithms in the community radiative transfer model: Application to AVHRR. *J Geophys Res-Atmos* **117**: D06 206, doi:10. 1029/2011JD016656.

Chen Y, Weng F, Han Y, Liu Q. 2008. Validation of the Community Radiative Transfer Model by using CloudSat data. *J Geophys Res* **113**: D00A03, doi:10.1029/2007JD009561.

Chou MD, Suarez MJ. 1994. An efficient thermal infrared radiation parameterization for use in general circulation models. NASA tech. memorandum 104606-vol 3, NASA Goddard Space Flight Center.

Curry JA, coauthors. 2004. Seaflux. *Bull. Amer. Meteor. Soc.* **85**: 409–424, doi:http://dx.doi.org/10. 1175/BAMS-85-3-409.

Dee D. 2004. Variational bias correction of radiance data in the ECMWF system. In: *Proceedings of the ECMWF Workshop on Assimilation of High Spectral Sounders in NWP*. ECMWF: Reading, UK, pp. 97– 112.

Dee DP, Balmaseda M, Balsamo G, Engelen R, Simmons AJ, Thépaut JN. 2014. Toward a consistent reanalysis of the climate system. *Bull. Amer. Meteor. Soc.* **95**: 1235–1248, doi:http://dx.doi.org/10.1175/BAMS-D-13-00043.1.

Dee DP, Uppala SM, Simmons AJ, Berrisford P, Poli P, Kobayashi S, Andrae U, M A Balmaseda GB, Bauer P, Bechtold P, Beljaars ACM, van de Berg L, Bidlot J, Bormann N, Delsol C, Dragani R, Fuentes M, Geer AJ, Haimberger L, Healy SB, Hersbach H, Holm EV, Isaksen L, Kallberg P, Kohler M, Matricardi M, McNally AP, Monge-Sanz BM, Morcrette JJ, Park BK, Peubey C, de Rosnay P, Tavolato C, Thepaut JN, Vitart F. 2011. The ERA-Interim reanalysis: configuration and performance of the data assimilation system. *Q. J. R. Meteorol. Soc.* **137**: 553– 597, doi:10.1002/qj.828.

Derber JC, Wu WS. 1998. The use of TOVS Cloud-Cleared Radiances in the NCEP SSI analysis system. *Mon Weather Rev* **126**: 2287– 2299, doi:http://dx.doi.org/10.1175/1520-0493(1998)126⟨2287:TUOTCC⟩2.0.CO;2.

Donlon C, coauthors. 2007. The global ocean data assimilation experiment high-resolution sea surface temperature pilot project. *Bull. Amer. Meteor. Soc* **88**: 1197–1213, doi:http://dx.doi.org/10.1175/BAMS-88-8-1197.

Donlon C, Minnett PJ, Gentemann C, Nightingale TJ, Barton IJ, Ward B, Murray MJ. 2002. Toward improved validation of satellite sea surface skin temperature measurements for climate research. *J. Climate* **15**: 353–369.

Donlon CJ, Martin M, Stark J, Roberts-Jones J, Fiedler E, Wimmer W. 2012. The Operational Sea Surface Temperature and Sea Ice Analysis (OSTIA) system. *Remote Sens. Environ.* **116**: 140–158, doi:10.1016/j.rse.2010.10.017.

Fairall CW, Bradley EF, Godfrey JS, Wick GA, Edson JB, Young GS. 1996. Cool-skin and warm-layer effects on sea surface temperature. *J Geophys Res-Oceans* **101**: 1295–1308, doi:10.1029/95JC03190.

Filipiak MJ, Merchant CJ, Kettle H, Borgne PL. 2010. A statistical model for sea surface diurnal warming driven by numerical weather prediction fluxes and winds. *Ocean Sci. Discuss.* **7**: 1497–1532, doi:10.5194/osd-7-1497-2010.

Gemmill W, Katz B, Li X, Burroughs LD. 2006. The daily Real-Time Global Sea Surface Temperature - high resolution analysis: RTG_SST_HR. Technical Procedures Bulletin MMAB/2006-01, Marine Modeling and Analysis Branch, Environmental Modeling Center, Camp Springs, MD 20746.

Gentemann CL, Donlon CJ, Stuart-Menteth A, Wentz FJ. 2003. Diurnal signals in satellite sea surface temperature measurements. *Geophys. Res. Lett.* **30**: 1140, doi:10.1029/2002GL016291.

Gentemann CL, Minnett PJ. 2008. Radiometric measurements of ocean surface thermal variability. *J. Geophys. Res.* **113**: C08 017, doi:10.1029/2007JC004540.

Gentemann CL, Minnett PJ, Ward B. 2009. Profiles of ocean surface heating (POSH): A new model of upper ocean diurnal warming. *J. Geophys. Res.* **114**: C07 017, doi:10.1029/2008JC004825.

Ham YG, Rienecker MM, Suarez MJ, Vikhliaev Y, Zhao B, Marshak J, Vernieres G, Schubert SD. 2014. Decadal prediction skill in the GEOS-5 forecast system. *Clim Dyn* **42**: 1–20, doi:10.1007/s00382-013-1858-x.

Han Y, van Delst P, Liu Q, Weng F, Yan B, Treadon R, Derber J. 2006. JCSDA Community Radiative Transfer Model (CRTM)- version 1. NOAA Technical Report NESDIS 122, U.S. Dept of Commerce, NOAA, Washington, D.C.

Hosoda K. 2010. A review of satellite-based microwave observations of Sea Surface Temperatures. *J Oceanogr* **66**: 439–473.

Kawai Y, Wada A. 2007. Diurnal Sea Surface Temperature variation and its impact on the Atmosphere and Ocean: A Review. *J Oceanogr* **63**: 721–744.

Kennedy JJ, Brohan P, Tett SFB. 2007. A global climatology of the diurnal variations in sea-surface temperature and implications for MSU temperature trends. *Geophys. Res. Lett.* **34**: L05 712, doi: 10.1029/2006GL028920.

Kleist DT, Parrish DF, Derber JC, Treadon R, Errico RM, Yang R. 2009a. Improving incremental balance in the GSI 3DVAR analysis system. *Mon Weather Rev* **137**: 1046–1060, doi:10.1175/ 2008MWR2623.1.

Kleist DT, Parrish DF, Derber JC, Treadon R, Wu WS, Lord S. 2009b. Introduction of the GSI into the NCEP Global Data Assimilation System. *Wea. Forecasting* **24**: 1691–1705, doi:http: //dx.doi.org/10.1175/2009WAF2222201.1.

Liang XM, Ignatov A, Kihali Y. 2009. Implementation of the Community Radiative Transfer Model in Advanced Clear-Sky Processor for oceans and validation against nightime AVHRR radiances. *J. Geophys. Res.* **114**: D06 112, doi:10.1029/2008JD010960.

Lumpkin R, Grodsky SA, Centurioni L, Rio MH, Carton JA, Lee D. 2013. Removing spurious low-frequency variability in drifter velocities. *J. Atmos. Oceanic Technol.* **30**: 353– 360, doi: 10.1175/JTECH-D-12-00139.1.

May DA, Parmeter MM, Olszewski DS, McKenzie BD. 1998. Operational processing of Satellite Sea Surface Temperature retrievals at the Naval Oceanographic Office. *Bull. Amer. Meteor. Soc.* **79**: 397– 407, doi:http://dx.doi.org/10.1175/1520-0477(1998)079⟨0397:OPOSSS⟩2.0.CO;2.

May DA, Stowe LL, Hawkins JD, McClain EP. 1992. A correlation of Saharan dust effects on satellite sea surface temperature measurements. *J Geophys Res* **97**: 3611– 3619.

McLay JG, Flatau MK, Reynolds CA, Cummings J, Hogan T, Flatau PJ. 2012. Inclusion of sea-surface temperature variation in the U.S. Navy ensemble-transform global ensemble prediction system. *J. Geophys. Res.* **117**: D19 120, doi:10.1029/2011JD016937.

Merchant CJ, Embury O, Le Borgne P, Bellec B. 2006. Saharan dust in nighttime thermal imagery: Detection and reduction of related biases in retrieved sea surface temperature. *Remote Sens. Environ.* **104**: 15– 30, doi:10.1016/j.rse.2006.03.007.

Molod A, Takacs L, Suarez M, Bacmeister J, Song IS, Eichmann A. 2012. The GEOS-5 Atmospheric General Circulation Model: Mean Climate and Development from MERRA to Fortuna. Technical Report Series on Global Modeling and Data Assimilation NASA/TM-2012-104606/Vol 28, NASA Goddard Space Flight Center.

Morel A, Huot Y, Gentili B, Werdell PJ, Hooker SB, Franz BA. 2007. Examining the consistency of products derived from various ocean color sensors in open ocean (Case 1) waters in the perspective of a multi-sensor approach. *Remote Sens. Environ.* **111**: 69– 88, doi: 10.1016/j.rse.2007.03.012.

Ohlmann JC, Siegel DA. 2000. Ocean radiant heating. Part II: Paramterizing solar radiation transmission through the upper ocean. *J Phys Oceanogr* **30**: 1849–1865.

Price JF, Weller RA, Pinkel R. 1986. Diurnal Cycling: Observations and models of the upper ocean response to diurnal heating, cooling and wind mixing. *J. Geophys. Res.* **91**: 8411–8427.

Putman WM, Lin SJ. 2007. Finite-volume transport on various cubed-sphere grids. *J Comput Phys* **227**: 55– 78, doi:10.1016/j.jcp.2007.07.022.

Reynolds RW, Rayner NA, Smith TM, Stokes DC, Wang Q. 2002. An improved in situ and satellite SST analysis for climate. *J. Climate* **15**: 1609–1625.

Reynolds RW, Smith TM, Liu C, Chelton DB, Casey KS, Schlax MG. 2007. Daily high-resolution-blended analyses for Sea Surface Temperature. *J. Climate* **20**: 5473–5496, doi: 10.1175/2007JCLI1824.1.

Rienecker MM, coauthors. 2008. The GEOS-5 Data Assimilation System. Documentation of versions 5.0.1 and 5.1.0, and 5.2.0. Technical Report Series on Global Modeling and Data Assimilation NASA/TM-2008-104606/Vol 27, NASA Goddard Space Flight Center.

Rienecker MM, Suarez MJ, Gelaro R, Todling R, Bacmeister J, Liu E, Bosilovich MG, Schubert SD, Takacs L, Kim GK, Bloom S, Chen J, Collins D, Conaty A, da Silva A, Gu W, Joiner J, Koster RD, Lucchesi R, Molod A, Owens T, Pawson S, Pegion P, Redder C, Reichle R, Robertson FR, Ruddick AG, Sienkiewicz M, Woollen J. 2011. MERRA: NASAs Modern-Era Retrospective Analysis for Research and Applications. *J. Climate* **24**: 3624–3648, doi:10.1175/JCLI-D-11-00015.1.

Roberts-Jones J, Fiedler EK, Martin MJ. 2012. Daily, global, high-resolution SST and Sea Ice Reanalysis for 1985-2007 using the OSTIA System. *J. Climate* **25**: 6215–6232, doi:10.1175/ JCLI-D-11-00648.1.

Saunders PM. 1967. The Temperature at the Ocean-Air Interface. *J Atmos Sci* **24**: 269–273.

Soloviev A, Lukas R. 1997. Observation of large diurnal warming events in the near-surface layer of the western equatorial Pacific warm pool. *Deep-Sea Res* **44**: 1055–1076.

Soloviev AV. 1982. On the vertical structure of the ocean thin surface layer at light wind. *Dokl. Acad. Sci. USSR Earth Sci. Sect. Engl. Transl.* **18**: 751–760.

Takaya Y, Bidlot JR, Beljaars ACM, Janssen PAEM. 2010a. Refinements to a prognostic scheme of skin sea surface temperature. *J Geophys Res-Oceans* **115**: C06 009, doi:10.1029/2009JC005985.

Takaya Y, Vitart F, Balsamo G, Balmaseda M, Leutbecher M, Molteni F. 2010b. Implementation of an ocean mixed layer model in IFS. Technical Memorandum 622, European Centre for Medium-Range Weather Forecasts, Shinfield Park, Reading, RG2 9AX, England, URL http://www.ecmwf.int/publications/.

Todling R. 1999. Estimation theory and foundations of atmospheric data assimilation. Office Note Series on Global Modeling and Data Assimilation 1999-01, NASA Goddard Space Flight Center.

Todling R. 2013. Comparing two approaches for assessing observation impact. *Mon Weather Rev* **141**: 1484–1505, doi:http://dx.doi.org/10.1175/MWR-D-12-00100.1.

Vernieres G, Rienecker MM, Kovach R, Keppenne CL. 2012. The GEOS-iODAS: Description and Evaluation. Technical Report Series on Global Modeling and Data Assimilation NASA/TM-2012-104606/Vol 30, NASA Goddard Space Flight Center.

Ward B. 2006. Near-surface ocean temperature. *J. Geophys. Res.* **111**: C02 004, doi:10.1029/2004JC002689.

While J, Martin M. 2013. Development of a variational data assimilation system for the diurnal cycle of sea surface temperature. *J Geophys Res-Oceans* **118**: 2845–2862, doi:doi:10.1002/jgrc.20215.

Wick GA, Ohlmann JC, Fairall CW, Jessup AT. 2005. Improved oceanic cool-skin corrections using a refined solar penetration model. *J Phys Oceanogr* **35**: 1986–1996.

Wieliczka DM, Weng S, Querry MR. 1989. Wedge shaped cell for highly absorbent liquids: infrared optical constants of water. *Appl Optics* **28**: 1714– 1719.

Xu F, Ignatov A. 2014. In situ SST Quality Monitor (iQuam). *J. Atmos. Oceanic Technol.* **31**: 164–180, doi:http://dx.doi.org/10.1175/JTECH-D-13-00121.1.

Zeng X, Beljaars A. 2005. A prognostic scheme of sea surface skin temperature for modeling and data assimilation. *Geophys Res Lett* **32**(14): L14 605, doi:10.1029/2005GL023030.

Appendix A. Acronyms

ADAS   atmospheric data assimilation system

AGCM   atmospheric general circulation model

AIRS   Atmospheric Infrared Sounder

AMSU   Advanced Microwave Sounding Unit

ACOR   anomaly correlation

AVHRR   Advanced Very High Resolution Radiometer

CRTM   Community Radiative Transfer Model

DAS   data assimilation system

ECMWF   European Center for Medium-Range Weather Forecasts

GEOS   Goddard Earth Observing System

GOCART   Goddard Chemistry, Aerosol, Radiation, and Transport

GMAO   Global Modeling and Assimilation Office

GSI   Gridpoint Statistical Interpolation

IASI   Infrared Atmospheric Sounding Interferometer

IAU   Incremental Analysis Update

IESA   integrated earth system analysis

IR   infrared

MW   microwave

NHE   northern hemisphere extratropics

OLR   outgoing longwave radiation

OMA   observation minus analysis

OMB   observation minus background

OSTIA   Operational Sea Surface Temperature and Sea Ice Analysis

SHE   southern hemisphere extratropics

SLP   sea level pressure

SST   sea surface temperature

Appendix B. Quality control of AVHRR observations

The following sequence of steps are performed for rejecting and deweighting the data:

1. reject if solar zenith angle $\leq 89^o$,

2. reject if observed $\mathbf{T_b} \leq 0^o K$ or $\geq 500^o K$,

3. reject over high topography (does not apply over ocean),

4. modify observational weights (Derber and Wu, 1998) according to CRTM computed atmospheric transmittance (Chen *et al.*, 2012).

5. cloud qc: all channels are rejected if cloud is detected, at any observation location,

6. weight according to sensitivity of $\mathbf{T_b}$ to $\mathbf{T_s}$ and emissivity,

7. a physical retrieval check: Appendix 1 of Gemmill *et al.* (2006),

8. gross check: if the difference between bias-corrected background and observed $\mathbf{T_b}$ is $> 3\,\sigma_o$.

We illustrate the application of the above steps for a single analysis performed on Apr 30, 2012 at 12 UTC. Fig.B50 depicts the observed $\mathbf{T_b}$ using AVHRR and IASI sensors on the Metop-A satellite. For the channels 4 and 5 of AVHRR we plotted IASI data from similar wavelenth channels; there is no assimilated channel on IASI that is spectrally close to AVHRR Ch 3. The pixel size of the GAC AVHRR data is about $4km^2$, whereas IASI footprint is about $50km^2$, and thinning box was set to $145km^2$ for both sensors. We notice that the $\mathbf{T_b}$ is greater than $300^o K$ for Ch 3 in the daytime (due to the solar contamination mentioned in section 4.2). As for Ch 4 and 5, the observed $\mathbf{T_b}$ is almost the same for AVHRR and IASI; the slight variation is due to the narrow spectral width of the IASI channels compared to the broader width of AVHRR. We also note that there are no observations from the AVHRR over land and sea ice (because we selected ocean-only GAC data) and that there are gaps over open ocean (due to the application of cloud mask in the GAC data (section 4.2); there is no cloud mask for the IASI level 1B radiance data used in the GEOS-ADAS).

Fig. B51 shows the OMB computed using the CRTM simulated $\mathbf{T_b}$ (before quality control and bias correction); we notice that the OMB is similar for AVHRR and IASI channels. After quality control, as shown in Fig. B52, we get rid of most of the cold biased observation locations and also the daytime observations of Ch 3, with similar results for channels 4 and 5 of AVHRR and IASI.

This shows that our procedure for the quality control and overall treatment of the AVHRR is similar to that currently being used for any IR sounder, illustrated with the aid of IASI on Metop-A. To complete this discussion, the OMB after bias correction is shown in Fig. B53. Bias correction seems to correct for regions of cold (warm) OMB bias by introducing a warm (cold) correction, hence trying to yield global mean OMB closer to zero. Notice that the Ch 3 AVHRR cold stripes at the edges of the scan (similar to figure 6 of Chen *et al.* (2012)) seen before bias correction (Fig. B52(a)) significantly benefit from bias correction (Fig. B53(a)), and the bias-corrected OMB is homogeneously distributed.
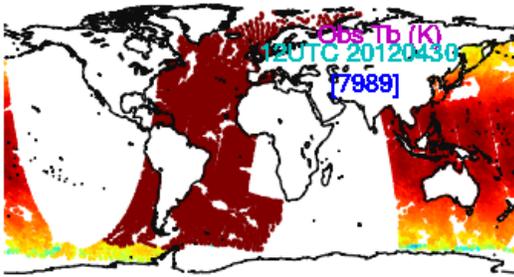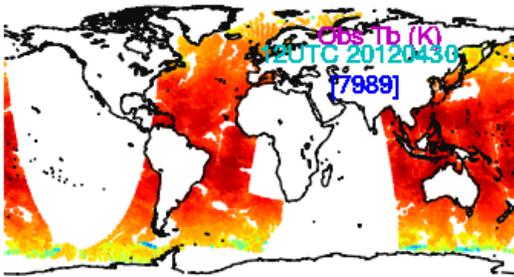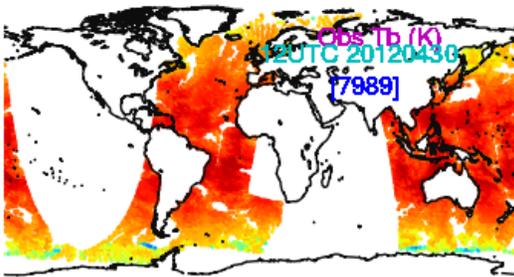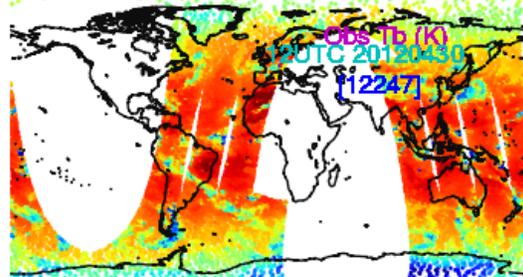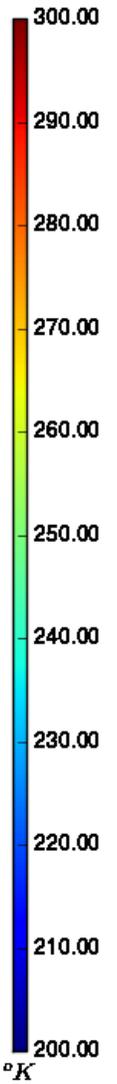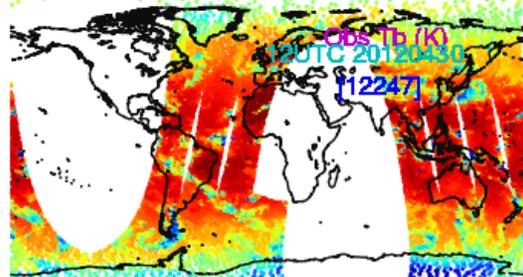
Figure B50: Observed brightness temperature (in ^oK) on 30 Apr 2012 within the 6-hour assimilation window centered at 12 UTC. (left) AVHRR on Metop-A: (a) Ch 3, (b) Ch 4, (c) Ch5. (right) IASI, also on Metop-A: (I) Ch 204, (II) Ch 195.
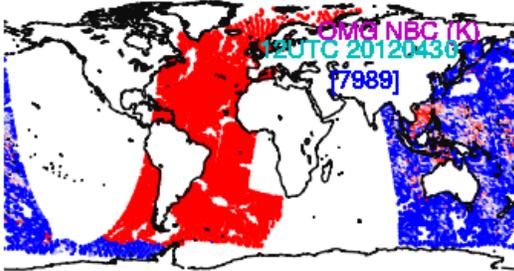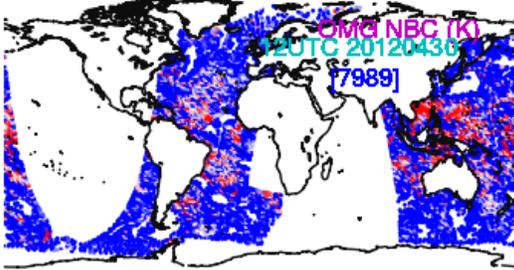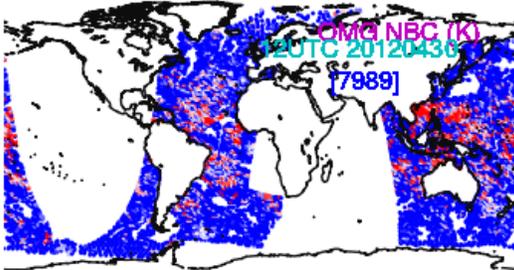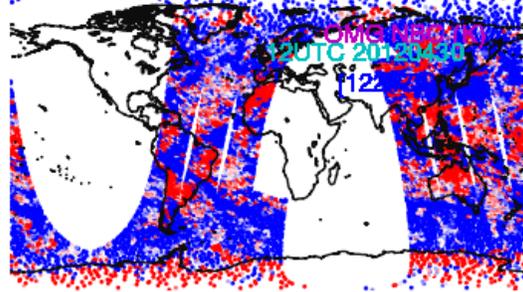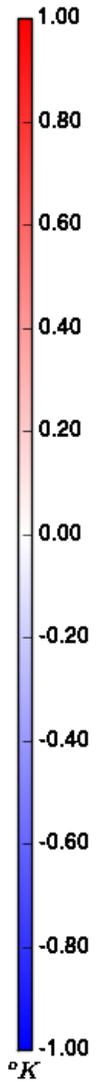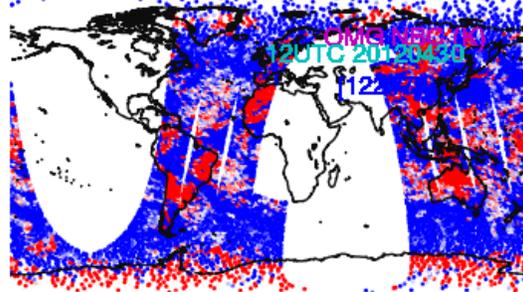
Figure B51: Same as in Fig. B50 but for the OMB before bias correction and no quality control.
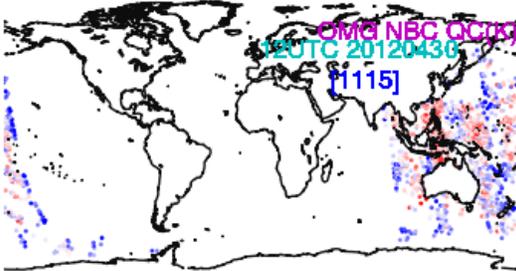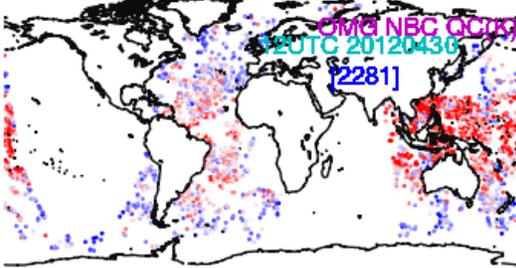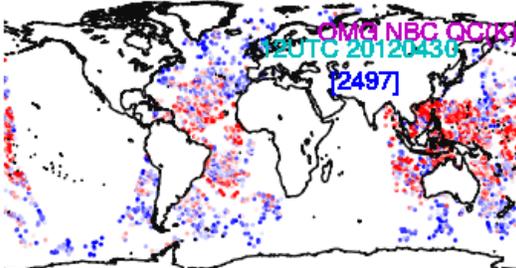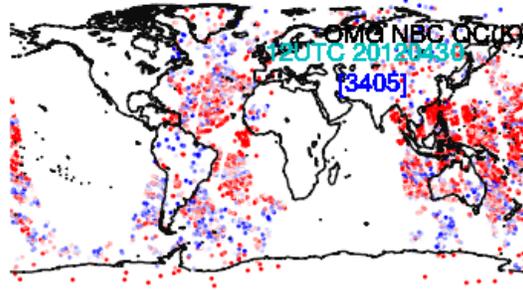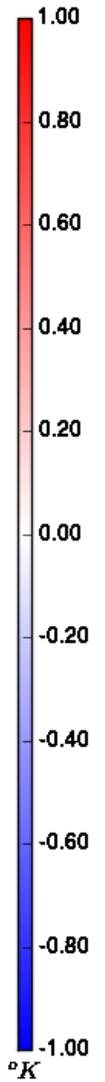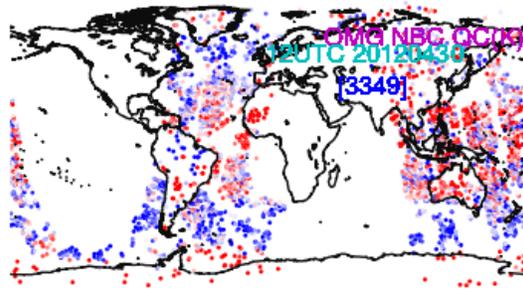
Figure B52: Same as in Fig. B51 but **after** quality control.
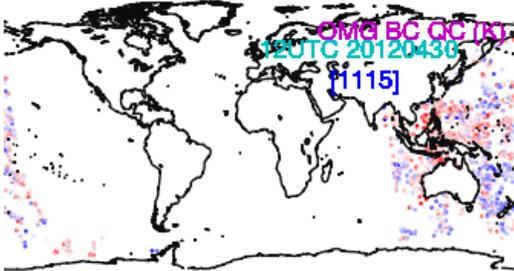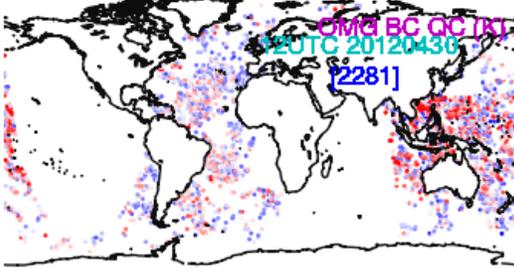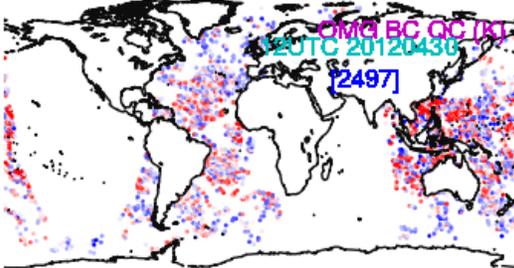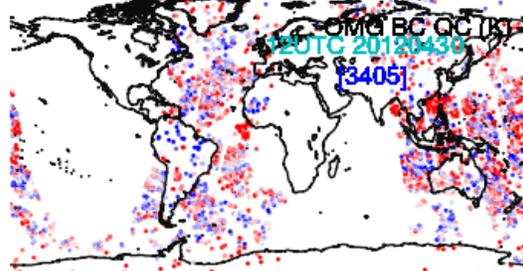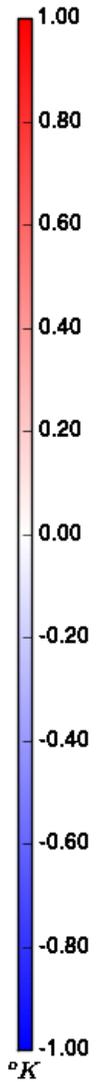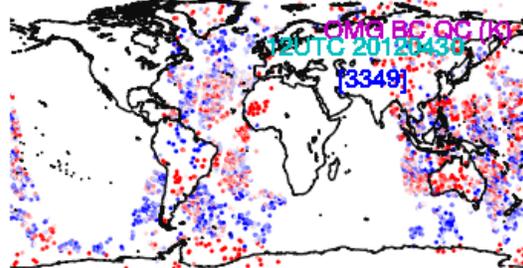
Figure B53: Same as in Fig. B52 but **after** bias correction

Appendix C. A simple interpretation of analysis increment

Let's define the following *errors* with respect to a reference or *true* state x_t :

$$
\begin{aligned}
\varepsilon_o &= y^o - H[x_t] \\
\varepsilon_b &= x_b - x_t \\
\varepsilon_a &= x_a - x_t
\end{aligned}
$$

where $\varepsilon_o, \varepsilon_b, \varepsilon_a$ denote the error in observation (y^o), background (x_b) and analysis (x_a), respectively; $H[\cdot]$ denotes a linearized observation operator that maps the state to observations space. Here all the variables are *vectors*; background, analysis and reference states are of the same dimension as the model state-space, but observational dimension is typically much smaller than model dimension.

Following a Kalman filtering approach,

$$
\begin{aligned}
x_a &= x_b + \mathbf{K}(y^o - H[x_b]) \\
&= x_b + \mathbf{K}(\varepsilon_o - H[\varepsilon_b]),
\end{aligned}
$$

where $\mathbf{K}$ is the Kalman gain matrix. Then the analysis increment is $\Delta x = x_a - x_b = \mathbf{K}(y^o - H[x_b])$. Recall that the observation minus background is $\mathtt{OMB} = y^o - H[x_b]$; therefore $\Delta x = \mathbf{K}\,\mathtt{OMB}$. Taking expectations (denoted by $< \cdot >$) on both sides, we obtain

$$
< \Delta x > = < \mathbf{K} >< \mathtt{OMB} >
$$

For a well *tuned* analysis system (with *optimal* observational and background errors) typically the trace of $\mathbf{K} \to C_o$, an asymptotic value. Therefore $< \Delta x > \propto < \mathtt{OMB} >$, i.e., mean of OMB and analysis increment are directly related to each other. Generally speaking, unbiased increments would be a sign of unbiased OMB (see chapter 5 of Todling (1999)). Similarly, $< \Delta x \Delta x^T > \propto < \mathtt{OMB} >< \mathtt{OMB}^T >$, which implies that a *smaller* increment (in a norm), is a sign of smaller OMB residue.

Previous Volumes in This Series